ABSTRACT

Title of Thesis: CHARACTERIZING THE QUASI-STATIC AND DYNAMIC RESPONSE OF A NON-CONTACT MAGNETO-ELASTIC TORQUE SENSOR

Brooks Muller, Master of Science, 2017

Thesis directed by: Professor Alison Flatau,
Department of Aerospace Engineering

Advances in the development of rolled-sheet magnetostrictive materials led to testing of a prototype wireless magneto-elastic torque (WiMET) sensor using the iron alloy Galfenol. As torque was applied to a shaft, stress-induced changes in the magnetic state of Galfenol that was bonded to the shaft were proportional to the applied torque. Building on that work, this thesis investigates strategies to improve both repeatability and the signal to noise ratio of WiMET sensor output. Multi-physics models of WiMET stress and magnetic states under applied torques are used to improve understanding of sensor operation. Testing to validate simulations is performed using Galfenol and Alfenol, a newer rolled-sheet alloy, for torsional loads of 0 – 200 in-lb, and under quasi-static and dynamic (0 – 2000 RPM) loading conditions. The experimental results presented support the potential of WiMET sensor use for dynamic torque measurement and health monitoring of drive train systems.

CHARACTERIZING THE QUASI-STATIC AND DYNAMIC RESPONSE OF A NON-CONTACT MAGNETO-ELASTIC TORQUE SENSOR

by

Brooks Muller

Thesis submitted to the Faculty of the Graduate School of the
University of Maryland, College Park in partial fulfillment
of the requirements for the degree of
Master of Science
2017

Advisory Committee
Dr. Alison Flatau, Chair
Dr. David Akin
Dr. Inderjit Chopra

Dedication

To the memory of my late
Grandparents Joan Boehm and John Muller
and
Uncle Thomas Muller

And

To my friends, family, and loved ones
For their constant encouragement and support

Acknowledgements

First and foremost, I would like to thank my advisor Dr. Alison Flatau for her guidance and support over the course of my research assistantship. Her constant encouragement and thoughtful advice have helped me become a more skillful and independent researcher, for which I am incredibly grateful.

This research was sponsored by Army AATD, Award Number W911W61120012, through the Vertical Lift Research Center of Excellence.

I would like to extend a special thank you to all of our collaborators across agencies and organizations for providing the technical assistance, feedback, and unique points of view which guaranteed the success of this project.

Our collaborators at Army Research Lab at Aberdeen Proving Grounds helped define clear goals for the project and provided constructive feedback during quarterly in-person status updates. I would especially like to thank Anindya Ghoshal, Muthuvel Murugan, Brian Dykas, and all other members of ARL team. I would also like to thank our collaborators at NASA Glenn, Vivake Asnani and Justin Scheidler for their input at ARL review sessions. Thank you all for taking the time to meet over the last few years and for taking an interest in this project.

I would like to extend my thanks to our collaborators at Innovital Systems. Dr. Ashish Purekar provided enlightening advice on sensor design and testing protocol early in the project, while tests conducted with Pablo Sztein informed testing procedure for operation in the dynamic mode.

I would also like to thank Treven Baker, Drives Technical Area Lead with the Aviation Development Directorate, for his comments and suggestions for future research in adapting the WiMET sensor for operation in more realistic environments.

I would like to acknowledge and extend my sincere thanks to the researchers, graduate students, and undergraduate students of the Aerosmart team who have worked with me over the last three years. Dr. Suok Min Na ensured that only the highest quality Galfenol and Alfenol samples were provided for this project, and this research would not have been possible without his metallurgic skills and expertise with magneto-elastic materials. Dr. Jung Jin Park has always been a friendly face around the lab, and his expertise and methodology in developing magnetostrictive sensors has provided me with the perfect example to follow.

Among graduate students, Ganesh Raghunath ensured that I began my research on the right foot, and has made sure to keep up with my progress, offering technical assistance with the test setup that he passed on to me. Maxim Germer, an exchange student from the University of Dresden, offered an outsider's perspective on my project and was always willing to ask the difficult-to-answer questions which vastly improved the quality of my research methodology and experimental results. Finally, Michael Van Order has been a steadfast friend, a source of constant encouragement, and an all-around superb labmate over the last three years. Among Aerosmart undergraduate students, I would like to thank Samantha Walters for her initial assistance in operating the benchtop test setup, Joey Cozzo for his enlightening COMSOL models, and Julia Downing and Allie Orr for their willingness to learn and collaborate. Thank you all so much.

Last but not least I would like to thank my family, my friends, and my significant other for their constant love and support over the years, without which this accomplishment would not have been possible.

Table of Contents

Dedication……ii

Acknowledgements…… iii

Table of Contents……vi

List of Tables……...ix

List of Figures……xi

List of Equations……xviii

Chapter 1: Introduction……1
1.1 Motivation……..1
1.2 Torque Sensor State of the Art……...2
1.2.1 Torsion-Bar Twist-Angle Sensors……...2
1.2.2 Magneto-Elastic Torque Sensors……....…….3
1.3 Magnetostriction……..…..…. 5
1.3.1 Crystal Axes and Magnetic Anisotropy……..6
1.3.2 Magnetostrictive Effect……...7
1.3.3 Inverse Magnetostrictive Effect……...9
1.3.4 Magnetostrictive Materials……....11
1.4 Wireless Magneto-Elastic Torque (WiMET) Sensor……...14
1.5 Experimental Investigation Overview……..20

Chapter 2: Modeling and Simulation…….....22
2.1 Coordinate Systems…….....22
2.2 Torsion……23
2.2.1 Mohr's Circle Analysis of a Solid Shaft in Torsion……26
2.3 Magnetostriction Modeling Review……30
2.4 COMSOL Modeling……32
2.4.1 Assumed Material Properties and Model Geometry……32
2.4.2 Torque Application……...34
2.4.3 Meshing……35
2.4.4 Results……...36
2.5 Summary……..44

Chapter 3: Experimental Setup……..45
3.1 Material Samples……45
3.2 Benchtop Test Setup……49
3.2.1 WiMET Sensor……50
3.2.2 Torque Application……...51
3.3 Sensor Positioning……...52
3.3.1 Lateral Magnet Positioning……...53

3.3.2 Vertical Hall Effect Sensor Positioning……56
3.3.3 Final Sensor Configuration……...57
3.4 Preliminary Bi-Directional Quasi-Static (BDQS) Testing……..58
3.5 Bonding Method Investigation…….....60
3.5.1 Initial Adhesive Selection……60
3.5.2 Testing Procedure……62
3.5.3 Independent Variables……..64
3.5.4 Results……...65
3.5.5 Repeatability……67
3.5.6 Additional Observations……...69
3.6 Quasi-Static Test Setup……71
3.6.1 Characterizing Effect of Flexible Couplings……71
3.6.2 Difference Between Measured and Modeled Strain……76
3.7 Dynamic Test Setup……80
3.7.1 Operational Limits……82

Chapter 4: Experimental Results and Analysis……..85
4.1 Quasi-Static Benchtop Testing……85
4.1.1 Testing Procedure……85
4.1.2 Data Analysis……86
4.1.3 Results……...88
4.1.4 Repeatability……92
4.1.5 Sensitivity……94
4.2 Dynamic Benchtop Testing……96
4.2.1 Testing Procedure……96
4.2.2 Data Analysis……98
4.2.2.1 Effect of Moving Average Filter on Response……98
4.2.2.2 Effect of Sampling Rate on Response……...103
4.2.2.3 Data Collection……103
4.2.3 Results and Discussion……...……104
4.2.3.1 Shaft Measurements……104
4.2.3.2 Repeatability……105
4.2.3.3 Effect of Rotation Direction……110
4.2.3.4 Effects of RPM Variation……113
4.2.3.5 Dynamic Sensitivity……119
4.3 Comparison of Experimental Results and Simulation……...120

Chapter 5: Conclusions and Future Work……126
5.1 Summary of Results……...126
5.2 Recommendations……..129
5.3 Future Work……...130
5.3.1 Testing in Realistic Operating Conditions……..131
5.3.2 Proposed testing with Army Research Lab……133

Appendices……...137
Appendix A: EBSD Images of Magnetostrictive Samples……..137

Appendix B: Modeling Magnetostriction……139
Appendix C: Preliminary BDQS Testing Results……143
Appendix D: Quasi-Static Drift Over One Minute……..150

Works Cited……151

List of Tables

Table 1.1: Material properties of magnetostrictive materials

Table 2.1: COMSOL model assumed material properties

Table 2.2: COMSOL model element geometry

Table 2.3: COMSOL parameters for predefined "Extra-fine" mesh

Table 3.1: Preliminary test cases

Table 3.2: Magnetostrictive sensing elements used in BDQS and Dynamic testing

Table 3.3: Quasi-static system specifications

Table 3.4: Hall effect sensor voltage measured at five locations under a 50 in-lb applied torque

Table 3.5: Hall effect sensor signal output at varied distances between patch and sensor

Table 3.6: Sensitivity of magnetostrictive sensing elements based on preliminary testing

Table 3.7: Adhesive bonding method test variables

Table 3.8: Adhesive volume used for different samples

Table 3.9: Demonstrating repeatability of best quality bond

Table 3.10: Quasi-static test cases

Table 3.11: Torque and theoretical twist in aluminum shaft, nine inches from fixed end

Table 3.12: Relative position and expected strain at each sample edge during quasi-static and dynamic testing

Table 3.13: Dynamic test cases

Table 3.14: Dynamic system specifications

Table 3.15: Speeds and applied torques tested in the dynamic mode

Table 4.1: Quasi-static testing schedule

Table 4.2: Sensitivity of magnetostrictive sensing elements in the quasi-static mode

Table 4.3: Randomization scheme and execution order of tests characterizing the response of an FeAl ring and FeGa Paint at 1000 RPM

Table 4.4: Dynamic Response at 1000 RPM

Table 4.5: Dynamic Sensitivity of FeGa and FeAl Samples

Table 4.6: WiMET sensor sensitivity estimation

Table 4.7: Sensitivity summary

Table 4.8: Differences in sensor configuration between prototype WiMET and current WiMET configurations

Table 5.1: Comparing modeling, quasi-static, and dynamic results

Table C.1: Randomized number strings used for testing

Table C.2: Sensitivity of magnetostrictive sensing elements before updated bonding protocol.

List of Figures

Figure 1.1: A unit cell with Miller index notation depicts the [100], [010], [001], and [111] directions and the (001) plane.

Figure 1.2: The application of a magnetic field induces magnetostriction.

Figure 1.3: Strain occurs in the direction of magnetization and maximum or saturation strain magnitude is independent of field polarity.

Figure 1.4: Experimental λ-H curves of 19 at.% Ga, furnace cooled, <100> oriented, single-crystal $Fe_{81}Ga_{19}$ under compressive prestress of 0, 15, 30, 45, 60, and 80 MPa, obtained by Atulasimha.

Figure 1.5: Experimental B-σ curves of furnace cooled, <100> oriented, single-crystal $Fe_{81}Ga_{19}$ under constant magnetic fields of 0, 22.3, 44.6, 66.9, 89.1, 111, 167, 223, 446, and 891 Oe, obtained by Atulasimha et al.

Figure 1.6: Magnetostriction (top) and magnetization (bottom) vary in a FeGa sample as applied magnetic field (Oe) is increased at -21˚C, 22˚C, and 80˚C.

Figure 1.7: The WiMET sensor is primarily composed of a magnetostrictive patch mounted on a shaft, with a Hall effect sensor and biasing magnet mounted to a high permeability flux piece above the patch (based on Raghunath et al.).

Figure 1.8: The magnet applies a magnetic bias to the magnetostrictive sensing element and stray fields from the patch are detected by the Hall effect sensor. Blue arrows are included to illustrate the flux path whereby flux from the permanent magnet flows through air to the magnetostrictive patch, through the patch, through air and the Hall effect sensor to the flux piece, and back to the permanent magnet.

Figure 1.9: As a torque is applied to the shaft (indicated by arrows at both ends of the shaft), shear stress in the patch along the principle axis, i.e. rotated 45˚ for the axis of the shaft (shown with thin red arrow labels τ), induces a change in magnetic flux density in the magnetostrictive patch and as a result throughout the magnetic flux path (indicated by red outline on the blue arrows depicting the flux circuit). The Hall effect sensor measures the change in magnetic flux in the air gap between the patch and the flux piece.

Figure 1.10: Commercial torque sensor (in-lb) and Hall effect sensor (mV) outputs plotted over time demonstrate a reduced level of response for applied loads >~50 in-lb in upper and lower graphs, respectively.

Figure 1.11: A decrease in response sensitivity is noted over a range of RPMs for loads in excess of ~20 in-lb.

Figure 2.1: Cartesian (x,y,z) and Cylindrical (r,φ,a) coordinate systems were defined to allow for accurate placement of modeling elements and proper application of torque.

Figure 2.2: An element on the surface of a shaft in perfect torsion experiences no forces or stresses other than $\tau_{\varphi a}$ and $\tau_{a\varphi}$.

Figure 2.3: A cross-sectional element *dA* in torsion experiences stress along the *rφ*-plane in the direction of applied torque.

Figure 2.4: An element on the surface of a shaft under axial (tension) and torsional (anti-clockwise, or negative) loading is exposed to axial stresses σ_x and σ_y and shear stress τ_1.

Figure 2.5: Points *A* and *B* are plotted along the *τ*-axis and *σ*-axis in the Mohr's Circle of an element on the surface of a shaft exposed to applied axial and shear stresses.

Figure 2.6: In pure clockwise torsion, the element experiences no axial stress.

Figure 2.7: A Mohr's Circle representation of a solid rod in pure clockwise torsion depicts principal stresses $\sigma_1 = \tau_{max}$ in tension and $\sigma_2 = -\tau_{max}$ in compression and angle $\theta = 45°$.

Figure 2.8: Torque was applied in the COMSOL model via the scheme shown in this figure along the length of the shaft.

Figure 2.9: An extra-fine mesh was applied to the entire model to ensure accurate rendering of the magnet, flux piece, hall effect sensor, and FeGa patch.

Figure 2.10: The maximum von Mises stress (N/m^2) occurred at the fixed end of the shaft and decreased along the *x*-axis under an applied torque of +200 in-lb.

Figure 2.11: The FeGa patch experienced less surface stress than the underlying aluminum, and twisted due to application of +200 in-lb.

Figure 2.12: Viewed along the length of the shaft, the FeGa patch experiences ~5MPa across its surface, the underlying aluminum shaft experiences ~6MPa, and a volume maximum stress within the FeGa patch of ~10MPa can be observed along its edge.

Figure 2.13: Principal stress occurs at roughly ±45˚ from the *x*-axis as predicted under (a) +200 in-lb and (b) -200 in-lb of applied torque.

Figure 2.14: Principle strain was expected to vary by ~50 μstrain between the edges of the test section, which are approximately ±5 in from the center of the FeGa patch along the *x*-axis.

Figure 2.15: Magnetic flux lines in this COMSOL visualization rendered only on the +*y*-direction side of the *x*-axis.

Figure 2.16: Magnetic flux density decreases by ~50% across a 0.01 in thick air gap between the FeGa patch and Hall effect sensor.

Figure 2.17: The FeGa patch is exposed to about 960 Oe directly beneath the magnet, and applied field strength decreases rapidly in all directions as distance from the magnet decreases.

Figure 2.18: Assuming no torque greater than 200 in-lb is applied to the shaft, the WiMET sensor should operate along one of the curves to the right of the hatched line depending on magnet strength, magnet position, and Hall effect sensor position in the physical test setup.

Figure 3.1: Test samples included (a) & (b) two FeGa samples, (c) three FeAl rings with thicknesses of 0.1, 0.15, and 0.4 mm, and (d) one FeAl patch and (e) an FeGa paint sample.

Figure 3.2: Magnetostrictive patches and rings were positioned along the 12 in long test section according to positions listed in Table 3.2 during quasi-static testing.

Figure 3.3: Magnetostrictive patches and rings were positioned along the 12 in long test section according to positions listed in Table 3.2 during dynamic testing.

Figure 3.4: The BDQS benchtop test setup is composed of a lever arm for load application, a 1 in diameter 2 ft long aluminum shaft, a commercial torque sensor, a brake, and Lovejoy flexible couplings between each component.

Figure 3.5: The WiMET sensor is presented in profile with its components identified.

Figure 3.6: Torque was applied to the shaft by placing a number of 5 lb weights 10 in from the longitudinal axis of the shaft, with the pictured ± directional convention.

Figure 3.7: The bias magnet was positioned at (a) the far end of flux piece, (b) left of the left edge of the patch, (c) centered above the left edge of the patch, (d) right of the left edge of the patch, and (e) in the center of flux piece above the patch.

Figure 3.8: In lateral position testing, the greatest signal was achieved with (a) the configuration above, presented in profile, with (b) a 10mV change in Hall effect sensor voltage output on application of a 50 in-lb torque.

Figure 3.9: Hall effect sensor was mounted above the magnetostrictive patch at a height of (a) 0.05 in (b) 0.025 in (c) 0.01 in (arrows indicate trends, as actual air gaps are just barely discernable in this image).

Figure 3.10: Maximum sensor response was achieved in (a) the above configuration, with (b) a Hall effect sensor output voltage of ~30mV on application of 50 in-lb.

Figure 3.11: Strain gages were mounted on and between similar samples of steel with different underlying adhesives to provide strain reading along the length of a sheet of aluminum as tip loads were applied.

Figure 3.12: Initial bending tests on a thin aluminum sheet demonstrated the superior performance of Loctite 648.

Figure 3.13: The test setup for the adhesive bonding method study was comprised of the above (a) steel shaft, (b) torque wrench, (c) steel shim, (d) wax paper, (e) syringe containing Loctite 648 adhesive, and (f) hose clamps.

Figure 3.14: Adhesive application configurations included a) a single 0.05 mL droplet, b) a single 0.03 mL droplet, c) a single 0.01 mL droplet, d) five 0.01 mL droplets, and e) nine 0.01 mL droplets.

Figure 3.15: This image shows the steel shim after debonding to examine bond layer thickness. A uniform bond layer formed around the edges of the shim when sanded with 60 grit sandpaper, using a 15 in-lb applied torque with 0.05 mL of Loctite 648 applied evenly to the bottom surface of the shim.

Figure 3.16: Repeatability test case 9 demonstrated a pooling of adhesive in a structural deformation present in the shim patch.

Figure 3.17: A non-uniform bond layer, with adhesive pooling around an air bubble, formed due to imperfect sanding of the shaft and shim sample.

Figure 3.18: An incomplete bond layer formed due to insufficient torque application (5 in-lb) while the adhesive cured.

Figure 3.19: A camera mounted above the test section provided images of the shaft during and after torque applications.

Figure 3.20: Etches were made adjacent to the magnetostrictive sensing element while adhered to the shaft in order to calculate angular displacement under applied bi-directional torsional loading.

Figure 3.21: An ImageJ screenshot shows a yellow line which provided the coordinates of the top edge of shaft, the bottom edge of shaft, and a midpoint between the two.

Figure 3.22: Angular displacement was determined by (a) measuring x_1 and x_2 for each etch and (b) calculating the difference of angles θ_1 and θ_2 with respect to the midpoint. x_1 was measured when no load was applied, and x_2 was measured when a was applied.

Figure 3.23: Strain gages were mounted 10 in apart, on either end of the test section, and atop the FeGa patch to determine if the position along the shaft of each magnetostrictive sample would impact sensor performance and to determine the decrease in principle strain between the surfaces of the aluminum shaft and FeGa patch.

Figure 3.24: Maximum principle strain (μstrain) measured at +45˚ from the longitudinal shaft axis varied little between opposite ends of the test section (10 in apart) and decreases by ~54% between the shaft and the FeGa patch (mounted in the center of the test section).

Figure 3.25: The dynamic test setup included a motor to drive the shaft, a speed controller to vary RPM, and a magnetic particle brake to apply torque to the test section.

Figure 3.26: Brake heat output (W) less than 110 W is plotted as torque (in-lb) and RPM are varied.

Figure 3.27: Torque (in-lb) increased bi-directionally as input voltage to the magnetic particle brake (V) was increased.

Figure 4.1: The Hall effect sensor signal (mV) is shown for six tests in (a) blue, cyan, and green while three +50 in-lb torques are applied and in red, pink, and black as three -50 in-lb torques are applied, with (b) a zoomed image of the first load application.

Figure 4.2: The filtered Hall effect sensor signal was sampled to determine the (a) mean voltage output over 10 seconds and b) signal drift over 10 seconds.

Figure 4.3: An increase in output magnitude was observed for all samples after changes were made to the adhesive application protocol.

Figure 4.4: The tendency of drift to increase or decrease as larger torques were bi-directionally applied varied on a sample-by-sample basis.

Figure 4.5: A 0.15 mm thick FeAl ring was tested with a load measured by the commercial torque sensor (blue) and with the Hall effect sensor (red) showing evidence of error in the no-load response between measurements. Loads are applied between 0:20 – 0:40, 0:50 – 1:10, and 1:20 – 1:40.

Figure 4.6: FeAl Patches provided a larger output signal than FeGa across most cases.

Figure 4.7: Over three individual test cases, FeGa and FeAl Patches experienced the highest drift (still < 2.5% mean) at ±50 in-lb and generally under positive loading.

Figure 4.8: The sensitivity (mV/in-lb) is considered as a change in Hall effect sensor output (mV) over a range of applied torques (in-lb)

Figure 4.9: A span-five moving average filter reduced peak Hall effect sensor output values by ~450 mV @ 2000 RPM.

Figure 4.10: FeAl at 500RPM produced filtered peaks ~30mV less than the maximum raw recorded values.

Figure 4.11: A span-three moving average filter was applied to the raw Hall effect sensor data to eliminate outliers and provide an estimate for a mean peak value for each rotation, here tested at 1000 RPM.

Figure 4.12: FeAl at 2000 RPM produced filtered peaks ~80mV less than the maximum raw recorded values.

Figure 4.13: Each FeAl ring covers the majority of the circumference of the shaft, such that the troughs represent a sliver of aluminum passing under the Hall effect sensor, shown here at 500 RPM with a 1000 Hz sampling rate.

Figure 4.14: Peak FeAl Ring output experiences minimal reduction in response due to the implementation of a span-three moving average filter at a speed of 2000 RPM and a sampling rate of (a) 1000 Hz and (b) no reduction at 10000 Hz. Peak signal for a FeGa paint sample experiences minimal reduction due to implementation of a moving average filter at a sampling rate of (c) 1000 Hz and (d) no reduction at 10000 Hz.

Figure 4.15: A maximum Hall effect sensor value was calculated for each rotation, and the results from the last 5 seconds were averaged to generate a "Mean Peak Signal."

Figure 4.16: Hall sensors mounted directly over the aluminum shaft measured an increase of ~10mV between minimum and maximum torque application.

Figure 4.17: Similar responses were observed in the FeGa Patch sample for loads > ~55 in-lb as measured by two separate WiMET sensors.

Figure 4.18: Similar responses were observed in the FeAl Patch sample for loads > ~50 in-lb as measured by two separate WiMET sensors.

Figure 4.19: Similar responses were observed in FeAl Ring 1 for loads > ~40 in-lb as measured by two separate WiMET sensors.

Figure 4.20: Slightly different responses were observed in the FeGa Paint sample for loads > ~50 in-lb as measured by two separate WiMET sensors.

Figure 4.21: A higher sloped trendline was observed under positive rotation than under negative rotation for the FeGa Patch.

Figure 4.22: A higher sloped trendline was observed under positive rotation than under negative rotation for the FeAl Patch.

Figure 4.23: A higher sloped trendline was observed under positive rotation than under negative rotation for the FeAl Ring.

Figure 4.24: A higher sloped trendline was observed under positive rotation than under negative rotation for the FeGa Paint.

Figure 4.25: Hall effect sensor output (V) decreased at low torque application, but increased in a linear fashion for torques in excess of 50 in-lb for FeGa samples.

Figure 4.26: Similar sensitivities were observed between 0 – 2000 RPM for the FeGa patch sample

Figure 4.27: Hall effect sensor output (V) decreased at low torque application, but increased in a linear fashion for torques in excess of 50 in-lb with a lower sensitivity response at 2000 RPM than at 0 – 1500 RPM for FeAl samples.

Figure 4.28: Hall effect sensor output voltage (V) increased non-linearly for torques < ~50 in-lb for the FeAl Ring sample and increased linearly for torques > ~50 in-lb with similarly sloped linear trendlines between 500 – 2000 RPM.

Figure 4.29: Hall effect sensor output voltage (V) increased by a maximum of ~10mV for the FeGa Paint sample as applied torque increased (NOTE: Scale of vertical axis is triple compared with graphs of other samples in this section).

Figure 4.30: This updated WiMET operating window is based on estimates from FeGa sensor curves generated by Atulasimha et al., modeling results from Chapter 2, and testing results from Chapters 3 and 4.

Figure 4.31: The updated WiMET configuration provided an output magnitude and sensitivity ~10 times greater than the prototype between ~ 44 and 188 in-lb.

Figure A.1: EBSD-scanned image of a patch of Goss-textured FeGa rolled sheet that was used for the prototype WiMET sensor by Raghunath et al. with a <100> orientation along the length of the shaft.

Figure A.2: EBSD-scanned image of FeAl rolled sheet that was used to create "FeAl Patch" sample for WiMET testing with a <100> orientation along the circumference of the shaft.

Figure B.1: Axial stress subscripts correspond to the stress orthogonal to a plane, while shear stress subscripts correspond to the stress on a plane in the direction of another axis.

Figure B.2: Magnetic flux lines are expected to travel though the magnetostrictive patch along the axis of the shaft and "leak" through the edge of the material to be detected by a Hall effect sensor mounted above.

Figure B.3: The FeGa patch experiences shear stress τ across the *1*-face and *3*-face as torsion is applied, and the material is magnetized along the *3*-axis as flux lines travel down the length of the shaft.

Figure C.1: Hall effect sensor mean voltage output (mV) increased as applied torque (in-lb) increased for each material sample in preliminary BDQS testing. Error bars indicate standard error of the mean.

Figure C.2: FeAl samples experienced signal drift < 1% of mean signal over all test cases, while FeGa Patch 2 exhibited drift > 6% under negative torsional loading.

Figure C.3: Hall effect sensor mean voltage output (mV) is plotted against applied torque (in-lb) for randomized-input BDQS testing. Error bars show standard mean error.

Figure C.4: Hall effect sensor drift (% mean voltage) is plotted against applied torque (in-lb) for randomized BDQS testing.

Figure D.1: Magnitude of sensor drift (% mean voltage) generally tended to be greater when observed over longer periods of time.

List of Equations

Equation 1.1: Magnetostriction as the change in length of a material

Equation 2.1: Shear stress in a shaft cross-section as a fraction of maximum surface shear stress

Equation 2.2 – 2.6: Deriving maximum shear stress in a cylindrical shaft under torsional loading

Equation 2.7: Polar moment of inertia of a solid cylindrical shaft

Equation 2.8: Shaft under axial and torsional loads, Mohr's Circle center point *C*

Equation 2.9: Shaft under axial and torsional loads, Mohr's Circle radius *R*

Equation 2.10: Shaft under axial and torsional loads, Mohr's Circle principle stress σ_1

Equation 2.11: Shaft under axial and torsional loads, Mohr's Circle principle stress σ_2

Equation 2.12: Shaft under axial and torsional loads, Mohr's Circle rotation angle θ

Equation 2.13: Shaft in pure torsion, Mohr's Circle center point *C*

Equation 2.14: Shaft in pure torsion, Mohr's Circle radius *R*

Equation 2.15: Shaft in pure torsion, Mohr's Circle principle stress σ_1

Equation 2.16: Shaft in pure torsion, Mohr's Circle principle stress σ_2

Equation 2.17: Shaft in pure torsion, Mohr's Circle rotation angle θ

Equation 2.18: Piezo-magnetic constitutive actuator equation

Equation 2.19: Piezo-magnetic constitutive sensor equation

Equation 2.20: Total force applied to COMSOL model

Equation 3.1: Torque application

Equation 3.2: Adhesive scaling relationship

Equation 3.3: Twist angle for solid rod in torsion

Equation 3.4: Magnetic particle brake heat output

Equation 4.1: Standard error of the mean

Equation 4.2: Drift as a percent of mean signal magnitude

Equation 4.3: Sensitivity of WiMET sensor response

Equation B.1: Expanded piezo-magnetic constitutive sensor equation

Equation B.2: Simplified piezo-magnetic constitutive sensor equation

Chapter 1: Introduction

1.1 Motivation

The ability to measure torque in a rotating system provides data on the time-varying loads experienced by the rotating system. During testing and regular operation of high-speed drive train systems in the automotive and rotorcraft industries, the ability to measure torque is necessary in the context of system health monitoring, condition-based monitoring, and usage-based monitoring. Many torque sensing products exist to address this need, but readily available systems often require extensive modification of test setups, add excessive weight to the system, occupy prohibitively large dimensions, or require the use of noise-prone integration methods such as slip rings or wireless methods to transfer signal between rotating and stationary reference frames. Therefore, a compact system that can accurately and reliably measure torque from a non-rotating frame of reference would provide a highly desirable solution to this need.

The advent of advances in the development of rolled sheet magnetostrictive materials has provided the opportunity to develop a non-contact torque sensor using a new type of integrated structural sensing element. A patch of magnetostrictive material is bonded to a shaft in a manner that a change in shaft torque produces a change in the magnetic state of the magnetostrictive material and, in turn, a readily measurable change in the stray magnetic field lines in air above the patch. This thesis explores the feasibility of using rolled sheet samples of Galfenol and Alfenol, iron alloys of Gallium and Aluminum respectively, as magnetostrictive sensing elements to measure variations in torque applied to stationary and rotating drive train shafts.

1.2 Torque Sensor State of the Art

The automotive industry is primarily interested in torque sensors in the context of measuring torque in steering wheels for electric power steering (EPS), driveshafts (transmission-out), and clutchshafts (engine-out) [9]. Torque sensors for steering wheels are currently more developed than systems that measure drive trains due to the rapid development of EPS systems and the more demanding operating requirements of drive train systems [9]. As such, there is a need for sensors that measure the torque in drive train systems. State of the art technology currently enables users to measure the torque present in a rotating drive train using technologies that can be grouped into two broad categories: torsion-bar twist-angle sensors, and magneto-elastic sensors [9].

1.2.1 Torsion-Bar Twist-Angle Sensors

Torsion-bar twist-angle sensors operate by measuring the twist in a shaft caused by the application of a torque. Several configurations of torsion-bar twist-angle torque sensors are of particular interest within the automotive industry [10].

Twist angle can be measured potentiometrically, with the use of sliding contacts to measure torque and relative angular position. Here, the sensor must be installed in-line with the shaft. Torque applied to the shaft alters the relative position between a torque output contact in relation to a reference voltage contact and a ground contact. The torque output contact provides an output voltage corresponding to the amount of torque applied to the system. Another similar contact tracks angular position as loads are applied [11]. This is the type of commercially available torque sensor that is currently used on this project's benchtop test setup.

Twist can also be measured using the torsion-bar twist-angle method using noncontact means. An optical displacement sensor can be used to measure the rotary displacement between two rotating shafts connected by a torsion bar. Light shines onto an array of photodetectors through slotted coaxial disks mounted on each shaft. Outputs from the photodetectors are processed to determine the torque or shaft displacement [12]. These products provide accurate response, with high signal to noise, but require systems with long slender test sections to achieve this result.

Using a similar system with two shafts connected to a torsion bar, it is also possible to determine torque magnetically, using displaceable air gaps [13]. Twist can also be detected electrically, using a pair of coils whose inductances vary in opposing directions with changes in torque and a differential amplifier circuit that receives and differentially amplifies a pair of detection voltages induced by said coils [14].

1.2.2 Magneto-Elastic Torque Sensors

Magneto-elastic detection methods are primarily non-contact, and allow for torque detection in solid shafts. Here, torque is measured either by detecting stress-induced changes in the magnetic permeability of the surface layer of a shaft or by detecting the effects of a torque-induced rotation of magnetic domains in surface layers of the shaft. Fleming identifies a few types of magneto-elastic sensors of interest to the automobile industry [9].

One steering wheel electric power steering (EPS) torque sensor uses a magnetic encoder ring and a Hall effect sensor to wirelessly measure torque. When a steering wheel is turned by the user, a torsion bar attaching the wheel to a magnetized encoder ring twists.

The encoder ring is angularly displaced relative to two co-rotating rings with ferromagnetic teeth. The flux across the teeth caused by the angular displacement of a rotating magnetic encoder ring creates the output torque signal. As greater torque is applied to the steering wheel, a greater twist angle occurs, causing a greater displacement of the poles of the encoder with respect to the ferromagnetic teeth, causing greater flux, causing greater signal output. The sensor design is compact, but it must be installed in-line with the steering wheel. It can accommodate at most ±8˚ of torsion bar twist. [9] [15] [16].

The Surface Acoustic Wave (SAW) Torque sensor is also used for steering wheel torque measurement. This device takes advantage of the influence of strain on the propagation velocity of acoustic waves. Its sensing elements are aligned with the principal lines of tensile and compressive torsional strain in the rotating shaft, which occur at ±45˚ from the shaft longitudinal axis. A piezoelectric transducer is mounted on a quartz substrate, which is in turn mounted to the shaft. The transducer generates acoustic waves that propagate through the quartz and along the principal lines of strain before returning to the transducer. Torque measurement is achieved by the differential measurement from two ± 45˚ resonators. The system is a batteryless, small, lightweight, and noncontact means of strain measurement caused by shaft torque that does not necessitate the use of a torque bar, unlike some comparable devices. However, the test shaft must have a flat surface machined into its curvature to allow for the placement of these sensors [9] [17].

Magneto-elastic torque sensors also allow for non-contact torque measurement without the use of a battery for the sensing element or the use of a torsion bar. MagCanica Inc (San Diego, CA) provides driveshaft and clutchshaft torque sensors for F1 racing vehicles that measure torque in this way. MagCanica's magneto-elastic torque sensors

measure torque in a solid shaft as a result of shaft stress, rather than strain. A circumferential region of a magneto-elastic shaft is permanently magnetized such that magnetic domains in the material are oriented circumferentially. As torque is applied to the shaft, magnetic domains realign, and a stronger magnetic field is produced in the axial direction; in this case, this is the longitudinal shaft axis. This change in field is measured by axially oriented flux-gate detectors, which provide the torque signal output. MagCanica's sensor provides a non-invasive, non-contact, wireless measurement of torque in a driveshaft. However, the calibration of each sensor is heavily dependent on the reproducibility of the magneto-elastic properties of each shaft. These properties are not typically specified or controlled by manufacturers, and as such it is difficult to guarantee consistent sensor performance on a part-to-part basis, which is overcome by conducting part-specific calibration [9], [18]–[22].

1.3 Magnetostriction

Magneto-elastic torque sensors operate based on the principles of magnetostriction, a phenomenon whereby the magnetic and elastic properties of a material are coupled. Upon an application of magnetic field, the dimensions of a magnetostrictive material will change, and upon deforming, a magnetostrictive material exposed to a "biasing" magnetic field, will undergo a measurable change in magnetization. In this way, a magnetostrictive material is able to transform mechanical energy to magnetic energy, and vice versa [2]. Magnetostrictive materials can be used for a wide range of applications as both actuators and sensors.

1.3.1 Crystal Axes and Magnetic Anisotropy

An understanding of crystal axes and magnetic anisotropy are necessary to understand magnetostriction, as the mechanical and electromagnetic properties of a magnetostrictive material vary depending on the crystal axis along which they are measured. Figure 1.1 defines crystal axes and direction vectors. The sides of the cube are unit length, and the cube axes are defined according to the Miller index notation. Vector direction is described as [*u v w*] and vectors that are equivalent because of symmetry are described as <*u v w*>. Planes perpendicular to a [*u v w*] direction are described as (*u v w*), and planes that are equivalent because of symmetry are described as {*u v w*}.

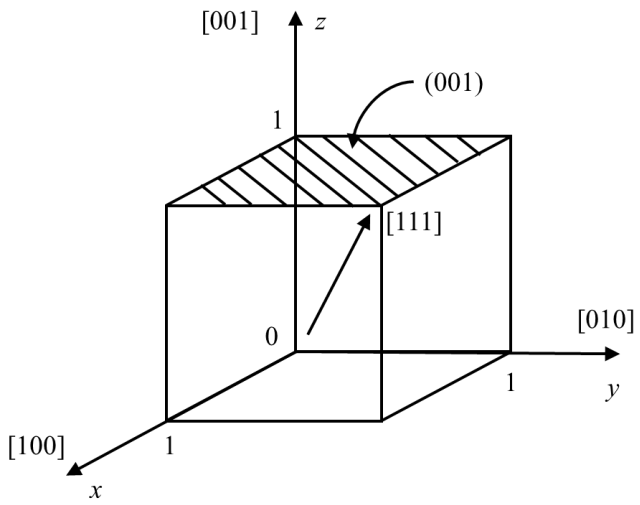

Figure 1.1: A unit cell with Miller index notation depicts the [100], [010], [001], and [111] directions and the (001) plane.

When unit cells are oriented randomly throughout a material, the material will exhibit isotropic macro-scale properties. However, if enough domains – groups of unit cells – are oriented in a particular direction, the macro-scale behavior can become anisotropic.

In the case of magnetostrictive materials, magnetic anisotropy is of particular concern. Here, the internal energy of a material is minimized by the formation of pairs of antiparallel magnetic domains, in which magnetization preferentially occurs in particular directions. These directions are often referred to as the "easy" axes [2]. In the magnetostrictive materials Galfenol and Alfenol, which are the focus of this thesis, the easy axes are the family of <001> directions. In the absence of external magnetic fields and mechanical stress, internal energy in these alloys in minimized with the formation of antiparallel domains randomly distributed with roughly one third aligned along the [100] direction, one third along the [010] direction, and the remaining third along the [001] direction.

1.3.2 Magnetostrictive Effect

When a magnetostrictive material is magnetized, its randomly oriented domains align in the direction of the magnetization, and cause deformation in the material in the direction of the applied magnetic field. This is referred to as the Joule Effect, depicted in Figure 1.2, and this is the mode in which magnetostrictive actuators operate.

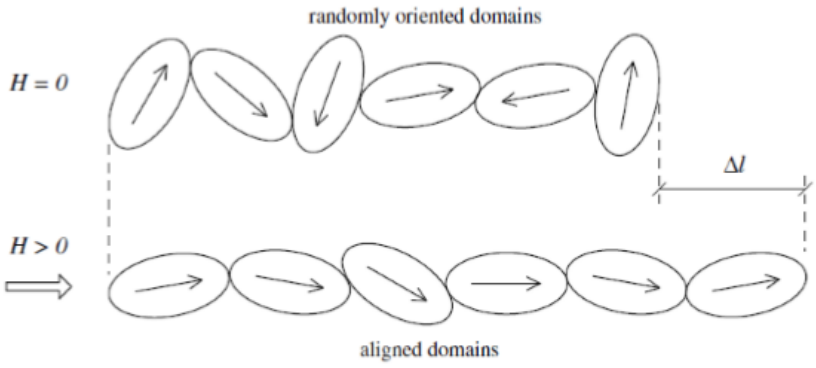

Figure 1.2: The application of a magnetic field induces magnetostriction [2].

When the direction of an applied magnetic field is reversed, but the magnitude remains the same, the response will be equal and opposite, as shown in the lower two sketches of Figure 1.3. Again, the domains align with the direction of the applied magnetic field.

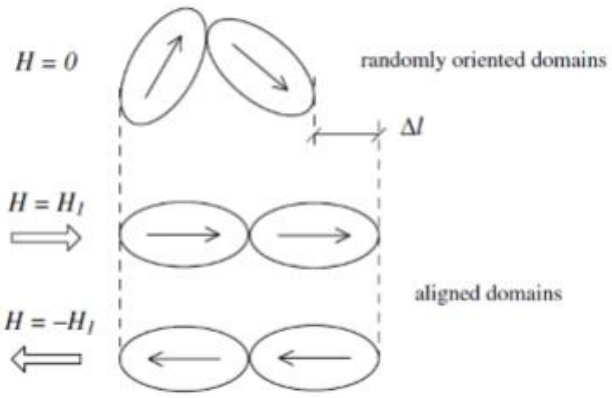

Figure 1.3: Strain occurs in the direction of magnetization and maximum or saturation strain magnitude is independent of field polarity [2].

In this way, magnetostriction λ can be represented as:

$$\lambda = \frac{\Delta L}{L} \tag{1.1}$$

Here, L is the length of the material prior to application of an external magnetic field, and ΔL is the change in length of the material due to the reorientation of magnetic domains to align with an applied external magnetic field. Saturation magnetostriction occurs when all magnetic domains within the magnetostrictive material are fully oriented along the axis where magnetization occurs. Here, no further extension can take place.

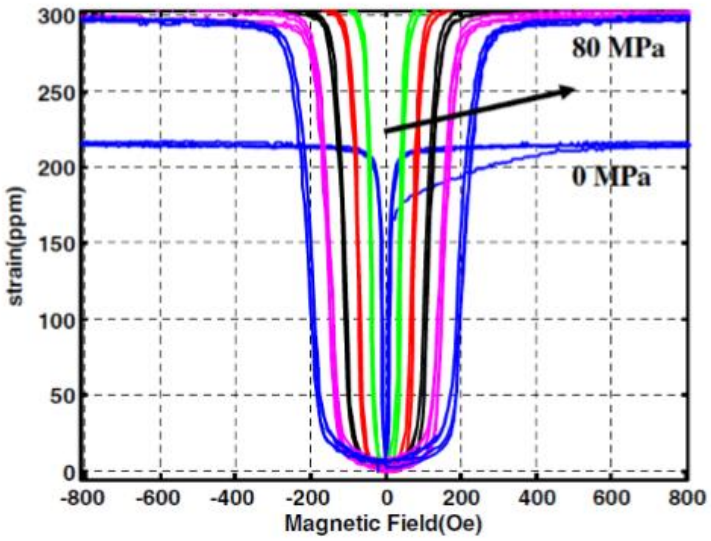

Figure 1.4: Experimental λ-H curves of 19 at.% Ga, furnace cooled, <100> oriented, single-crystal $Fe_{81}Ga_{19}$ under compressive prestress of 0, 15, 30, 45, 60, and 80 MPa, obtained by Atulasimha [4].

This actuation behavior is characterized for a cylindrical sample of <100> oriented single-crystal $Fe_{81}Ga_{19}$ in Figure 1.4. This sample was machined to have a magnetic easy axis aligned along the length of the cylinder, and both the magnetic field and the compressive pre-stress are applied along the cylinder axis. Here, saturation can be observed for a range of applied pre-stresses; saturation occurs at the end of the linear region of response, when the magnetic field grows strong enough to reorient all magnetic domains parallel to the applied field [4].

1.3.3 Inverse Magnetostrictive Effect

The inverse of the Joule Effect occurs when a mechanical stress is applied to a sample magnetized with a DC bias. When a magnetic bias is applied to an unloaded

material, the domains align themselves along the easy axis closest to the direction of magnetization. When a compressive stress is applied along that direction, the magnetic domains are reoriented to the easy axes that are perpendicular to the direction of the field. This measurable change in magnetization due to deformation, known as the Villari Effect, or inverse magnetostriction, is the mode in which magnetostrictive WiMET sensors presented in this thesis operate.

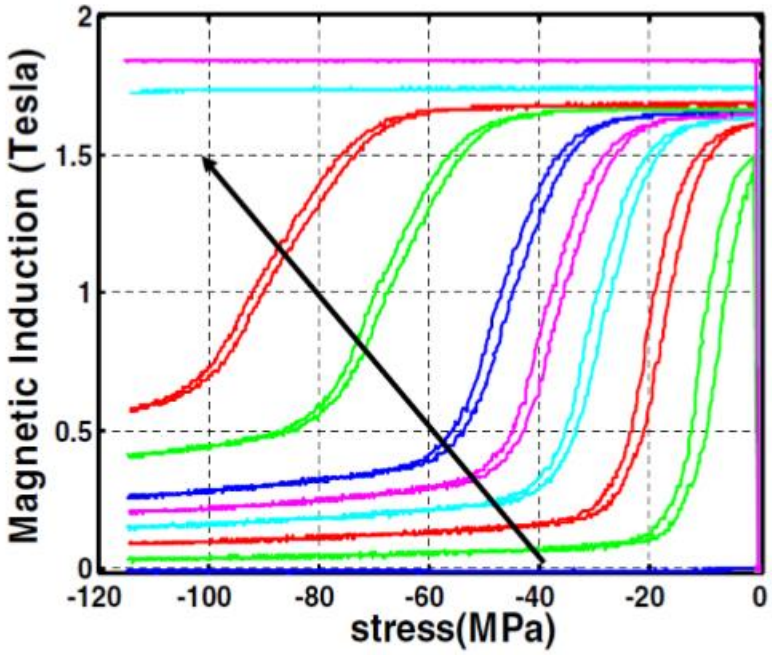

Figure 1.5: Experimental *B*-σ curves of furnace cooled, <100> oriented, single-crystal $Fe_{81}Ga_{19}$ under constant magnetic fields of 0, 22.3, 44.6, 66.9, 89.1, 111, 167, 223, 446, and 891 Oe, obtained by Atulasimha et al. [4].

Figure 1.5 demonstrates the Villari Effect. It plots magnetic induction against applied compressive stress for the Figure 1.4 cylindrical sample of <100> oriented single-

crystal $Fe_{81}Ga_{19}$. The balance of internal magnetic energy and stress energy in the sample is evident, as for higher DC magnetic fields, a higher compressive stress is required to rotate domains away from the applied field direction into the easy axes that are perpendicular to the direction of compressive stress and applied field. In this figure, the compressive stresses never fully rotated all domains away from the rod length. This suggests the influence of additional contributions to the sample internal energy, for example shape anisotropy, which would promote the tendency for magnetization to be oriented along the length of a cylindrical sample [4].

1.3.4 Magnetostrictive Materials

Table 1.1: Material properties of magnetostrictive materials [1]–[8]

	Iron	**Nickel**	**Terfenol – D**	**Galfenol**	**Alfenol**
Saturation Magnetization (T)	0.17	0.05	1	1.4 – 1.8	1.5
Hysteresis in λ-H and B-H Curves	Low	Low	Moderate	Very Low	Very Low
Saturation Magnetostriction (ppm)	-24	-66	1600-2400	150 - 420	100 - 200
Modulus of Elasticity (GPa)	200	207	25-35	65	68
Ultimate Tensile Strength (MPa)	400	500	30	580	606
Mechanical Properties	Flexible	Flexible	Brittle	Flexible	Flexible

Iron and nickel are two of the materials in which magnetostriction was first observed, in the 1840s by James Joule [2]. Both provide low saturation magnetization, meaning that they have a limited operating range for sensing applications. However, they

offer favorable mechanical properties, with elastic moduli of ~200 GPa and ultimate tensile strengths between 400 – 500 MPa.

Since the creation of Terfenol-D by Naval Ordinance Laboratory researcher Arthur Clark and his colleagues, it has seen use in a variety of applications as a magnetostrictive actuator and transducer [23], [24]. Although it exhibits high saturation magnetization, see Table 1.1, it is difficult to machine or shape due to its brittle nature, and is thus less attractive for use as a sensor in an integrated smart structure. Iron and nickel have more desirable mechanical properties, but possess much lower magnetostriction (roughly two orders of magnitude lower) and much lower saturation magnetization (one to two orders of magnitude lower).

Galfenol (FeGa) is a ferromagnetic iron-gallium alloy first created by researchers at the Naval Surface Warfare Lab [25]. Galfenol has promising mechanical and load bearing properties, similar to those of iron. Unlike Terfenol-D, FeGa alloys (with Ga content less than ~20%) have been shown to be machinable, ductile, rollable, and weldable [26]. FeGa alloys exhibit magnetostriction on the order of 350ppm under magnetic fields as low as ~100 Oe [26]. FeGa alloys have low hysteresis, demonstrate tensile strength on the order of 500 MPa, and see little variation in macromechanical properties between -20 ˚C and 80˚C, as seen in Figure 1.6 [26].

For applications involving sensing and energy harvesting, saturation magnetization of between 1.4 and 1.8 T is observed depending on material composition, grain orientation, and applied field [4]. Thermo-mechanical processing methods (rolling and subsequent high-temperature atmospheric anneals) are effective for producing Goss-textured (cube on edge) rolled sheet FeGa alloys with one in-plane <100> easy axis along the rolling direction

that make effective sensors and energy harvesters [27]. Additionally, FeGa alloys of Fe-15, 20, and 27.5 at.%, Ga have proven to exhibit good corrosion resistance, which is promising for applications in oily or aqueous environments [5], [28]. Considered together, these characteristics make FeGa alloys excellent candidates for structural sensing applications such as in devices that detect rotational torque and fluid flow [1], [3], [29], [30]. FeGa alloys have also seen use in experimental bending-mode energy harvesters, which convert vibrational energy into electrical energy [31], [32].

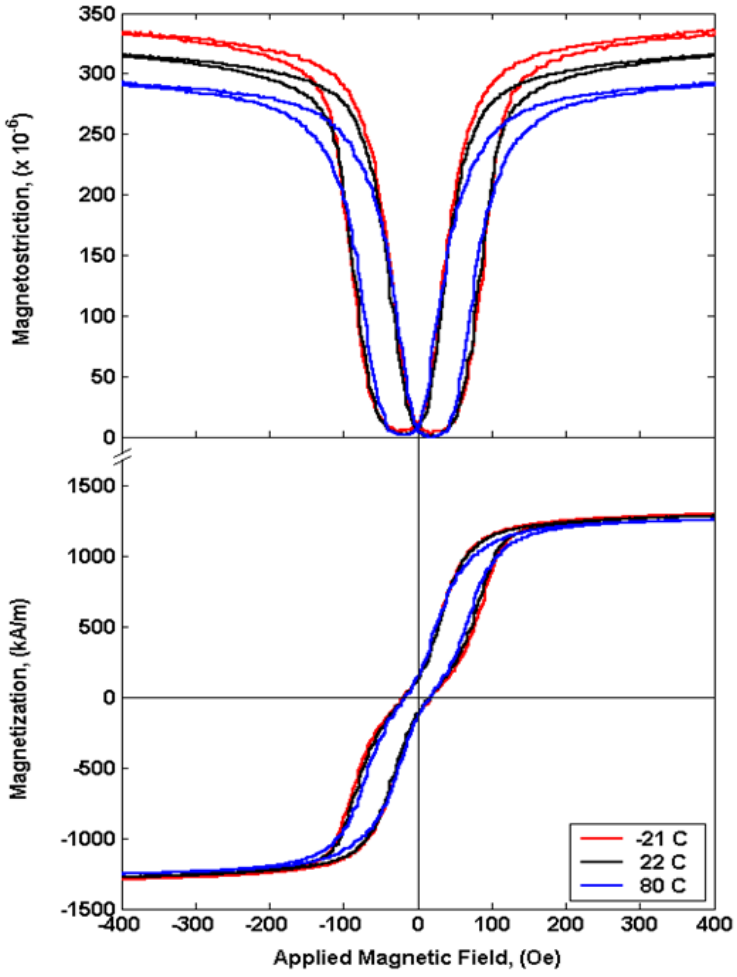

Figure 1.6: Magnetostriction (top) and magnetization (bottom) vary in a FeGa sample as applied magnetic field (Oe) is increased at -21˚C, 22˚C, and 80˚C [26].

Alfenol (FeAl) is a ferromagnetic iron-aluminum alloy, with aluminum content less than ~20%, that has macromechanical and magneto-elastic properties which are comparable to those of FeGa (see Table 1.1). Like FeGa, FeAl offers higher ductility and tensile strength when compared to Terfenol D. Although saturation magnetostriction λ for FeAl is ~40% smaller than in FeGa, saturation magnetization M_s is nearly the same, meaning that the two materials should offer comparable performance in terms of output potential in the sensing and energy harvesting modes [3], [8]. Both materials exhibit a body-centered cubic or "bcc" atomic lattice structure and <100> easy magnetostriction axes [33]. Galvanized FeAl whiskers made from Goss-textured rolled thin sheet utilized experimentally as flow sensors in aqueous environments have demonstrated resistance to corrosion, the ability to withstand severe bending stresses, and the ability to provide a net voltage response due to time varying magnetic induction proportional to applied tip loads and deflection [3], [27]. Additionally, aluminum is abundant with a relatively low material cost compared to gallium. All things considered, these characteristics allowed for the creation of FeAl sensors with similar performance and lower cost when compared to FeGa sensing elements, and as such, both FeGa and FeAl samples were utilized when testing different configurations of sensors in this thesis.

1.4 Wireless Magneto-Elastic Torque (WiMET) Sensor

Results of a preliminary study of a Galfenol wireless magneto-elastic torque (WiMET) sensor that is the focus of this thesis are summarized in a work by Raghunath et al. [34], [35]. The WiMET sensor functions by using the aforementioned Villari Effect to measure changes in magnetic flux density leaking from the edges of a Galfenol sensing

element as loads are applied to the shaft. In their work, Raghunath et al. used Crystal Bond (a heat sensitive glue) to attach a thin, rectangular magnetostrictive sensing element to an aluminum shaft. A magnet and Hall effect sensor were attached to a high permeability flux piece and mounted to a height gage above the patch, with the Hall effect sensor positioned over the edge of the patch, as seen in Figure 1.7.

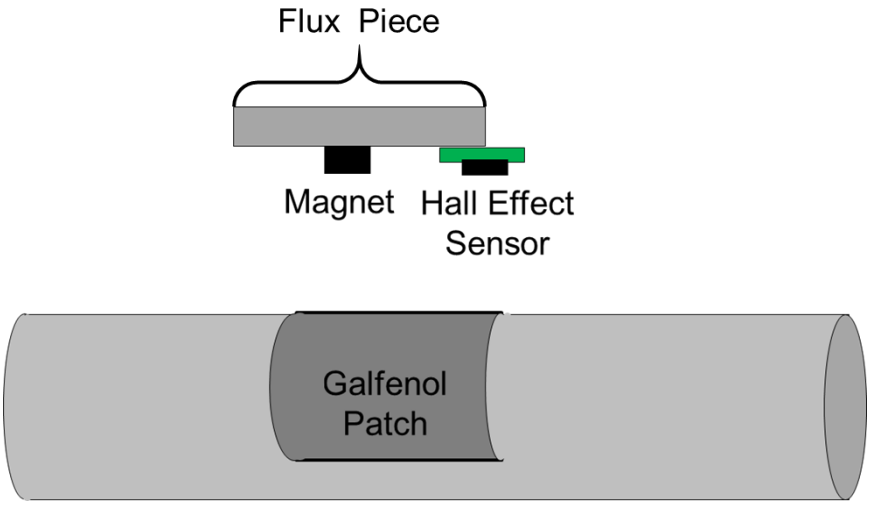

Figure 1.7: The WiMET sensor is primarily composed of a magnetostrictive patch mounted on a shaft, with a Hall effect sensor and biasing magnet mounted to a high permeability flux piece above the patch (based on Raghunath et al.) [35].

The magnet imparts a magnetic bias to the magnetostrictive sensing element, as seen in Figure 1.8. As torque is applied to the shaft, strain is transferred from the surface of the shaft, through the adhesive, and into the magnetostrictive sensing element, as seen in Figure 1.9.

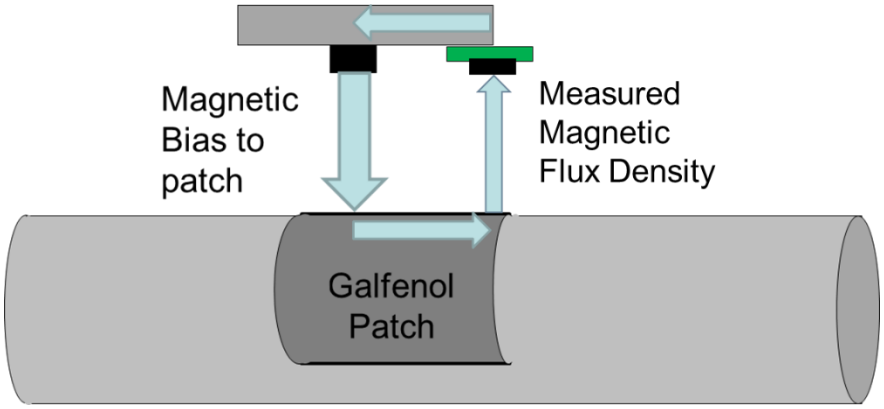

Figure 1.8: The magnet applies a magnetic bias to the magnetostrictive sensing element and stray fields from the patch are detected by the Hall effect sensor. Blue arrows are included to illustrate the flux path whereby flux from the permanent magnet flows through air to the magnetostrictive patch, through the patch, through air and the Hall effect sensor to the flux piece, and back to the permanent magnet.

As the magnetostrictive sensing element is strained, as in Figure 1.9, a change in magnetic flux density is measurable around the edges of the patch. The Hall effect sensor that is mounted above the shaft measures this change in flux density. This torque sensor can be considered a non-contact solution for torque measurement, as no cabling is run between the stationary and rotating reference frames. Note the change in size of the arrows between Figure 1.8 and Figure 1.9 indicate an increase in measured field, but depending on the direction and magnitude of torque applied, decreases and increases in signal were observed.

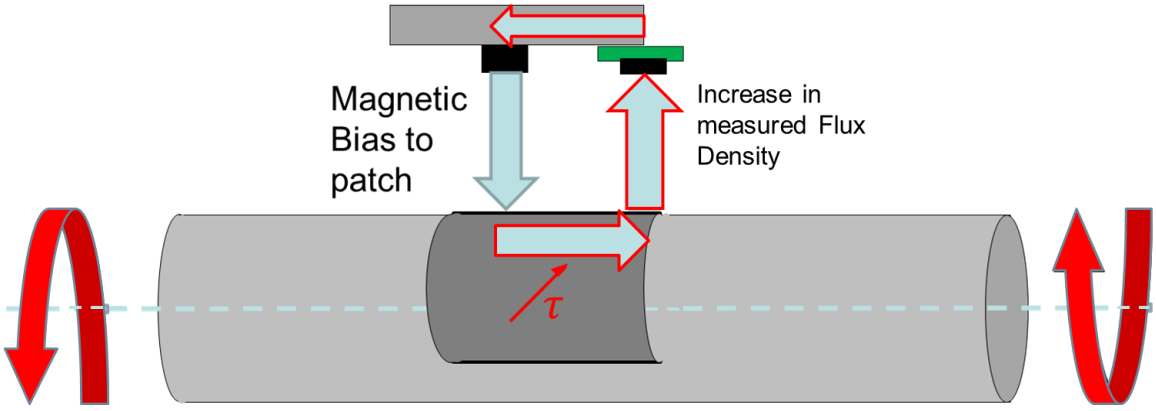

Figure 1.9: As a torque is applied to the shaft (indicated by arrows at both ends of the shaft), shear stress in the patch along the principle axis, i.e. rotated 45˚ for the axis of the shaft (shown with thin red arrow labels τ), induces a change in magnetic flux density in the magnetostrictive patch and as a result throughout the magnetic flux path (indicated by red outline on the blue arrows depicting the flux circuit). The Hall effect sensor measures the change in magnetic flux in the air gap between the patch and the flux piece.

The sensor developed by Raghunath et al. responded linearly to changes in applied torque with corresponding changes in Hall effect sensor output voltage for torques < ~50 in-lb. As seen in a time-domain comparison of commercial torque sensor output and Hall effect sensor output in Figure 1.10, the prototype WiMET sensor lost linearity in response at torques in excess of ~50 in-lb. This effect can be seen at speeds between 360 and 1800 RPM in Figure 1.11 [35].

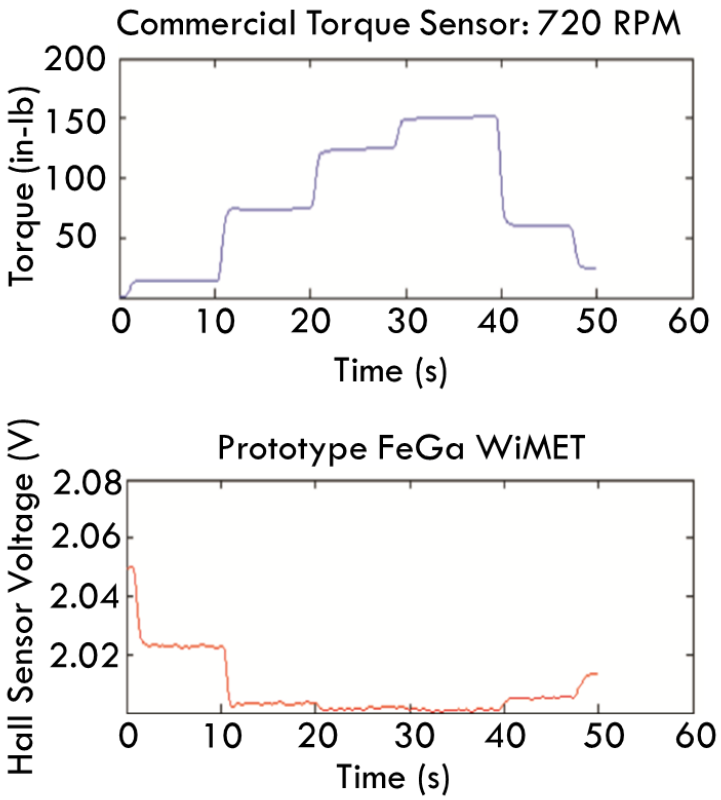

Figure 1.10: Commercial torque sensor (in-lb) and Hall effect sensor (mV) outputs plotted over time demonstrate a reduced level of response for applied loads >~50 in-lb in upper and lower graphs, respectively [35].

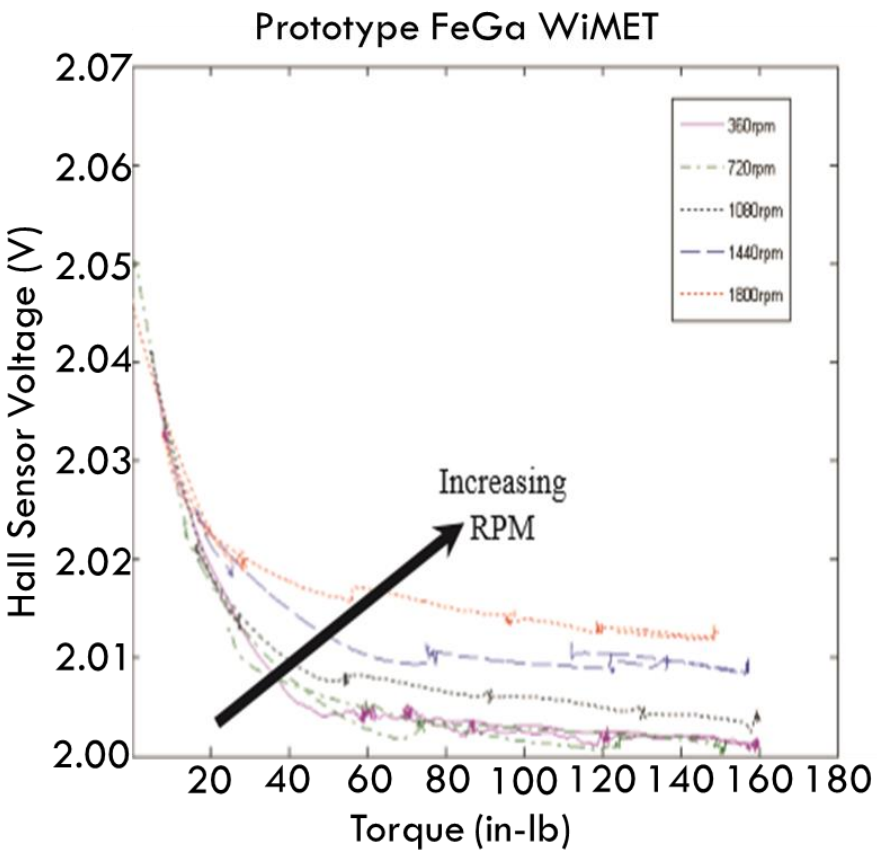

Figure 1.11: A decrease in response sensitivity is noted over a range of RPMs for loads in excess of ~20 in-lb [35].

The preliminary results from Raghunath et al. on their non-contact Galfenol torque sensor provided motivation to better understand the response of this configuration of non-contact magnetostrictive torque sensor and to consider the performance potential of an Alfenol torque sensor. With the input of collaborators at the US Army Research Laboratory (ARL), the following list of research objectives was composed to address challenges in further characterizing sensor response:

1. Investigate thermal stability.
2. Investigate the sensitivity of performance in the presence of shaft movement.

3. Investigate methods for bonding the magnetostrictive patches to shafts of different materials, e.g. aluminum and composite shafts.
4. Investigate requirements for design configurations that match operation load and RPM ranges needed for monitoring performance of full-scale engines and drive train systems.
5. Investigate methods for in-situ calibration.
6. Validate sensitivity and accuracy in realistic operation environments, such as on the ARL high speed test rigs rather than the University benchtop setup.

The scope of this thesis addresses Task 2 and Task 3, and planning for Tasks 4, 5, and 6 is discussed in the future work section. Task 1 was conducted by other students in parallel with this work. Testing in Chapter 3 evaluates adhesive bonding methods on steel and aluminum. Results from static and dynamic testing in Chapter 4 are used to evaluate the output of the sensor and its sensitivity to varied applied load and rotational speed. Chapter 5 summarizes insights from the experimental results and provides details on suggestions for future work and additional planning and design considerations for testing to take place on drive train systems at Aberdeen Proving Grounds.

1.5 Experimental Investigation Overview

As the next step toward developing this WiMET sensor technology, and to aid in determining if it has the potential to provide high sensitivity torque measurements in a compact non-contact system that is mounted passively to a shaft and that can be easily

installed or retrofitted in existing systems, this thesis addresses the following several outstanding challenges identified in the preliminary WiMET study.

In this thesis, the signal response of a wireless magneto-elastic torque sensor is evaluated in both quasi-static and dynamic modes using both Galfenol and Alfenol as magnetostrictive sensing elements. The tests performed in this thesis were divided into the following parts: In Chapter 2, a modeling effort was carried out in COMSOL in order to characterize the stresses and applied magnetic fields that would act on the shaft and magnetostrictive element of a proposed sensor configuration. Chapter 3 describes the experimental setup used for bi-directional quasi-static (BDQS) tests and dynamic tests. It includes discussion of the steps used in determining test protocols. Permanent magnet and Hall effect sensor positioning were varied and improvements were made to the process by which the magnetostrictive element was bonded to the shaft in order to maximize output signal-to-noise. In Chapter 4, the WiMET sensor underwent a battery of BDQS tests to characterize the magnitude and drift of changes in magnetic induction produced by a variety of magnetostrictive samples which varied in composition and shape. Chapter 4 also provides results from dynamic testing of these magnetostrictive sensing elements to characterize signal response as RPM, applied torque, and rotation direction were varied. Chapter 5 summarizes modeling and experimental results and concludes with a discussion of proposed future work.

Chapter 2: Modeling and Simulation

This chapter discusses modeling efforts made to better understand the mechanical and magnetic inputs acting on patches of magnetostrictive material in torsion, and it suggests a resultant operating range for the sensor as a function of input torque, applied magnetic field, and magnetostrictive patch thickness in the WiMET sensor configuration. First, a coordinate system was established to denote the direction of applied torque, stresses, and magnetic fields. A series of equations derived from a Mohr's circle analysis of a rod in torsion was then considered to provide a prediction of the primary stresses acting on the WiMET sensor. A COMSOL Multiphysics model was developed in order to estimate the magnitude of stresses acting on the surfaces of the shaft and magnetostrictive material using a Structural Mechanics module, and a Magnetics module was separately implemented to estimate the distribution of applied magnetic fields and magnetic flux density across the prototype WiMET sensor configuration. These estimations were then compared to experimental B-σ curves for FeGa produced by Atulasimha et al. to predict a window of operation for the WiMET sensor.

2.1 Coordinate Systems

Using a traditional Cartesian (x,y,z) coordinate system, the longitudinal axis of the shaft is defined as the x-axis, the z-axis runs normal to the x-axis in the direction of the Hall effect sensor, and the y-axis completes the traditional right-handed system. An additional Cylindrical (r,φ,a) coordinate system was established for ease of torque application in COMSOL modeling such that the r-coordinate is defined as the radial distance from the x-axis of the shaft, φ is defined as the angle of rotation about the x-axis, where the reference

direction $\varphi = 0$ is set to align with the z-axis of the Cartesian coordinate system, and a is measured as distance along the x-axis.

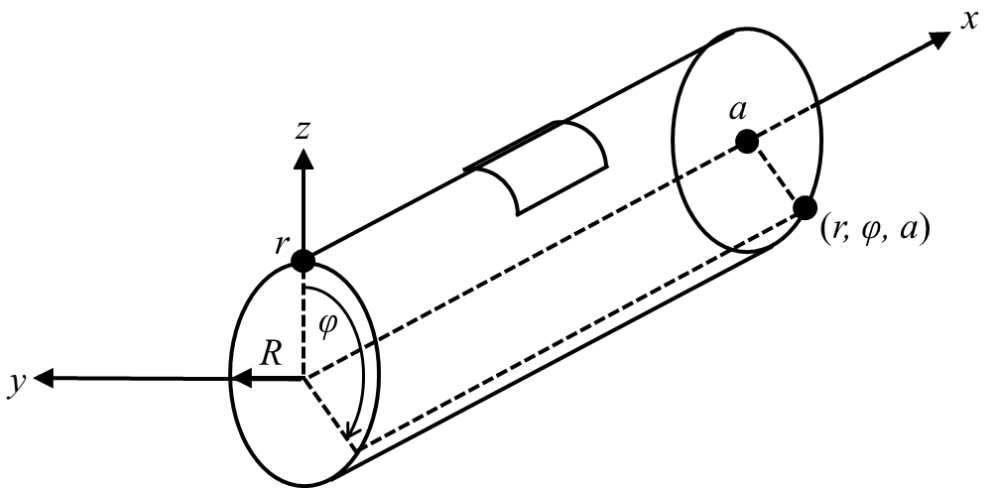

Figure 2.1: Cartesian (x,y,z) and Cylindrical (r,φ,a) coordinate systems were defined to allow for accurate placement of modeling elements and proper application of torque.

2.2 Torsion

A mechanics-level analysis of a rod in pure torsion was first conducted to evaluate the stresses and strains present in the test section shaft while torque was applied. Consider an element at point $P(r,\varphi,a)$ on the surface of a cylindrical shaft in pure torsion, as shown in Figure 2.2.

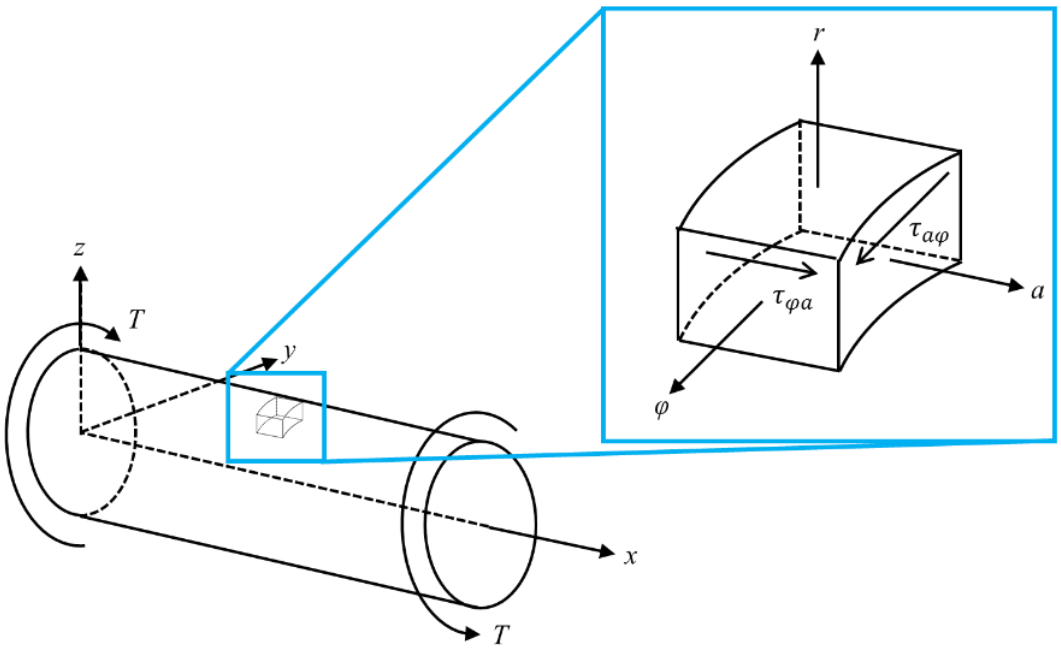

Figure 2.2: An element on the surface of a shaft in perfect torsion experiences no forces or stresses other than $\tau_{\varphi a}$ and $\tau_{a\varphi}$.

As an applied torque *T* is the only input acting on the shaft, it follows that the element at point *P* should experience no axial stresses or strains. Instead, this element experiences only shear stresses $\tau_{\varphi a}$ and $\tau_{a\varphi}$ as seen in Figure 2.2. Assuming that shear stress depends linearly on increasing radial distance from the *x*-axis, shear stress at any point can be expressed as a fraction of the maximum shear stress experienced on the surface of the shaft, as shown in Equation 2.1 [36].

$$\tau = \frac{r}{R}\tau_{max} \tag{2.1}$$

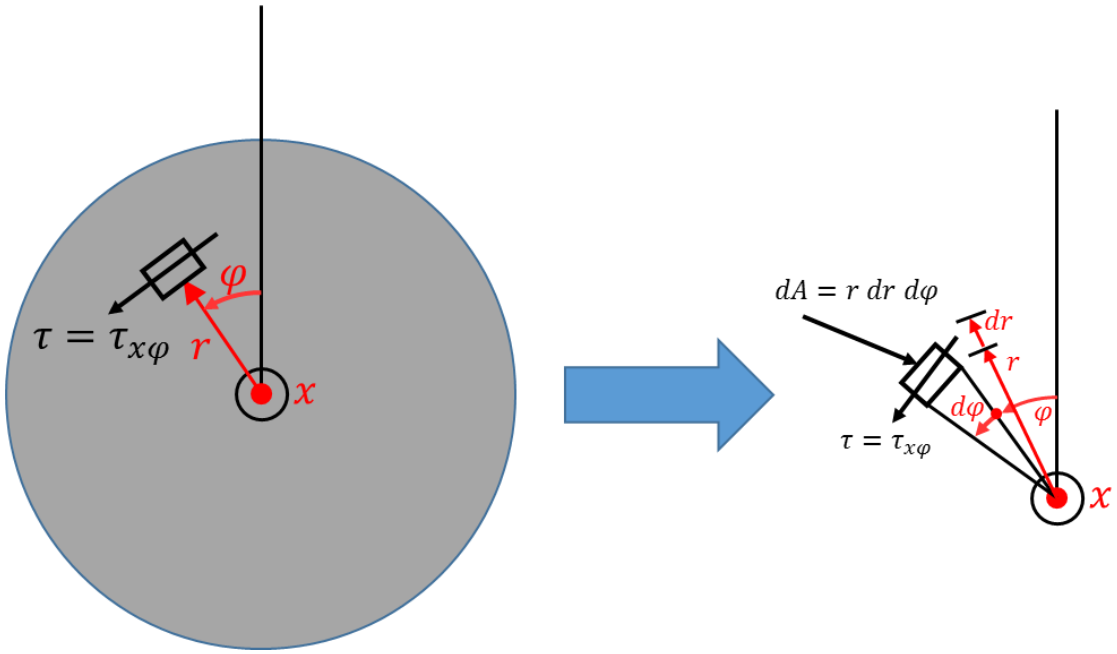

Figure 2.3: A cross-sectional element *dA* in torsion experiences stress along the *rφ*-plane in the direction of applied torque [36].

When a torque *T* acts at a cross section along the *x*-axis parallel to the *yz*-plane as seen in Figure 2.3, the shear stress $\tau = \tau_{a\varphi}$ acts on the cross section of an element, referred to here as *dA*, where the height of the area *dA* is *dr*, and the width of each area *dA* is *r dφ*. The torque produces both a force and moment on each element *dA*, with the force $dF = \tau\, dA$ and the moment $dM = dF\, r = \tau\, dA\, r$ about the *x*-axis. By integrating this elementary moment over the cross section, the internal torque of the cross section can be balanced and a term for maximum shear can be derived [36]:

$$T = \int_{Area} (shear\ stress \times elemental\ area) \times lever\ arm \tag{2.2}$$

$$T = \int_A (\tau\, dA)\, r = \int_A \frac{r}{R}\, \tau_{max}\, r\, dA = \frac{\tau_{max}}{R} \int_A r^2\, dA \tag{2.3}$$

$$T = \frac{\tau_{max}}{R}\int_A r^2(r\,dr\,d\varphi) = \frac{\tau_{max}}{R}\int_A r^3 dr\,d\varphi \tag{2.4}$$

$$T = \frac{\tau_{max}\,J}{R} \tag{2.5}$$

$$\tau_{max} = \frac{T\,R}{J}, \qquad \tau = \frac{r}{R}\tau_{max} = \frac{T\,r}{J} \tag{2.6}$$

Here, *J* represents the polar moment of inertia of a solid cylinder:

$$J = \int_A r^2 dA = \int_A r^3 dr\,d\varphi = \frac{\pi R^4}{2} \tag{2.7}$$

As shear stress is proportional to *r*, maximum shear stress $\tau = \tau_{max}$ occurs at the surface of the shaft, where $r = R$.

2.2.1 Mohr's Circle Analysis of a Solid Shaft in Torsion

The purposes of a Mohr's circle analysis are to determine the orientation of the "principal element," an elemental area on the surface of a shaft under applied torsional and axial loads defined such that no shear stress acts on the element, and to calculate the magnitude of principal stresses σ_1 and σ_2. In a general case where a shaft is exposed to axial and shear stresses, as shown in Figure 2.4, the axial stress at point *A* is $\sigma_A = \sigma_y$ and the shear stress at point *A* is $\tau_A = -\tau_1$, while the axial stress at point *B* is $\sigma_B = \sigma_x$ and the shear stress at point *B* is $\tau_B = +\tau_1$ [37].

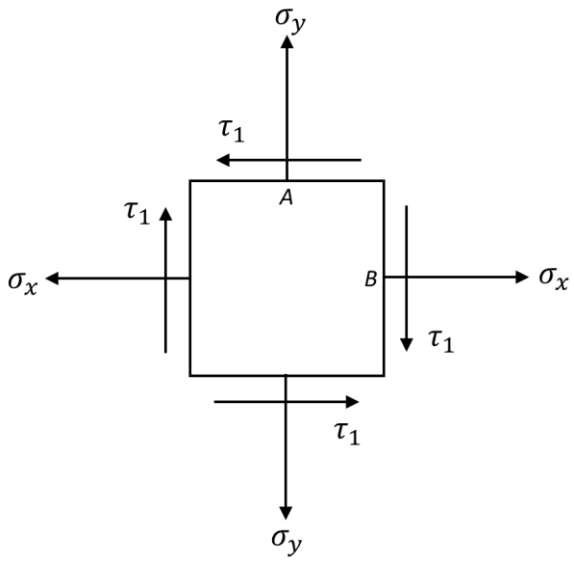

Figure 2.4: An element on the surface of a shaft under axial (tension) and torsional (anti-clockwise, or negative) loading is exposed to axial stresses σ_x and σ_y and shear stress τ_1 [37].

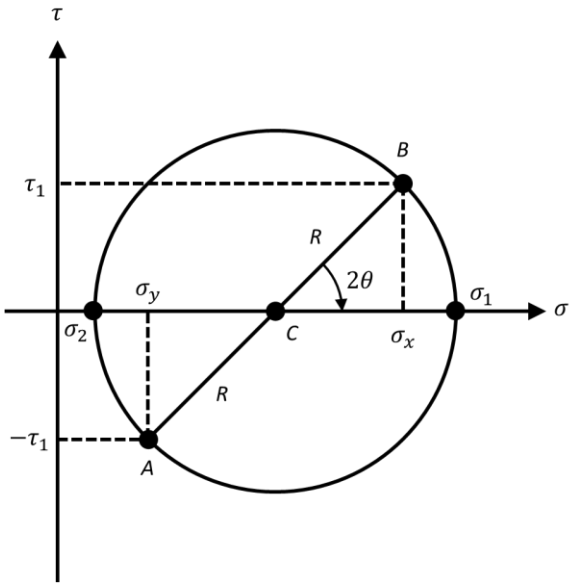

Figure 2.5: Points *A* and *B* are plotted along the τ-axis and σ-axis in the Mohr's Circle of an element on the surface of a shaft exposed to applied axial and shear stresses [37].

The Mohr's Circle for such an element is then defined by plotting stresses at points *A* and *B* along axes of shear stress τ and axial stress σ as shown in Figure 2.5. Here, a line is drawn between points *A* and *B* such that its center *C* is defined on the σ-axis as in Equation 2.8, the radius of the circle *R* extends between *C* and *A* or between *C* and *B* and is calculated using the Pythagorean theorem in Equation 2.9, principal stresses σ_1 and σ_2 are defined where the circle meets the σ-axis at a distance $\pm R$ from point *C*, and the angle between line *CA* or *CB* and the σ-axis is defined by convention as 2θ [37].

$$C = \frac{\sigma_x + \sigma_y}{2} \tag{2.8}$$

$$R^2 = (\sigma_x - C)^2 + \tau_1^2 \tag{2.9}$$

Here, solving for σ_1 and σ_2 in terms of σ_x, σ_y, and τ_1 provides principle stresses σ_1 and σ_2 as in Equations 2.10 – 2.11, while solving for θ in Equation 2.12 provides the clockwise angle used to rotate the original square element into the coordinate system of the principal axes [37].

$$\sigma_1 = C + R \tag{2.10}$$

$$\sigma_2 = C - R \tag{2.11}$$

$$\tan(2\theta) = \frac{\tau_1}{\sigma_x - C} \tag{2.12}$$

These equations simplify when considering points *A* and *B* along the edges of an element on the surface of a shaft in pure torsion as shown in Figure 2.6. At point *A* axial

stress $\sigma = 0$ and shear stress $\tau = \tau_{max}$ as calculated in Equation 2.6, and at point *B* axial stress $\sigma = 0$ and shear stress $\tau = -\tau_{max}$.

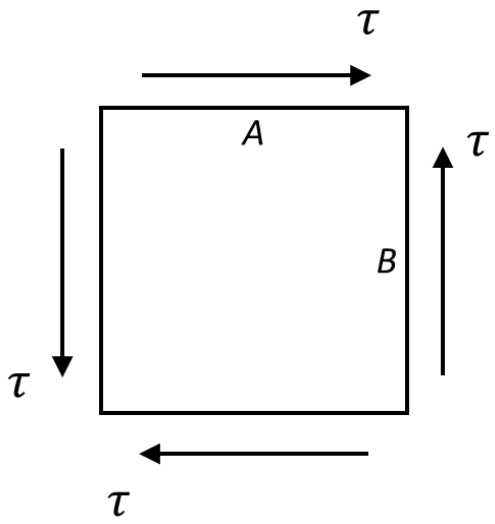

Figure 2.6: In pure clockwise torsion, the element experiences no axial stress.

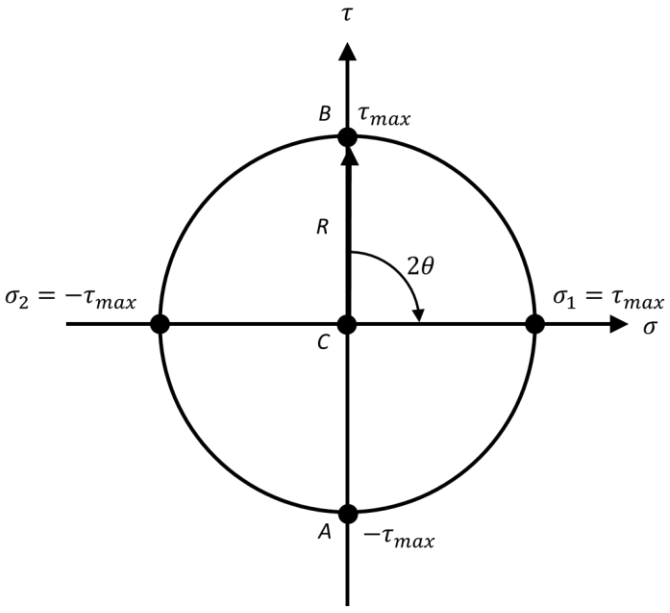

Figure 2.7: A Mohr's Circle representation of a solid rod in pure clockwise torsion depicts principal stresses $\sigma_1 = \tau_{max}$ in tension and $\sigma_2 = -\tau_{max}$ in compression and angle $\theta = 45°$ [36].

By inspection of the corresponding Mohr's Circle, points *A* and *B* are plotted directly on the τ-axis, such that principle stresses σ_1 and σ_2 and transformation angle θ are calculated as per Equations 2.13 – 2.17.

$$C = \frac{\sigma_x + \sigma_y}{2} = 0 \tag{2.13}$$

$$R^2 = (\sigma_x - C)^2 + \tau_{max}^2 \rightarrow R = \tau_{max} \tag{2.14}$$

$$\sigma_1 = C + R = \tau_{max} \tag{2.15}$$

$$\sigma_2 = C - R = -\tau_{max} \tag{2.16}$$

$$\tan(2\theta) = \frac{\tau_1}{\sigma_x - C} \rightarrow \theta = 45° \tag{2.17}$$

As such, it can be shown that principal stresses $\sigma_1 = \tau_{max}$ in tension and $\sigma_2 = -\tau_{max}$ in compression occur at $\theta = \pm 45°$ from the longitudinal *x*-axis, as depicted in Figure 2.7 [36], [37].

2.3 Magnetostriction Modeling Review

There are multiple phenomenological models that can be used to simulate and predict the response of magnetostrictive materials to applied field and stress, e.g. the data shown in Figures 1.4 and 1.5, respectively. Complex models are available that take into account hysteretic behaviors, operation at different frequencies of excitation, and non-linear behavior (e.g. responses at low fields and near magnetic saturation) by fitting experimental data to physically based laws [38]–[42]. However, most actuators and sensors

are designed to operate within the largely linear response regions in Figures 1.4 and 1.5 respectively. The linear constitutive model given by the piezo-magnetic equations, Equations 2.18 and 2.19, provides a useful representation of the three-dimensional magneto-elastic behavior in this linear operating region. These coupled linear equations relate changes in strain ε and magnetic induction B [T] in a magnetostrictive material to changes in applied stress σ [N/m^2] and applied magnetic field H [A/m, Oe].

$$\varepsilon = s^H \sigma + dH \tag{2.18}$$

$$B = d^* \sigma + \mu^\sigma H \tag{2.19}$$

The other terms in these equations are material-specific matrices that describe the elastic compliance in the presence of a constant applied magnetic field s^H [m^2/N], magnetic permeability in the presence of a constant stress μ^σ [H/m, Tm/A] and the two transduction coefficients, d and d^*, respectively, that describe the mechanical response to an applied magnetic field and the magnetic response to an applied mechanical stress. Here, d [m/A] is the matrix of magnetostrictive constants corresponding to the linear region of the ε-H curve, seen in Figure 1.4, and d^* [Tm^2/N] represents the change in magnetic induction due to a change in stress for a given constant magnetic field, seen in Figure 1.5. Superscripts indicate the property held constant in each case [2]. The resulting linearized coupled constitutive relations for a magnetostrictive actuator or sensor apply for constant temperature environments and low excitation inputs.

Equation 2.19 exhibits the coupled relationship between stress and field in the value of magnetic induction in a sample. It illustrates that for a given applied field H, magnetic

induction will vary as a function of stress in a manner that will be different than how magnet induction varies with stress for a larger or smaller applied field (e.g. the different biasing magnetic fields in Figure 1.5).

2.4 COMSOL Modeling

A COMSOL finite element model (Comsol Inc.) was implemented to evaluate the stresses, applied magnetic field, and magnetic flux lines present in a FeGa patch during a bi-directional quasi-static (BDQS) application of torque. The COMSOL model included the "Structural Mechanics" module to evaluate stresses present in an aluminum shaft and a perfectly bonded FeGa patch under bi-directional torsional loading, while the "AC/DC: Magnetic Fields, No Currents" module calculated applied magnetic field distribution and magnetic flux density across the patch and was used to visualize magnetic field lines travelling through the magnetic circuit. The physics from these two modules were not coupled; rather, stresses and principle strains were evaluated while a ±200 in-lb torque was applied to an aluminum shaft, while the magnitude and distribution of the applied magnetic field and magnetic flux density were evaluated separately. Results from this modeling effort were used with experimentally generated B-σ curves for FeGa to estimate an operating window for the proposed WiMET sensor.

2.4.1 Assumed Material Properties and Model Geometry

Assumptions made regarding the mechanical and magnetic properties of modelled materials are listed on Tables 2.1 – 2.2. Based on experimental results for a <100> oriented single crystal FeGa specimen tested at low applied stress and magnetic field, constant

values were assumed for elastic modulus, density, and Poisson's ratio within a region of linear stress-strain relations [26]. Relative permeability for FeGa was assigned based on material data provided by ETREMA Products Inc, while an estimate for Aluminum 2024 material properties was provided by Aerospace Specification Metals Inc [43], [44]. Physical properties for the flux piece, magnet, and Hall effect sensor are not included in Table 2.1, as they were not considered in the Structural Mechanics model. The model places the FeGa patch so that one edge is located at 12 inches from the fixed end of the shaft, and the other edge is located at 12.7 inches from the fixed end of the shaft.

Table 2.1: COMSOL model assumed material properties

Material	Elastic Modulus (GPa)	Density (kg/m^3)	Poisson's ratio	Relative Permeability	Residual Flux Density (G)
Aluminum 2024	73.1	2780	.33	1	0
FeGa	65	7800	.45	100	0
Flux Piece	-	-	-	1000	0
Hall Effect Sensor	-	-	-	1	0
Magnet	-	-	-	1.15	6800

Table 2.2: COMSOL model element geometry

Model Element	Length, *x* (in)	Width, *y* (in)	Thickness, *z* (in)	Radius (in)
Aluminum Shaft	24	-	-	0.5
FeGa Patch	0.7	0.7	0.025	0.5
Flux Piece	0.7	0.2	0.2	-
Magnet	-	-	0.08	0.12
Hall Effect Sensor	0.47	0.47	0.12	-

2.4.2 Torque Application

Torque is most fundamentally represented as the cross product of a force vector and position vector. As modelled in COMSOL, the magnitude of the position vector is the radius of the aluminum shaft, and the magnitude of the force vector is the quotient of the magnitudes of desired torque and position. The two vectors were modelled as orthogonal such that the cross product becomes a scalar.

$$T = r \times F \therefore F_{applied} = \frac{T_{desired}}{r_{shaft}} \tag{2.20}$$

A maximum torque of ±200 in-lb was tested such that a total force ±400 lb (four 100 lb force vectors applied along the length of the shaft) was applied in the ± φ across the entire surface of the shaft, at a radius of 0.5 in, in the ±φ direction. By convention here, positive torque is applied in the -φ direction, while negative torque is applied in the +φ direction.

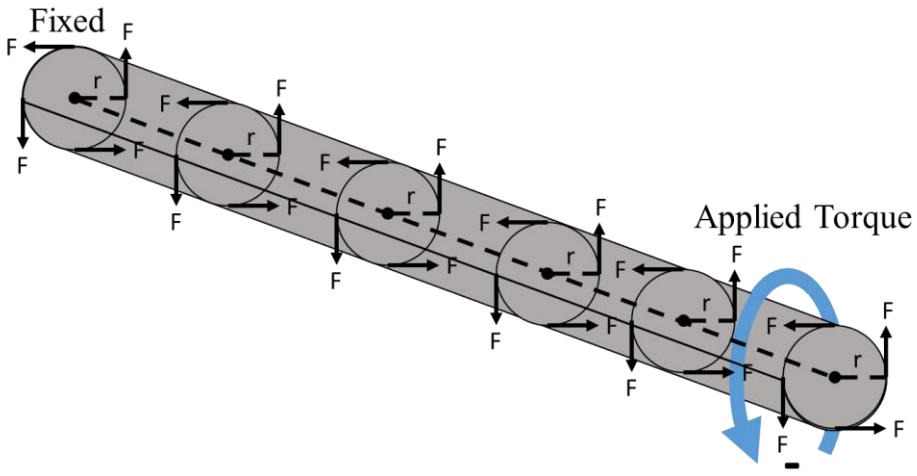

Figure 2.8: Torque was applied in the COMSOL model via the scheme shown in this figure along the length of the shaft.

2.4.3 Meshing

An "extra-fine" physics-controlled mesh was applied to ensure that model geometry for the flux piece, magnet, Hall effect sensor, and FeGa patch were rendered without imperfections due to improperly sized mesh elements, as seen on Table 2.3 and in Figure 2.9.

Table 2.3: COMSOL parameters for predefined "Extra-fine" mesh

Maximum element size (in)	Minimum element size (in)	Maximum element growth rate	Curvature factor	Resolution of narrow regions
0.84	0.036	1.35	0.3	0.85

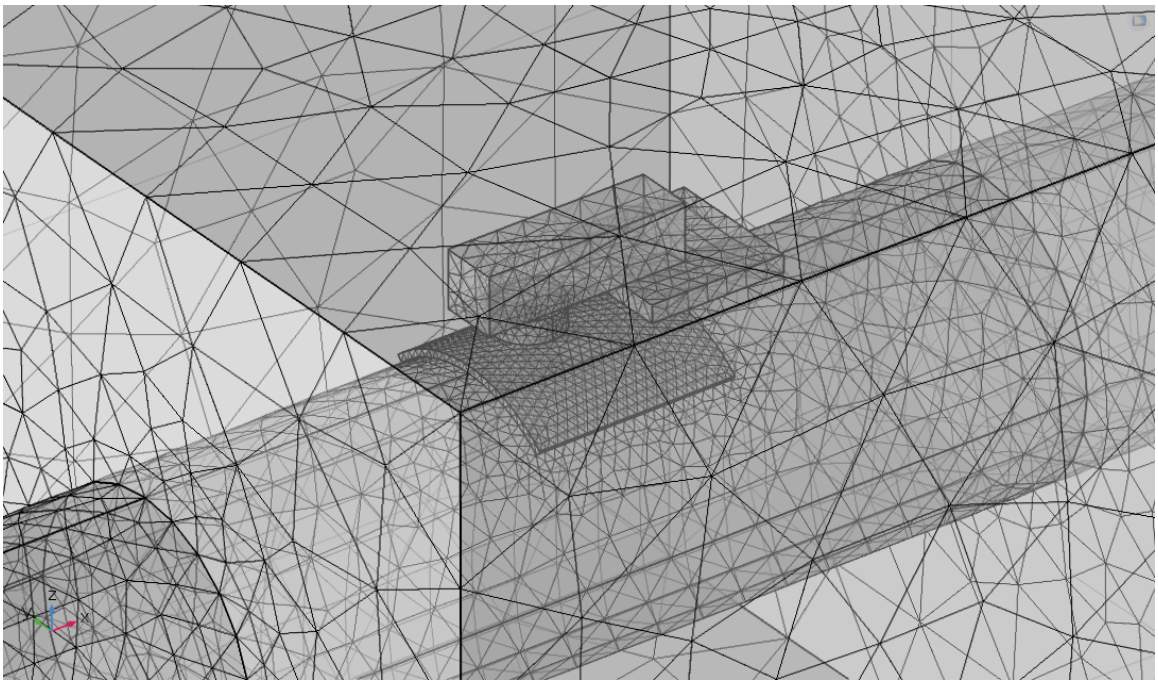

Figure 2.9: An extra-fine mesh was applied to the entire model to ensure accurate rendering of the magnet, flux piece, hall effect sensor, and FeGa patch.

2.4.4 Results

Under a +200 in-lb torque, the von Mises stress [N/m^2] is maximized at ~12.3MPa on the surface of the shaft near its fixed end, such that stress increases radially in the *r*-direction and decreases along the *x*-axis as seen in Figure 2.10. The FeGa patch experienced a ~5 MPa stress across its surface, compared to ~6 MPa on the surface of the shaft as seen in Figures 2.10 – 2.11, and a volume maximum principal stress of ~10 MPa occurred in the FeGa patch along an interface between the patch and the shaft along the edge of the patch, as seen in Figure 2.12. Torsional deflection is observed along the φ-axis, and it is scaled by a factor of 10 for visibility in Figure 2.11. These results is not consistent with the equations discussed in Section 2.2, where one would expect strain and stress to be constant along the length [36]. Because the shaft has polar symmetry, one would expect same stains and stresses to be induced regardless of the position along the surface of the shaft being analyzed.

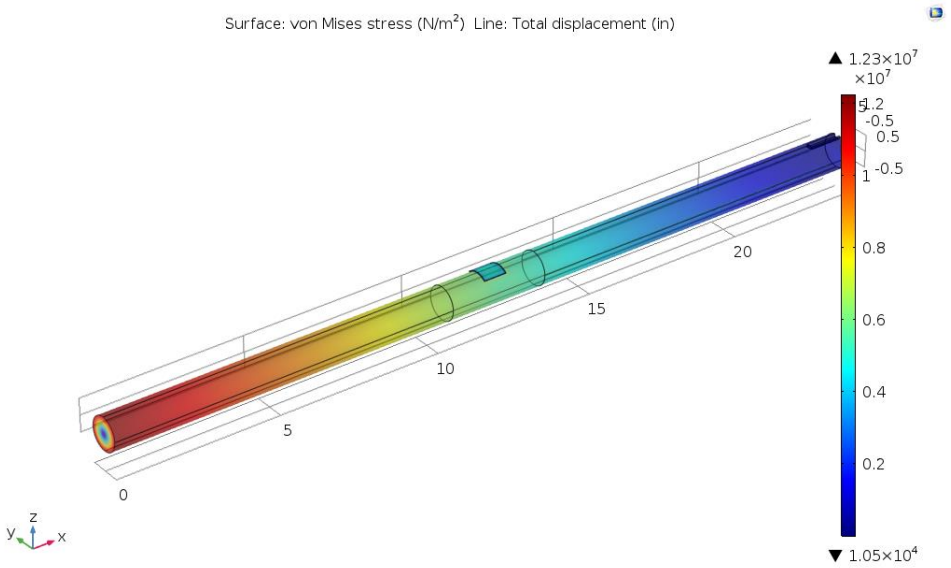

Figure 2.10: The maximum von Mises stress (N/m^2) occurred at the fixed end of the shaft and decreased along the *x*-axis under an applied torque of +200 in-lb.

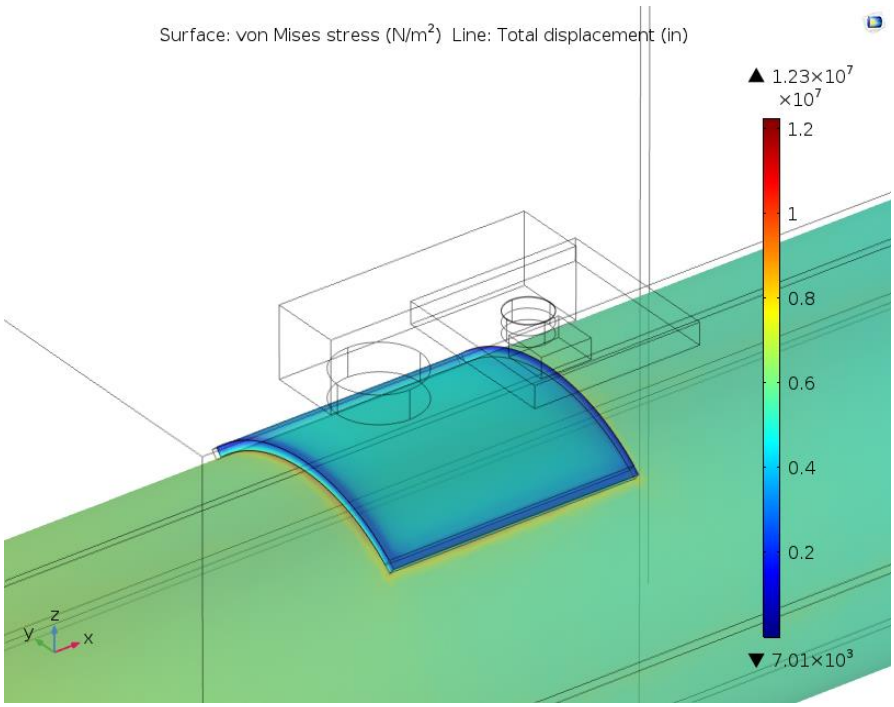

Figure 2.11: The FeGa patch experienced less surface stress than the underlying aluminum, and twisted due to application of +200 in-lb.

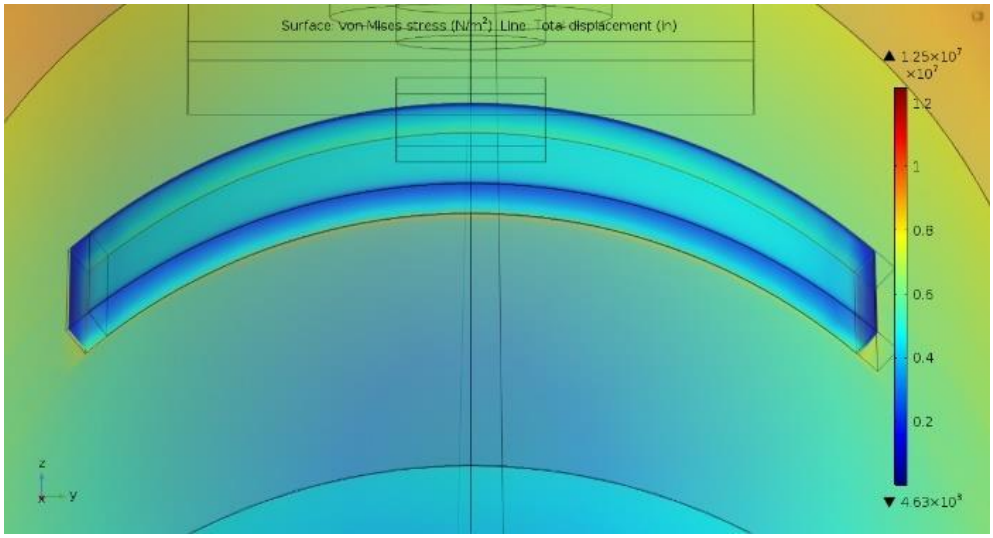

Figure 2.12: Viewed along the length of the shaft, the FeGa patch experiences ~5MPa across its surface, the underlying aluminum shaft experiences ~6MPa, and a volume maximum stress within the FeGa patch of ~10MPa can be observed along its edge.

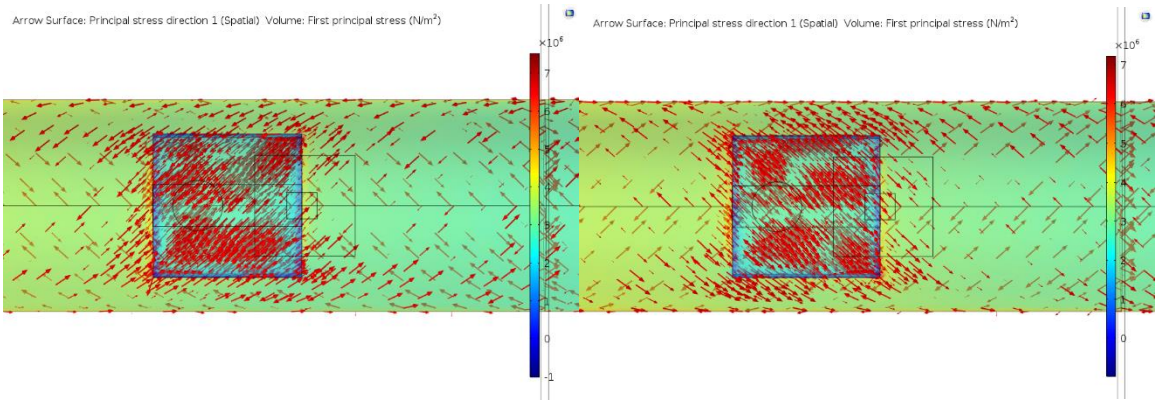

(a) (b)

Figure 2.13: Principal stress occurs at roughly ±45˚ from the *x*-axis as predicted under (a) +200 in-lb and (b) -200 in-lb of applied torque.

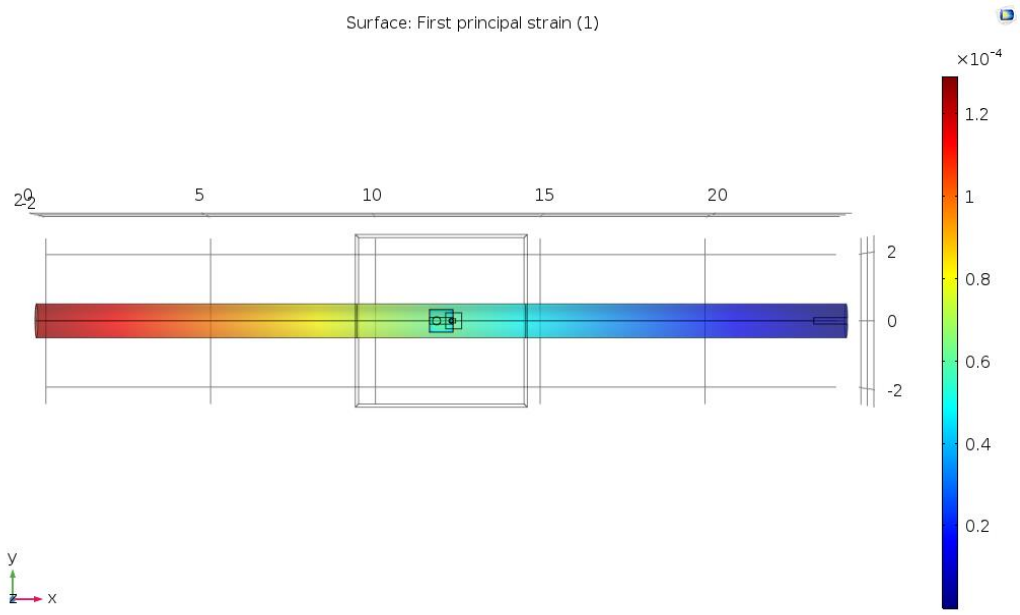

Figure 2.14: Principle strain was expected to vary by ~50 μstrain between the edges of the test section, which are approximately ±5 in from the center of the FeGa patch along the *x*-axis.

Note the stress and strain distributions in Figures 2.10 and 2.14 respectively represent a gradient in torque along the length of the shaft rather than a uniform torque along the length. Upon application of pure torsion in the clockwise and counter-clockwise directions, the principal stress vector occurred at ~ ±45˚ from the longitudinal *x*-axis, as predicted by the analysis in Section 2.1, and this can be seen in the COMSOL simulation results shown in Figure 2.13. The non-uniformity of the density of shear stress vectors and the slight differences in stress magnitude, indicated by different shades of green in this figure, are not understood. Principle strain, as seen in Figure 2.14, was expected to decrease along the length of the shaft as distance from the fixed end increased, such that two points, located ±5 in along the *x*-axis from the midpoint of the shaft at the ends of the notional test

section, experienced a strain of 88 μs and 36 μs respectively. This 52 μs decrease in strain along the length of the shaft was expected to affect the performance of magnetostrictive sensing elements depending on their placement along the test section.

An attempt was made to use the "AC/DC: Magnetic Fields, No Current" module to observe magnetic flux lines following the proposed magnetic circuit discussed in Section 1.4 under zero applied torque. However, the side view indicated flux diverted downward into the aluminum shaft rather than staying in the ferromagnetic patch and leaking from the edge of the patch into air and the aluminum shaft. Additionally, the analysis resulted in a directional asymmetry in the formation of flux density lines in the top down view, such that flux lines only rendered in the $+y$-direction relative to the longitudinal x-axis as seen in Figure 2.15 and this is also inconsistent with expected physics of symmetric systems. For this reason, it is suspected that there was an issue in trying to produce this result, and these figures do not seem correct.

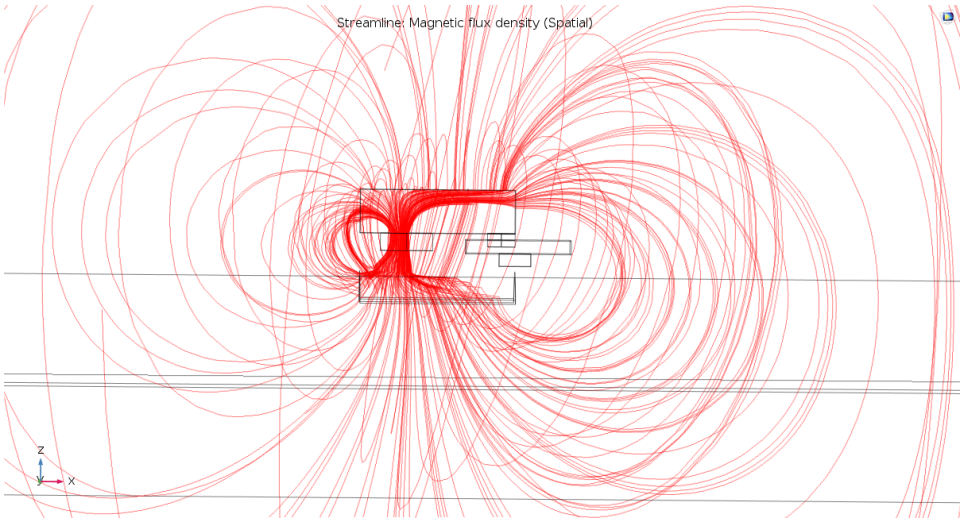

(a)

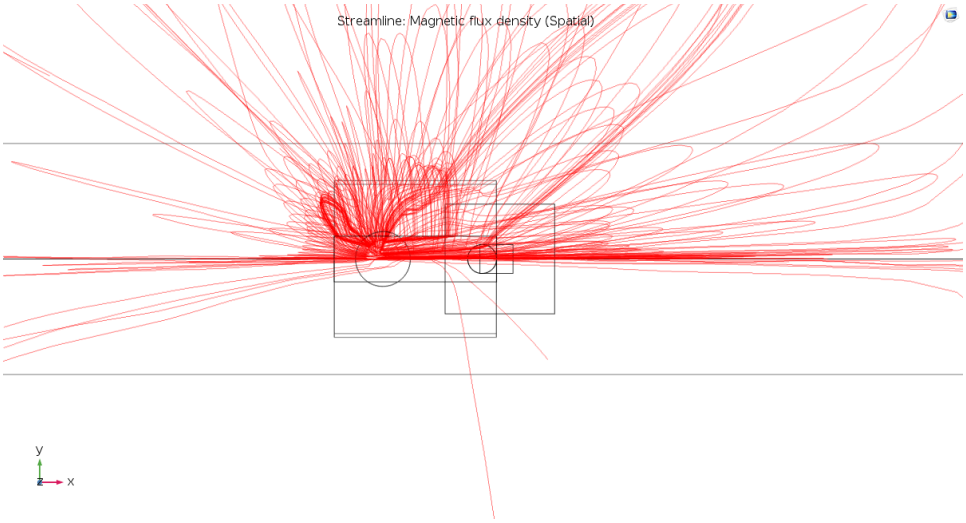

(b)

Figure 2.15: Magnetic flux lines in this COMSOL visualization rendered only on the +*y*-direction side of the *x*-axis.

When installed on the physical test setup, the Hall effect sensor was not in direct contact with the magnetostrictive patch, in order to avoid damage to either element during quasi-static and dynamic testing. Hall effect sensor output was expected to decrease with decreasing flux density as distance from the edge of the patch was increased. For instance,

at a standoff distance of 0.01 in between the patch and Hall effect sensor, the magnetic flux density measured on the bottom surface of the Hall effect sensor is only about half of that measured exiting the right edge of the FeGa patch, decreasing from ~60 mT to ~30 mT as seen in Figure 2.16. This ~50% decrease in measurable magnetic flux can be considered to compare the magnetic flux density exiting a magnetostrictive patch with the measurements made by a Hall effect sensor, assuming standoff distance remains at 0.01 in.

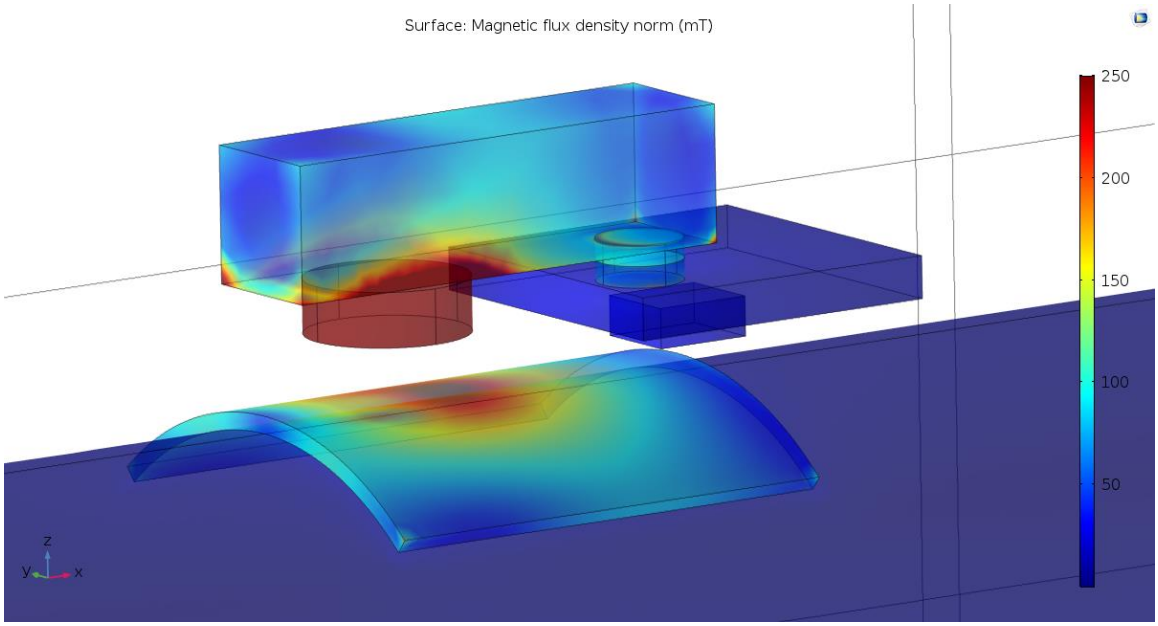

Figure 2.16: Magnetic flux density decreases by ~50% across a 0.01 in thick air gap between the FeGa patch and Hall effect sensor.

A model of the applied magnetic field in Figure 2.16 depicts flux leakage occurring primarily from the corners of the FeGa patch (as does Figure 2.17), and a maximum applied field of ~960 Oe is noted on the FeGa patch directly beneath the magnet, as seen in Figure 2.17 for a permanent magnet with a surface field of 3400 Oe at a distance of 0.05 in above

the patch. This amounts to a ~72% decrease in field strength between the bottom surface of the magnet and the bottom surface of the patch.

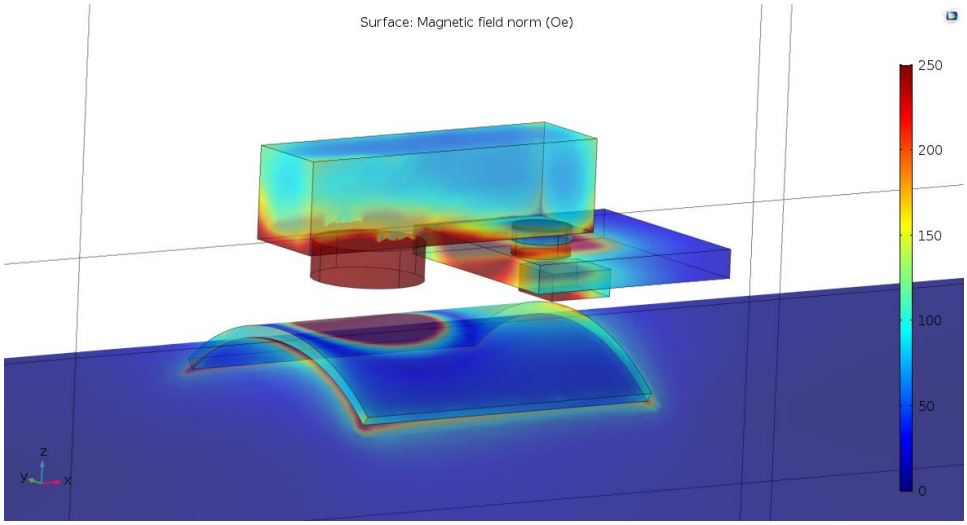

Figure 2.17: The FeGa patch is exposed to about 960 Oe directly beneath the magnet, and applied field strength decreases rapidly in all directions as distance from the magnet decreases.

Unlike Figure 2.15, where magnetic flux lines appeared asymmetric, Figure 2.16 and Figure 2.17 depict relatively symmetric distributions of applied of magnetic flux density and applied field respectively across the entire surface of the patch. As such, Figures 2.16 and 2.17 likely provide better estimates of the behavior of the three-dimensional magnetic field than the field line model in Figure 2.15.

2.5 Summary

Observed maximum principle stress τ in the FeGa patch was $\tau \sim 10$ MPa at an applied torque of ±200 in-lb and the observed applied magnetic field H across the surface of the FeGa patch was $H < 960$ Oe. By applying these values to experimentally generated B-σ curves for <100> oriented FeGa, an operating window for the sensor was approximated for loads less than 200 in-lb as seen in Figure 2.18.

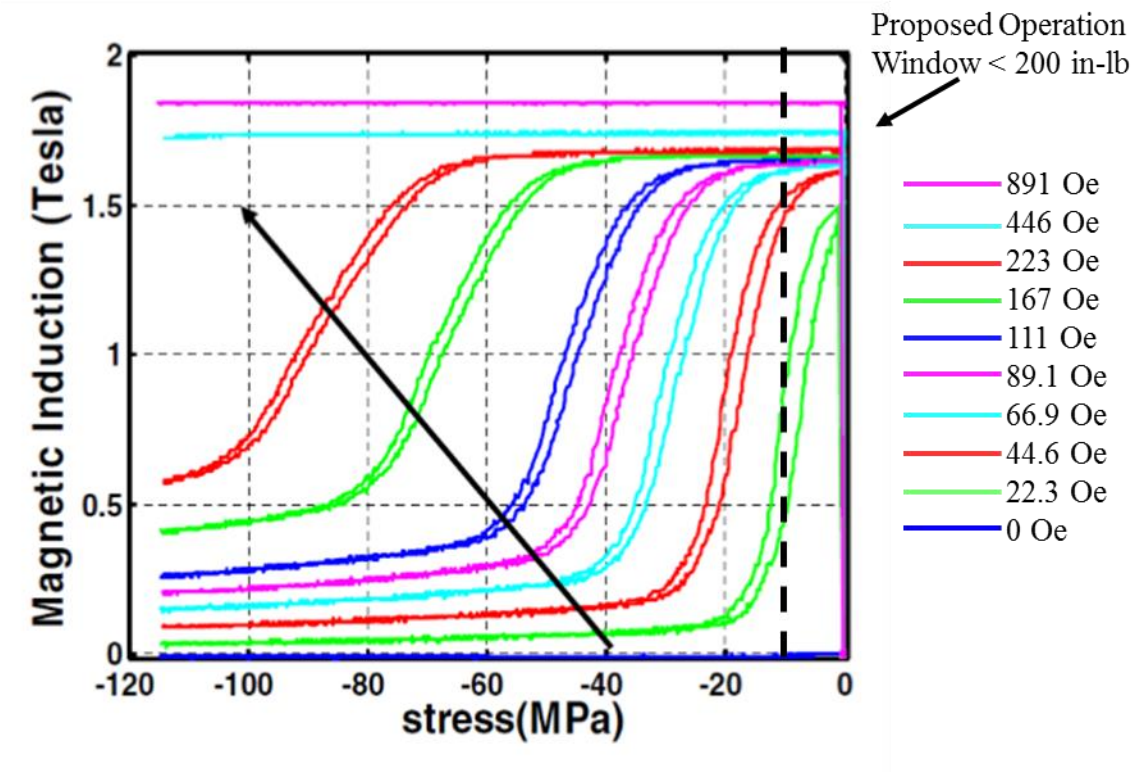

Figure 2.18: Assuming no torque greater than 200 in-lb is applied to the shaft, the WiMET sensor should operate along one of the curves to the right of the hatched line depending on magnet strength, magnet position, and Hall effect sensor position in the physical test setup.

Chapter 3: Experimental Setup

Chapter 3 describes the components of the WiMET sensor and details preparations made prior to bi-directional quasi-static (BDQS) testing and dynamic testing (Chapter 4). This chapter begins with a description of the magnetostrictive samples used over the course of testing and the relative position of each sample along the test section. The experimental benchtop test setup and individual WiMET components are then detailed, followed by a short discussion of the testing rationale and experimental results for a series of tests meant to increase output signal magnitude, which are summarized in Table 3.1. Finally, the operational limits of the benchtop test setup and additional considerations regarding quasi-static and dynamic testing are discussed.

Table 3.1: Preliminary test cases

Subject	Samples Tested
Sensor Positioning	FeGa Patch 1
Lateral Magnet Positioning	
Vertical Hall Effect Sensor Positioning	
Preliminary BDQS Testing	FeGa Patch 1 FeGa Patch 2 FeAl Ring 1, t = 0.1mm FeAl Ring 2, t = 0.4mm
Preliminary Testing	
Random Input Testing	
Bonding Method Investigation	Steel Shim

3.1 Material Samples

For preliminary quasi-static testing, two FeGa patches and two FeAl rings were adhered to the shaft. Each circumferential side of the FeGa patches was tested. Edges with a known circumferential crystal orientation of <100> were arbitrarily labeled edge (a) and

(b) as in Figure 3.1. The FeAl samples initially tested were two rings with respective thicknesses of 0.1 mm and 0.4 mm with a <100> circumferential crystal orientation. In total, the patches and rings provided six cases for preliminary testing: the (a) and (b) edge of each FeGa patch and one <100> edge of each the FeAl ring.

Additionally, the performances of an FeAl patch, a 0.15mm thick FeAl ring, and a FeGa paint sample were evaluated in later quasi-static and dynamic testing. The FeAl patch (of similar shape and dimension to the FeGa patch) was tested in order to compare the performance of FeGa and FeAl without the possibility of any interfering shape anisotropy effects, while the FeAl rings and FeGa paint were tested to evaluate any extreme shape effects in comparison to the patch samples. The FeGa paint was composed of <100> oriented FeGa flakes mixed with a toluene epoxy at a 1:1 ratio and was painted onto the shaft [45]. The composition, dimensions, and approximate distance from the fixed end of the shaft of each element are summarized in Table 3.2, while Figure 3.2 and Figure 3.3 illustrate the relative position of each sample with respect to the beginning of the test section, which is positioned ~3 in from the fixed end of the shaft, for quasi-static and dynamic testing respectively.

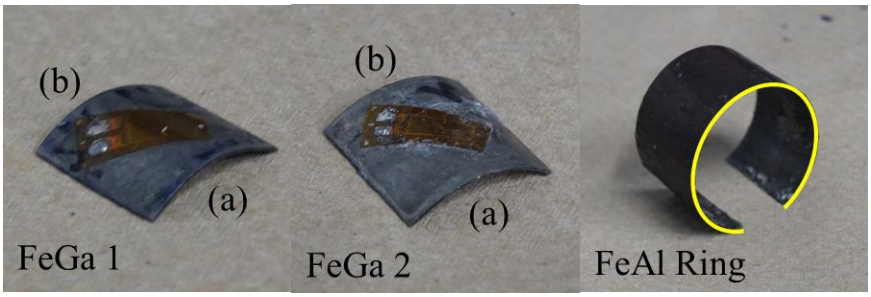

(a) (b) (c)

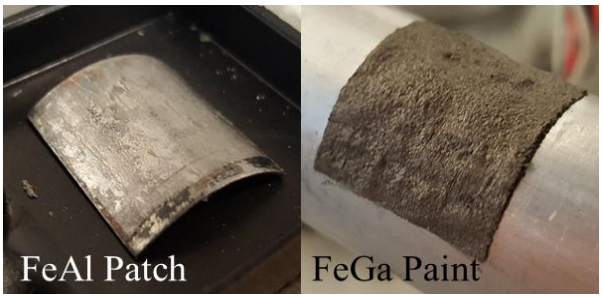

(d) (e)

Figure 3.1: Test samples included (a) & (b) two FeGa samples, (c) three FeAl rings with thicknesses of 0.1, 0.15, and 0.4 mm, and (d) one FeAl patch and (e) an FeGa paint sample.

Table 3.2: Magnetostrictive sensing elements used in BDQS and Dynamic testing

Sample	Composition	Dimensions (in)	Thickness	Distance from Shaft Fixed End to Closest Element Edge (in)	Distance from Shaft Fixed End to Furthest Element Edge (in)
FeGa Patch 1	$Fe_{81}Ga_{19}$	0.7 x 0.7	0.025 in	~4.5	~5.2
FeGa Patch 2	$Fe_{81}Ga_{19}$	0.7 x 0.7	0.025 in	~4.5	~5.2
FeAl Patch	$Fe_{80}Al_{20}$	0.7 x 0.7	0.02 in	~7.25	~7.95
FeAl Ring 1	$Fe_{80}Al_{20}$	~0.8 wide	0.1 mm	~7.25	~8.05
FeAl Ring 2	$Fe_{80}Al_{20}$	~0.8 wide	0.4 mm	~9.25	~10.05
FeAl Ring 3	$Fe_{80}Al_{20}$	~0.8 wide	0.15 mm	~9.25	~10.05
FeGa Paint	$Fe_{81}Ga_{19}$ 1:1, Flakes:Epoxy	0.8 x 0.8	.015 in	~11.25	~12.05

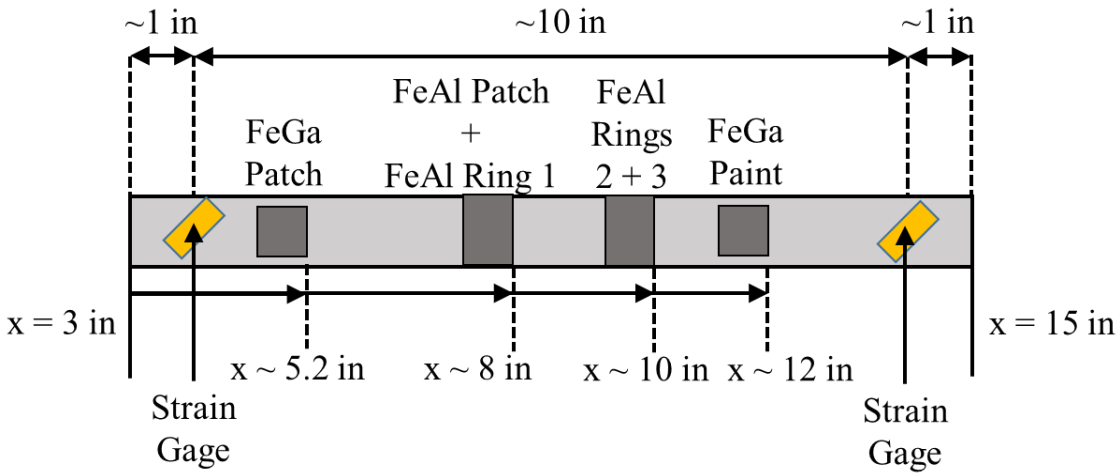

Figure 3.2: Magnetostrictive patches and rings were positioned along the 12 in long test section according to positions listed in Table 3.2 during quasi-static testing.

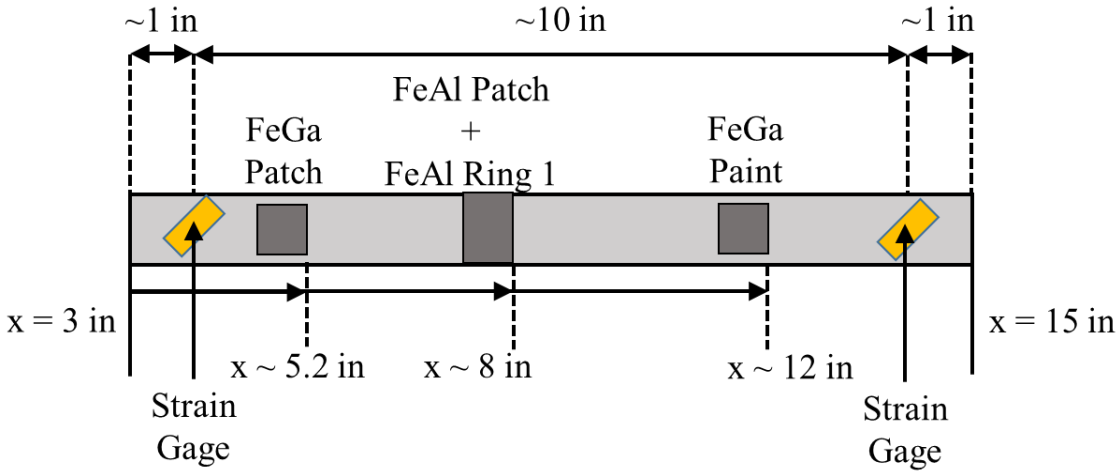

Figure 3.3: Magnetostrictive patches and rings were positioned along the 12 in long test section according to positions listed in Table 3.2 during dynamic testing.

3.2 Benchtop Test Setup

The benchtop test setup consisted of the WiMET sensor mounted to a height gage over the test section, a moment arm used to apply torque to the shaft, a commercial torque sensor, and a brake, as shown in Figure 3.4. The system specifications and operational limits of each component of the benchtop test setup are outlined in Table 3.3.

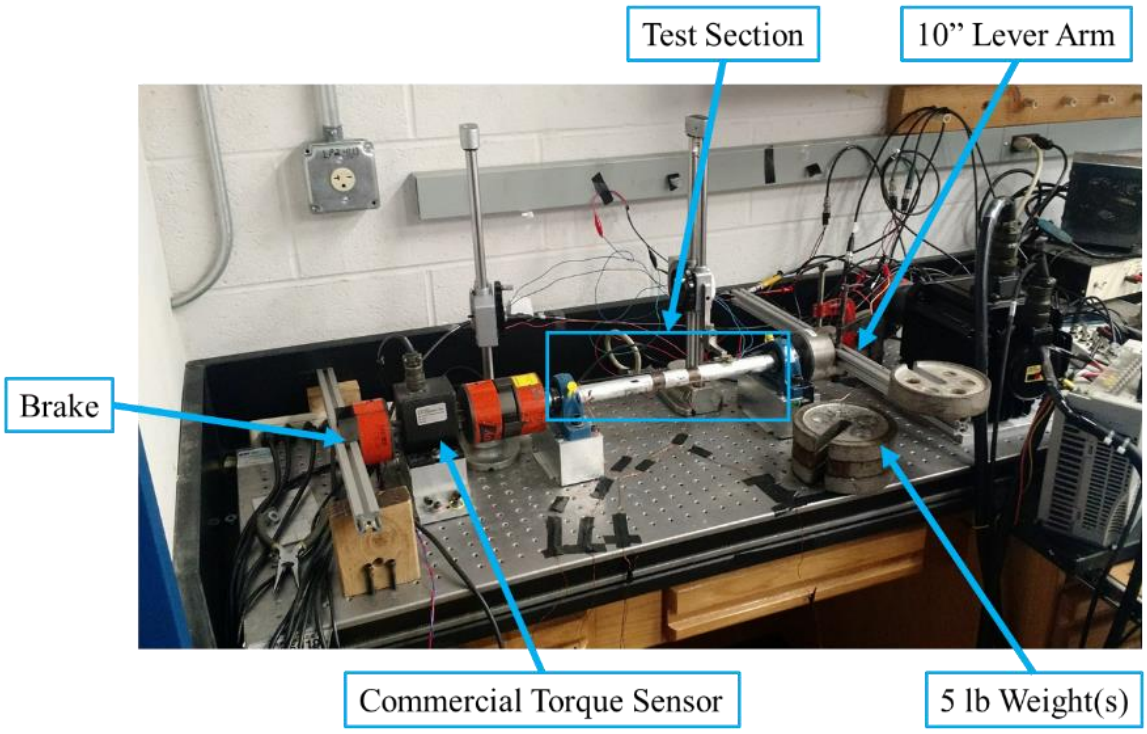

Figure 3.4: The BDQS benchtop test setup is composed of a lever arm for load application, a 1 in diameter 2 ft long aluminum shaft, a commercial torque sensor, a brake, and Lovejoy flexible couplings between each component.

Table 3.3: Quasi-static system specifications

Part	Specifications	Manufacturer	Details
Linear Torque Sensor	Max Torque: ~200 in-lbs	Sensor Developments Inc.	Rotary Shaft-Slip Ring
Shaft	Diameter: 1 in Length of test section: 12 in Length of shaft: 24 in	McMaster-Carr	Aluminum
Magnetic Flux Piece	Dimensions: 1.18 x 0.2 x 0.2 in	McMaster-Carr	Steel, High Permeability
Hall Effect Sensor	Sensitivity: 130 mV/mT @ 5V input voltage	Asahi Kasei Microdevices	Hybrid Linear Hall Effect Ics EQ-series
Bias Magnet	Residual flux density: 6800 G	McMaster-Carr	Nd-Fe-B disk

3.2.1 WiMET Sensor

The WiMET sensor and its components are pictured in Figure 3.5. A biasing magnet and an Asahi Kasei Microdevices Hybrid Linear Hall effect sensor (EQ-series) were mounted on a high permeability flux piece. Downselected from multiple magnets with surface fields between 100 and 300 mT, the biasing magnet was a low strength bonded-neodymium-iron-boron magnet with a surface field of ~135 mT and a residual flux density B_r of 6800 Gauss [G] (5902K52 from McMaster-Carr). The flux piece described in Table 3.3 was mounted to a height gage, which was used to precisely determine the offset distance between the Hall effect sensor and the magnetostrictive patch that was adhered to the shaft. Multiple magnetostrictive sensing elements were tested over the course of this study, including FeGa patches, FeAl patches, FeAl rings, and FeGa paint.

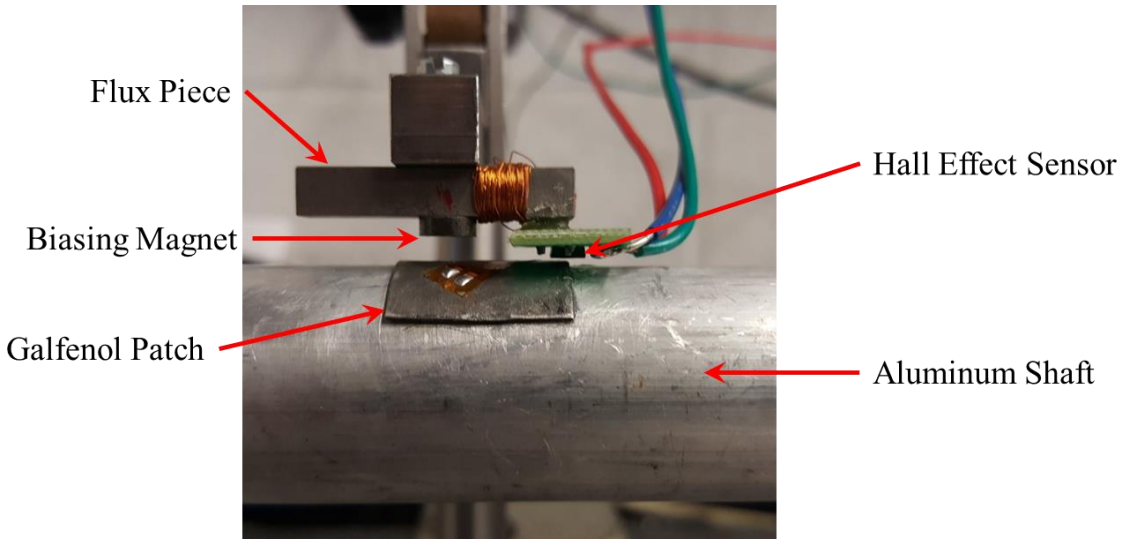

Figure 3.5: The WiMET sensor is presented in profile with its components identified.

3.2.2 Torque Application

Torque is typically represented as the cross product of two vectors: a position vector and a force vector. Here the two vectors are orthogonal, as force is applied tangentially to the radius of the shaft.

$$T = \vec{\boldsymbol{r}} \times \vec{\boldsymbol{F}} \rightarrow T = Moment\ Arm * Applied\ Load \tag{3.1}$$

In this case, position was measured in inches [in], force was measured in pound force [lb], and torque was measured by the commercial torque sensor in inch pounds [in-lb]. Torque application was achieved by placing 5 lb weights at ±10 in from the center of the shaft along a piece of 80-20, one inch square T-slotted aluminum (80-20 Inc.).

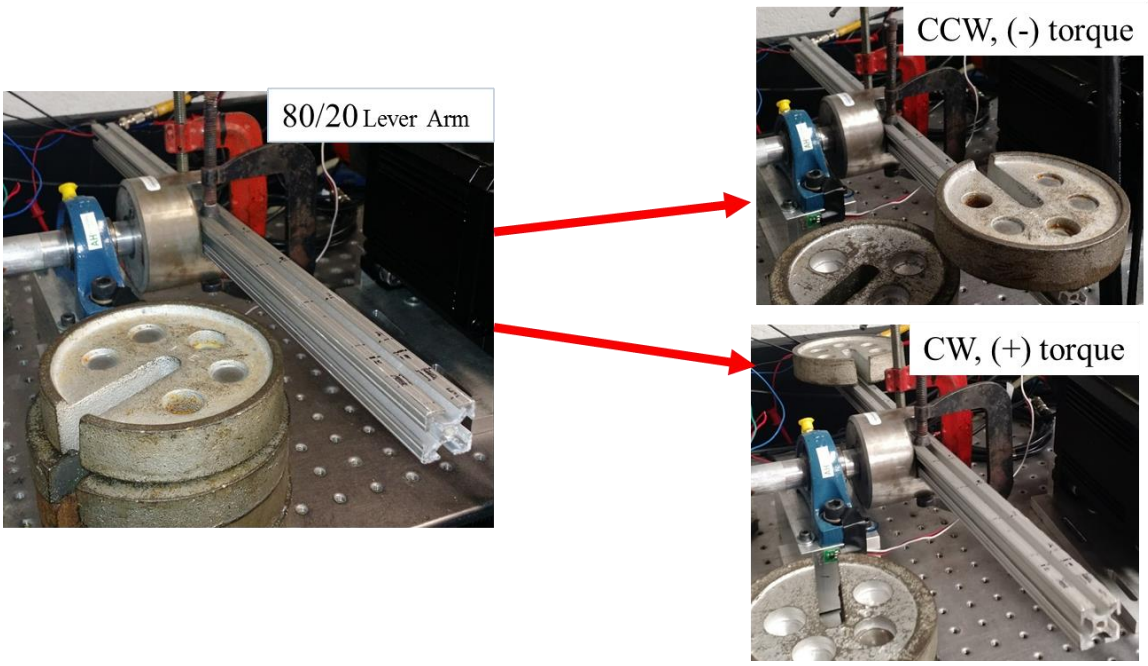

Figure 3.6: Torque was applied to the shaft by placing a number of 5 lb weights 10 in from the longitudinal axis of the shaft, with the pictured ± directional convention.

Torques of ±50, 100, 150, and 200 in-lb were applied to the shaft with the convention shown in Figure 3.6. As loading was performed by hand, an error of at most ± 5 in-lb associated with small variations in positioning of the weights was observed for any given load application. Torque measurements were confirmed by the commercial torque sensor mounted in-line with the shaft. A brake was assembled at the end of the shaft using wood blocks and 80-20 to keep the shaft stationary as loads were applied to the moment arm.

3.3 Sensor Positioning

This section details efforts made to maximize Hall effect sensor signal output by varying the position of the biasing magnet and decreasing the standoff distance between

the Hall effect sensor and magnetostrictive patch. Previous studies have shown that measurements should be made over the edge of a patch, where maximum flux leakage occurs as loads are applied [30]. Such flux leakage can be observed exiting the edges and corners of the modeled FeGa patch in Figures 2.16 – 2.17 from Section 2.4, and maximum flux leakage is observed at the corners of the patch. Both the height of the sensor above the patch and the lateral position of the magnet along the flux path were varied while the Hall effect sensor was fixed directly above the edge of the magnetostrictive patch.

3.3.1 Lateral Magnet Positioning

Here, the distance along the flux piece between the magnet and Hall effect sensor was varied. In each case, a 50 in-lb moment was applied and measured using the commercial torque sensor mounted in-line with the shaft, while the Hall effect sensor mounted above the edge of the FeGa patch recorded changes in voltage as loads were applied to and removed from the shaft. During these tests, the vertical distance between the Hall effect sensor and the FeGa patch was a constant 0.05 in.

Five configurations were tested, as depicted in Figure 3.7. Configurations (b), (c), and (d) were chosen in an effort to introduce magnetic flux to the edge of the patch opposite the side being measured by the Hall effect sensor, while (a) and (e) were selected as the extreme ends of the flux piece. Configuration (a) was expected to produce the lowest response, due to its distance from the patch and the Hall effect sensor. It was anticipated that configurations (b), (c), and (d) would create a magnetic circuit running from the magnet, across the air gap, into the edge of the patch, across the magnetostrictive material, and out the opposite edge across a second air gap into the Hall effect sensor, and ultimately

produce similar voltage outputs. The magnet in configuration (e) was predicted to over-saturate the output signal of the Hall effect sensor due to its proximity.

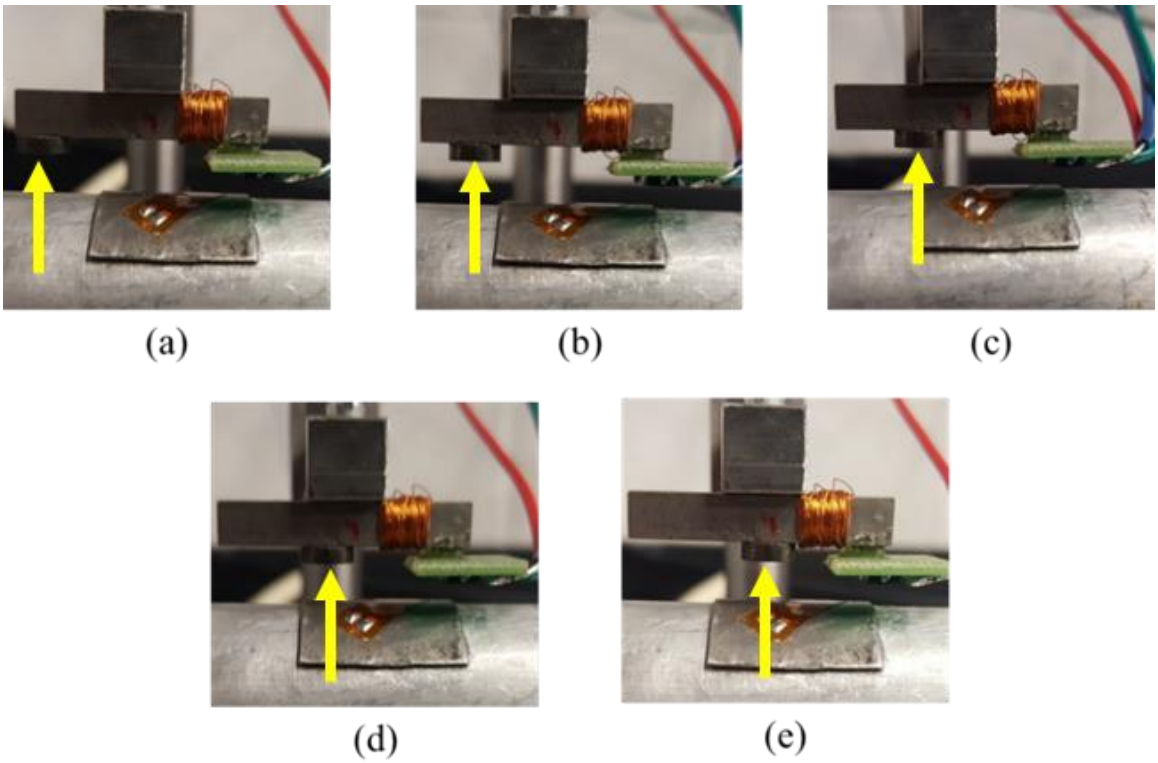

Figure 3.7: The bias magnet was positioned at (a) the far end of flux piece, (b) left of the left edge of the patch, (c) centered above the left edge of the patch, (d) right of the left edge of the patch, and (e) in the center of flux piece above the patch.

Table 3.4: Hall effect sensor voltage measured at five locations under a 50 in-lb applied torque

Case	Position (Qualitative)	Position (in)	Δ Signal (mV)
(a)	End of Flux Piece	0.63	0
(b)	Left of Edge	0.49	3
(c)	Over Edge	0.35	6
(d)	Right of Edge	0.2	8
(e)	Center of Flux Piece	0.17	10

The results of these five test cases are listed in Table 3.4, where "position" is a measure of the distance between the right edge of the magnet and the left edge of Hall effect sensor board. Case (e), pictured in Figure 3.8, did not oversaturate the Hall effect sensor. Rather, it resulted in the largest magnitude signal while the magnet was positioned over the patch, near the Hall effect sensor. Cases (b), (c), and (d) produced weaker signal as distance from the Hall effect sensor increases, while configuration (a) produced no noticeable variation in signal while load was applied.

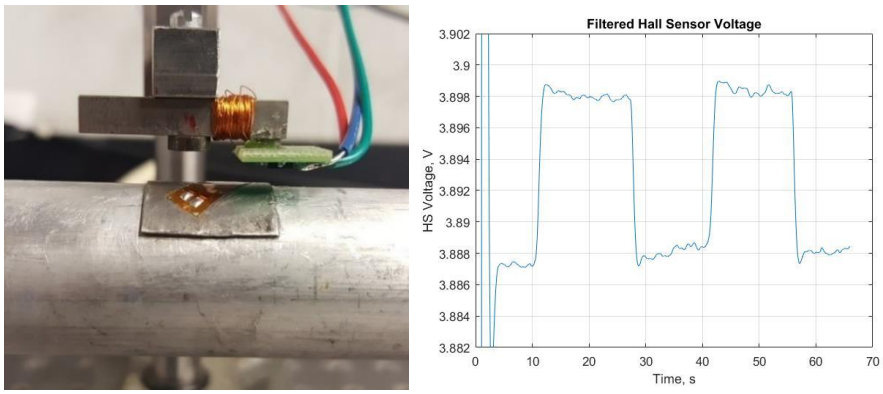

(a) (b)

Figure 3.8: In lateral position testing, the greatest signal was achieved with (a) the configuration above, presented in profile, with (b) a 10mV change in Hall effect sensor voltage output on application of a 50 in-lb torque.

Modeling results from Section 2.4 suggest that in all cases, the majority of flux leakage from the FeGa patch occurred from the corners and sides closest to the magnet. Even in position (e), when the magnet was furthest from the left edge of the patch, it is likely that this occurred. Testing with the magnet even closer to the Hall effect sensor was not done, although it is likely that the maximum change in Hall effect sensor output for a

given load would be reached with the bias magnet positioned somewhere between position (e) and having the magnet in contact with the Hall effect sensor. As such, it appears that the Hall effect sensor measured greater magnetic induction as the magnet was moved from left to right along the flux piece, but the sensor did not become over-saturated by excessive flux leakage, as most flux lines simply exited the leftmost corners of the patch.

3.3.2 Vertical Hall Effect Sensor Positioning

Here, the vertical distance between the edge of the FeGa patch and Hall effect sensor was varied. In each following case, a 50 in-lb torque was applied to the shaft and was measured using the commercial torque sensor. Additionally, the Hall effect sensor mounted above the edge of the FeGa patch recorded changes in voltage as loads were applied to and removed from the shaft. Three cases were tested with offset distances of (a) 0.05 in, (b) 0.025 in, and (c) 0.01 in, as shown in Figure 3.9.

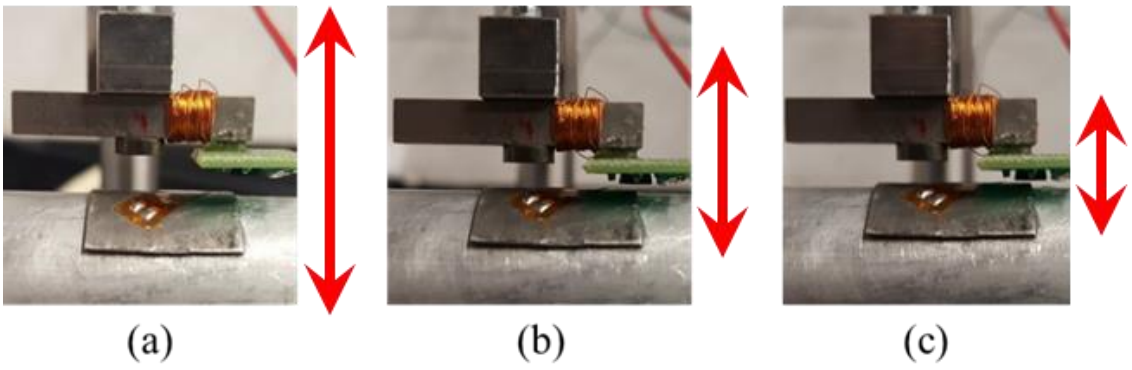

Figure 3.9: Hall effect sensor was mounted above the magnetostrictive patch at a height of (a) 0.05 in (b) 0.025 in (c) 0.01 in (arrows indicate trends, as actual air gaps are just barely discernable in this image).

Table 3.5 shows the resulting signal from the Hall effect sensor upon application of a 50 in-lb torque at each standoff distance between sensor and patch. As the Hall effect sensor approached the magnetostrictive patch, the output of the sensor increased due to an increased magnetic flux density closer to the edge of the patch, as suggested in Section 2.4.

Table 3.5: Hall effect sensor signal output at varied distances between patch and sensor

Case	Height (in)	Signal (mV)
(a)	0.05	10
(b)	0.025	19
(c)	0.01	27

3.3.3 Final Sensor Configuration

The configuration for the WiMET sensor reported in this thesis utilized the preceding best-cases from Sections 3.3.1 and 3.3.2. The center of the Hall effect sensor was mounted directly over the right edge of the patch, the magnet was positioned over the magnetostrictive material on the center of the flux piece along the *x*-axis, and the Hall effect sensor was positioned 0.01 in above the edge of the magnetostrictive material. This configuration, depicted in Figure 3.10, quantitatively provided the best signal-to-noise ratio.

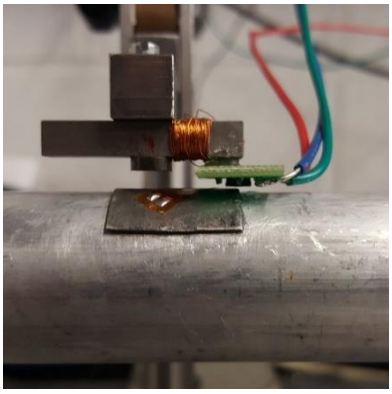

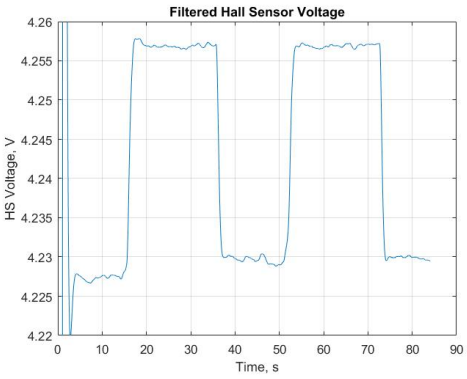

(a) (b)

Figure 3.10: Maximum sensor response was achieved in (a) the above configuration, with (b) a Hall effect sensor output voltage of ~30mV on application of 50 in-lb.

3.4 Preliminary Bi-Directional Quasi-Static (BDQS) Testing

Appendix C provides an in-depth discussion of the testing procedure, data analysis, and results of tests conducted to evaluate the signal response of the WiMET sensor under BDQS torsional loading. As summarized in Table 3.6, this study assessed the signal magnitude and linearity of response over a range of applied torques, recorded measurement error between tests of the same torque input, and characterized signal drift between the beginning and end of torque application.

Table 3.6: Sensitivity of magnetostrictive sensing elements based on preliminary testing

Sample	Sample Dimensions (in)	Sensitivity (mV/in-lb)		Signal Drift (% Mean)	
		-	+	-	+
FeGa Patch 1 Edge (a)	0.7 x 0.7	0.36	0.175	1.6	1.5
FeGa Patch 1 Edge (b)	0.7 x 0.7	0.36	0.23	0.9	0.6
FeGa Patch 2 Edge (a)	0.7 x 0.7	0.15	0.18	3.7	0.8
FeGa Patch 2 Edge (b)	0.7 x 0.7	0.16	0.27	4.2	1.9
FeAl Ring, t = 0.1mm	0.75 x 3.14	0.28	0.33	0.4	0.5
FeAl Ring, t = 0.4mm	0.75 x 3.14	0.33	0.33	0.4	1.5

Sensitivity in Table 3.6 was calculated as the observed increase in Hall effect sensor output as a range of torques (50 – 200 in-lb) was applied to the shaft. FeGa samples offered a wide range of sensitivities between 0.15 – 0.36 mV/in-lb depending on the direction of load application and depending on the sample, while signal drift over a ten second load application maximized at 15% of mean signal in a single case. FeAl ring samples provided a smaller range of sensitivities between 0.28 – 0.33 mV/in-lb, offering good bi-directional agreement across samples tested and comparatively low signal drift on the order of 1% of mean signal. Based on feedback from collaborators at ARL, it was suggested that non-uniformity in response among the FeGa samples was most likely due to the formation of a non-uniform adhesive layer between the shaft and patch during sample application, and as such the adhesive application process was updated before further testing was conducted.

3.5 Bonding Method Investigation

Following a presentation of the results of preliminary BDQS testing in Section 3.4 and Appendix C to collaborators at the Army Research Lab at Aberdeen Proving Grounds, it was suggested that drift and inconsistencies in signal response could be due in part to a non-uniform bond layer between the shaft and magnetostrictive patches. Our collaborators also suggested that improved bonding methods could result in a greater signal-to-noise ratio in sensor output. Therefore, an effort was undertaken to improve and standardize adhesive application methods to ensure the presence of uniform bond layers for future testing. Adhesive selection, test procedure, test variables, and results are presented in this section.

3.5.1 Initial Adhesive Selection

Very early in the design of this test setup, the performances of multiple adhesives were quantitatively evaluated. Multiple pieces of steel shim were adhered to an aluminum sheet, and strain on each piece of shim was measured as a bending load was applied across the tip of the sheet as seen in Figure 3.11. The strain response was averaged over several runs and is plotted in Figure 3.12.

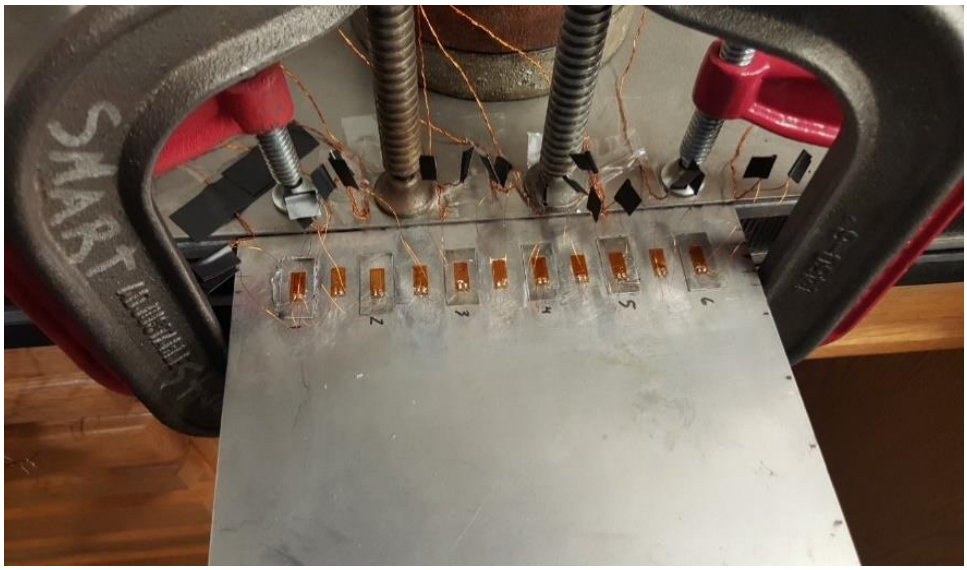

Figure 3.11: Strain gages were mounted on and between similar samples of steel with different underlying adhesives to provide strain reading along the length of a sheet of aluminum as tip loads were applied.

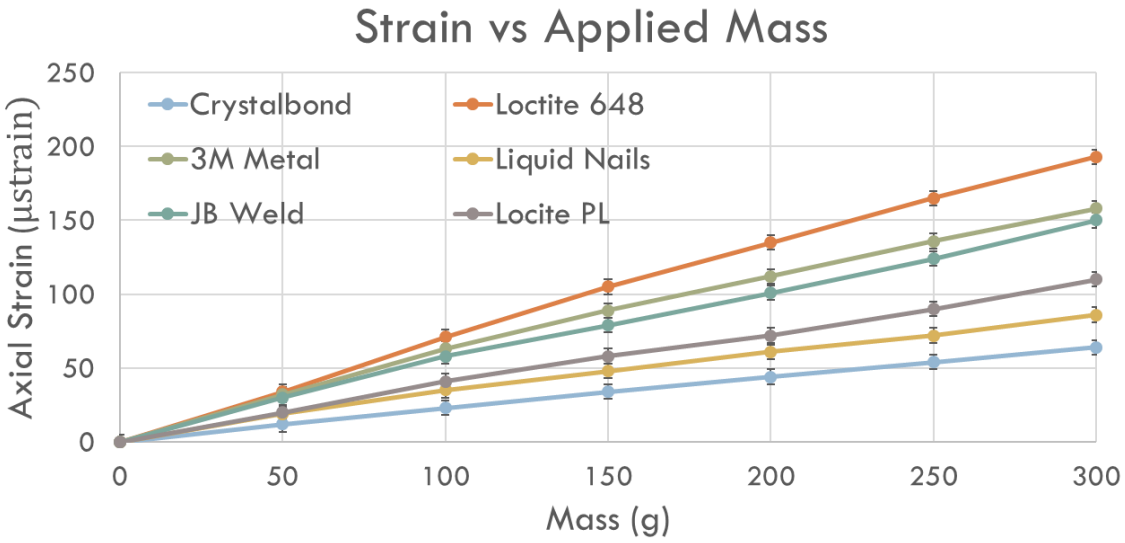

Figure 3.12: Initial bending tests on a thin aluminum sheet demonstrated the superior performance of Loctite 648.

Loctite 648 provided the highest axial strain under bending in every case. Loctite 648 is a urethane methacrylate acrylic adhesive that cures in the absence of oxygen, and it is specifically designed for use with close fitting parts, preventing loosening and leakage from shock and vibration [46]. As such, Loctite 648 was used to adhere magnetostrictive sensing elements to the shaft for all other testing presented in this document.

3.5.2 Testing Procedure

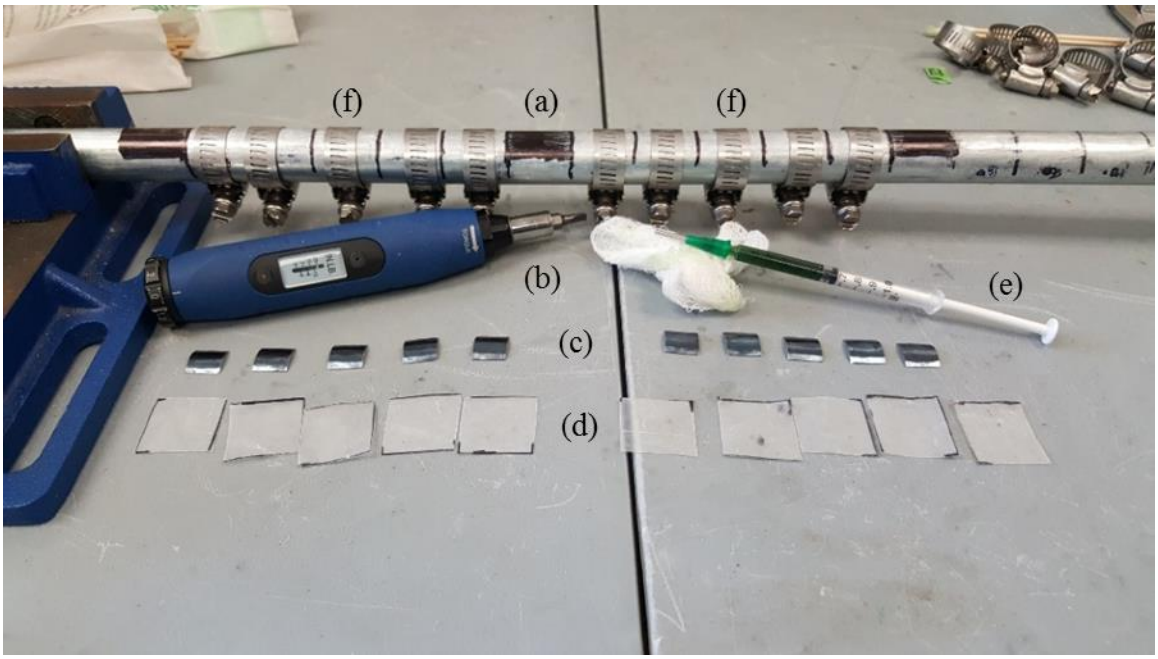

Figure 3.13: The test setup for the adhesive bonding method study was comprised of the above (a) steel shaft, (b) torque wrench, (c) steel shim, (d) wax paper, (e) syringe containing Loctite 648 adhesive, and (f) hose clamps.

The following procedure was carried out for each sample. In order to avoid any unnecessary wear on the magnetostrictive patches, steel shim was used in its place. The shim was bent by hand to ensure adequate fit to the steel shaft and measured roughly 0.01

in thick and 0.5 in per side. The surfaces of the shaft and each piece of shim were cleaned, first by acetone to remove any remaining adhesive from previous tests and then by ethyl alcohol to degrease the surface. Each shaft test section and the bonding surface of each shim piece were then roughened with sandpaper to increase the surface area where bonds were able to form by swiping along the circumference and the length of the shim ten times each. After roughening, the surface was wiped clean with gauze, adhesive volume was measured in a syringe, and adhesive was applied in several different configurations on the surface of the patch as shown in Figure 3.14.

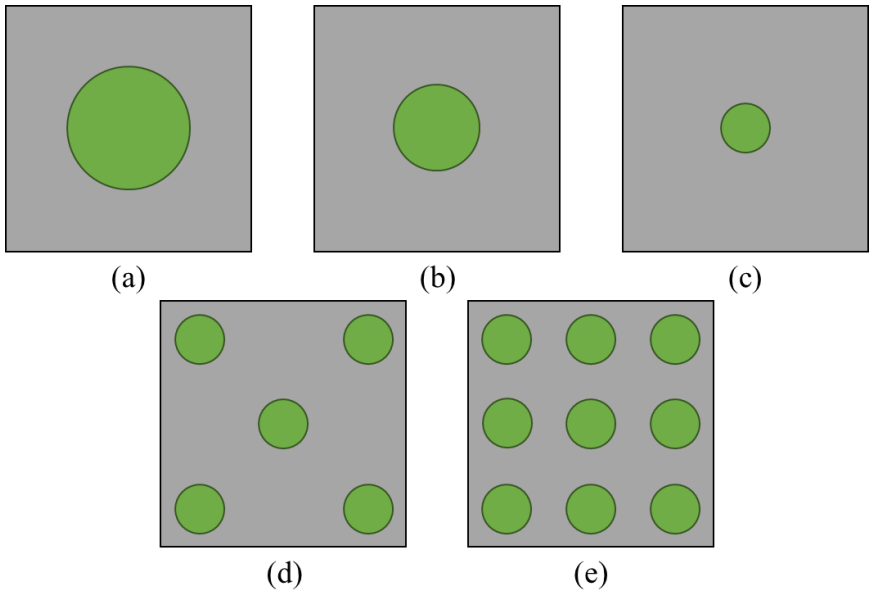

Figure 3.14: Adhesive application configurations included a) a single 0.05 mL droplet, b) a single 0.03 mL droplet, c) a single 0.01 mL droplet, d) five 0.01 mL droplets, and e) nine 0.01 mL droplets.

Hose clamps were tightened by a torque wrench with specific input torques to secure the shim tightly during its two-hour cure time. Wax paper was wrapped around the circumference of the shaft between the shim and the clamps to ensure the hose clamps would remain free of adhesive. After the two-hour cure time, the shim was removed from the shaft using a precision razor blade and prepared for imaging. The bond layer remained almost entirely on the shim after removal.

Each piece of shim and its underlying test section were imaged with a camera, and qualitatively examined. The total thickness of the shim considering the steel and adhesive was measured in eight locations along its perimeter with a pair of calipers on the edges that ran along the circumference of the shaft. After cleaning, the thickness of the shim was measured at each point and subtracted from the total measurement to determine the thickness of the adhesive layer at each point. The maximum thickness and minimum thickness were noted in each case, and the eight data points were averaged. Finally, each piece of shim was vigorously wiped with an acetone-covered cotton-tipped applicator, and the adhesive was scraped off using the blunt wooden end of the applicator. This process was repeated over several sets of parametric variations.

3.5.3 Independent Variables

Over the course of six total rounds of testing, sandpaper grits 60 and 320 were used to roughen the shim and the test section, each hose clamp was tightened to 5, 10, and 15 in-lb, and different volumes of adhesive were applied to each sample before they were allowed to cure for at least two hours. The variation of these parameters on a test-by-test

basis is summarized in Table 3.7. Adhesive was applied in five different configurations for each round of testing, as shown in Figure 3.14.

Table 3.7: Adhesive bonding method test variables

Test Round	Sandpaper Grit	Torque
1	60	15
2	320	15
3	60	5
4	60	10
5	320	5
6	320	10

3.5.4 Results

In most cases, torque applications of 5 in-lb and 10-lb resulted in the formation of largely non-uniform bond layers with maximum thicknesses greater than those observed in cases with a 15 in-lb torque application during curing. The results of research characterizing in-plane shear loaded adhesive layers suggest that a decrease in adhesive strength should be expected as bond thickness increases, due to the low yield strength of comparatively thick adhesives [47]. As such, bond thickness should be minimized where possible, while still ensuring even sample coverage. The study also suggested that thin bonds (< 0.10 in) are more likely to fail as a result of poor connection to substrate. This highlights the importance of vigorous and uniform sanding across both surfaces to ensure adequate surface area for the bond to take hold [47]. According to the material data sheet for this brand of Loctite when comparing the bond strength and cure speed of 0.05 mm, 0.15 mm, 0.25 mm thick bond layers, the thinnest of the three, yielded the quickest and strongest bond on a steel shaft [46].

Test 1 configuration (d) in Figure 3.14 yielded the most effective solution, as shown in Figure 3.15. Here, 60 grit sandpaper was used to roughen both surfaces, adhesive was applied as five 0.01mL dots, and a torque wrench applied 15 in-lb to the tightened hose clamps over the two-hour cure time. As it was pressed onto the shaft, adhesive was observed to spread evenly around the edges of the shim. Upon removal of the patch, the bond layer was measured to be 0.05 mm thick, with an error of 0.01 mm.

Figure 3.15: This image shows the steel shim after debonding to examine bond layer thickness. A uniform bond layer formed around the edges of the shim when sanded with 60 grit sandpaper, using a 15 in-lb applied torque with 0.05 mL of Loctite 648 applied evenly to the bottom surface of the shim.

When applying the magnetostrictive patches to the main test shaft, the amount of adhesive used was scaled to account for the increased dimensions of the magnetostrictive sample, as seen below in Equation 3.2 and in Table 3.8.

$$\left(\frac{Volume_{adhesive}}{Area_{sample}}\right)_{shim} = \left(\frac{Volume_{adhesive}}{Area_{sample}}\right)_{FeGa,FeAl} \quad (3.2)$$

Table 3.8: Adhesive volume used for different samples

Property	Steel Shim	FeGa	FeAl patch	FeAl ring
Sample Dimensions (in)	0.5 x 0.5	0.7 x 0.7	0.75 x 0.75	0.8 x 3.14 circumference
Bonding Surface Area (in^2)	0.25	0.49	0.5625	~2.5
Adhesive Used (mL)	0.05	0.1	0.11	0.5

3.5.5 Repeatability

In order to demonstrate repeatability of this uniform bond, ten shim patches were adhered to the test shaft using the updated protocol, and the mean bond layer thicknesses and error are tabulated in Table 3.9.

Over ten applications, the calculated mean bond layer thickness was 0.035 mm. The outlying value for thickness and variance in Case 9 were due to an imperfection in the curvature in the shim, as seen in Figure 3.16. Due to the imperfection, a large amount of adhesive pooled in a small section of the patch leading to the large variance from the mean measurement for that sample. Aside from one instance, this refined application method proved to be effective and repeatable, and was therefore used to repeat and extend BDQS testing results.

Table 3.9: Demonstrating repeatability of best quality bond

Test	Mean Bond Layer Thickness (mm)	Observed ±Variance From Mean (mm)
1	0.03	0.01
2	0.03	0.01
3	0.03	0.01
4	0.025	0.015
5	0.04	0.01
6	0.04	0.02
7	0.03	0.01
8	0.04	0.01
9	0.055	0.045
10	0.03	0.005

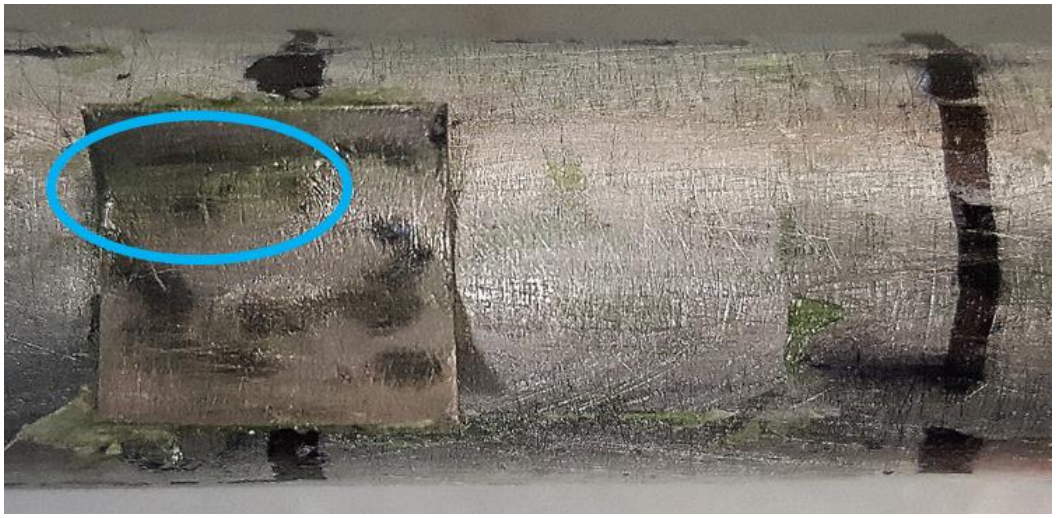

Figure 3.16: Repeatability test case 9 demonstrated a pooling of adhesive in a structural deformation present in the shim patch.

3.5.6 Additional Observations

Beyond identifying an updated bonding protocol, several other important observations were made regarding requirements for material production and sample processing. The quality of the bonds seen in this study was largely dependent on several major factors. The presence of structural imperfections or deformation in the shim led to the formation of non-uniform bond layers. In these cases, bonds would be of varying thicknesses, as adhesive would fill divots in the shim, while uniformly-shaped sections would not receive as much coverage. This is demonstrated in repeatability test case 9, pictured in Figure 3.16. This is an excellent reminder that when processing and shaping magnetostrictive materials for this purpose, special care must be taken to ensure near-perfect fit to the shaft [30], [35].

Uniform sanding of the shaft and patch also proved to be of great importance. Higher grit sandpaper (320 grit) offered generally weaker bonds than lower grit sandpaper (60 grit), and sections of shim and shaft that were not adequately roughened by either grit did not maintain as strong of a bond as those sections that were completely sanded. This was evidenced by bands of adhesive that would remain on the surface of the shaft when the shim was removed. An example is provided in Figure 3.17 where a smooth dark section of the shim resulted in the formation of an air bubble.

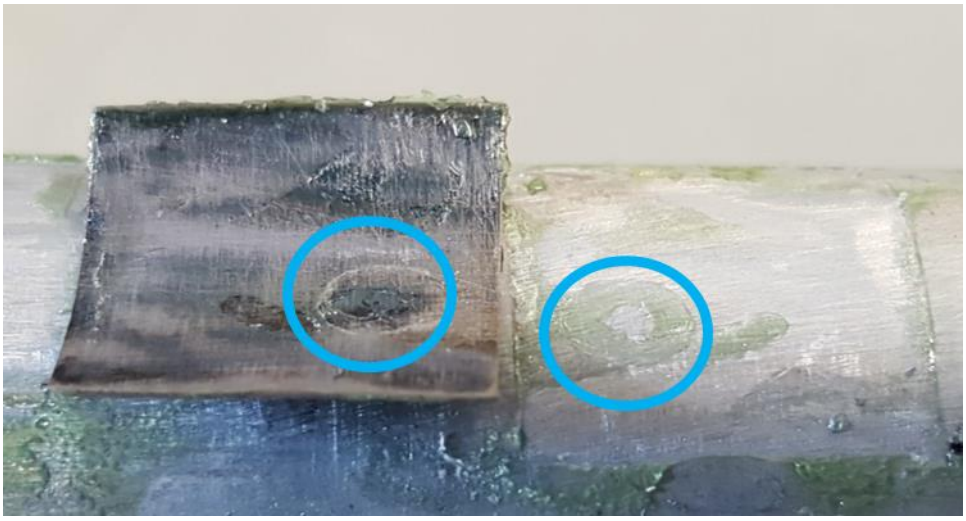

Figure 3.17: A non-uniform bond layer, with adhesive pooling around an air bubble, formed due to imperfect sanding of the shaft and shim sample.

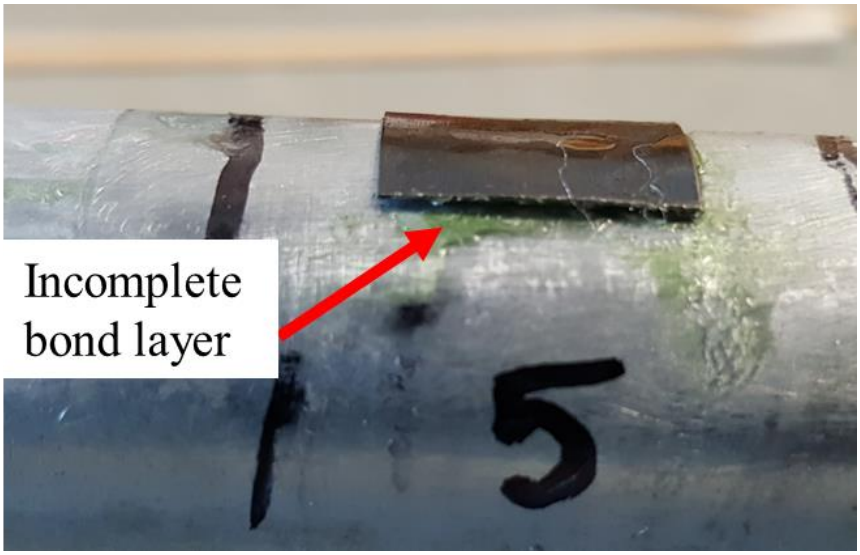

Figure 3.18: An incomplete bond layer formed due to insufficient torque application (5 in-lb) while the adhesive cured.

Likewise, uniform high torque application to samples while adhesive cures was essential for the formation of an adequate bond between the shaft and sample. See Figure

3.18, where an application of 5 in-lb resulted in the incomplete bonding of the bottom edge of one piece of shim.

3.6 Quasi-Static Test Setup

Magnetostrictive samples discussed in Section 3.1 were evaluated in bi-directional quasi-static (BDQS) testing using this improved bonding protocol. Here, outputs from the WiMET sensor and the commercial torque sensor were collected simultaneously while torques between 50 – 200 in-lb were applied to the shaft according to the convention described in Section 3.2.2. Table 3.10 provides a summary of the test cases evaluated during quasi-static testing.

Table 3.10: Quasi-static test cases

Subject	Samples Tested
BDQS Testing	FeGa Patch 1
Ring Thickness	FeGa Patch 2
Patch Comparison	FeAl Ring 1, t = 0.1mm
Shape Anisotropy	FeAl Ring 3, t = 0.15mm
Repeatability	FeAl Patch

3.6.1 Characterizing Effect of Flexible Couplings on WiMET Response

Flexible couplings were included between rotating elements in this test setup in order to minimize vibrational loading of the shaft during operation and to ensure proper alignment of rotating parts in the dynamic mode. However in the quasi-static mode, where the couplings were required to physically hold the test setup together, they introduced an angular displacement to the system beyond what would normally have occured in an

aluminum shaft under an applied torque *T*. The twist that would naturally occur in a solid shaft as a torque is applied is calculated as in Equation 3.3:

$$\varphi = \frac{Tl}{GJ} \tag{3.3}$$

Here, φ is the cross sectional angle of twist measured in radians, T is the applied torque measured in in-lb, l is the distance from the root of the shaft measured in inches, G is the shear modulus of the material measured in psi, and J is the polar moment of inertia measured in in^4.

To characterize the effect of the flexible couplings, the shaft was etched in two locations, and bi-directional loads were applied to the shaft as images were captured from above using the setup shown in Figure 3.19. One etch was made near the center of the patch and another was made along the bottom edge of the patch, as seen in Figure 3.20. Theoretical values of twist are tabulated in Table 3.11 between 50 and 200 in-lb assuming that twist is measured 9 in from the root of the aluminum shaft, where the FeGa patch was mounted when experimental twist measurements and images were taken.

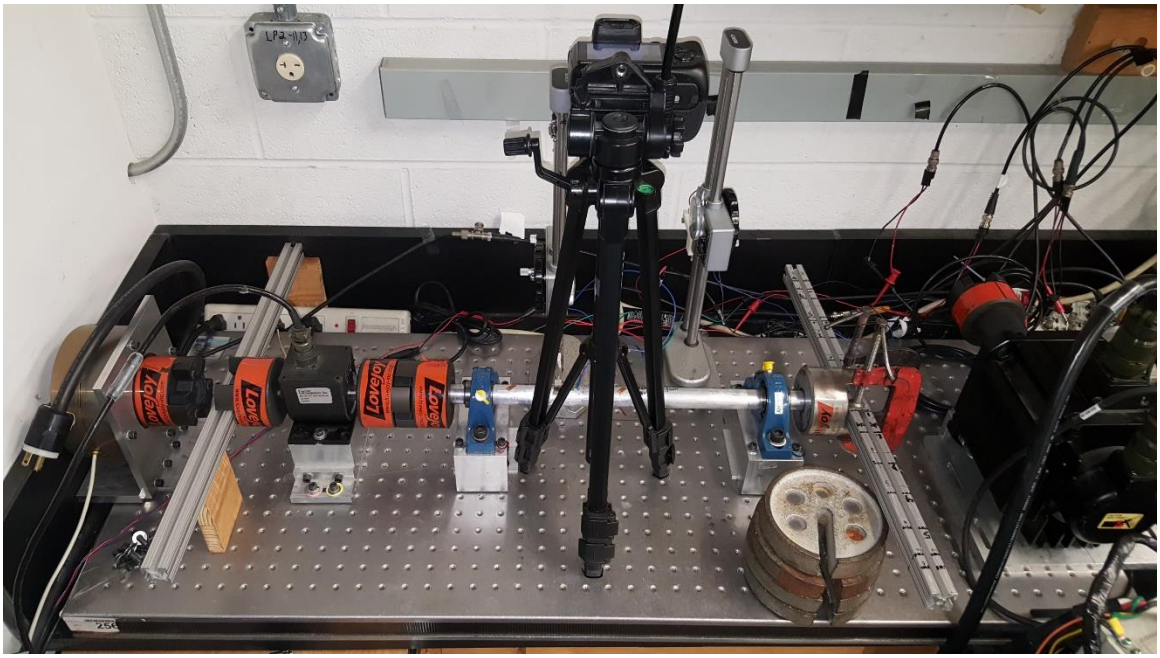

Figure 3.19: A camera mounted above the test section provided images of the shaft during and after torque applications.

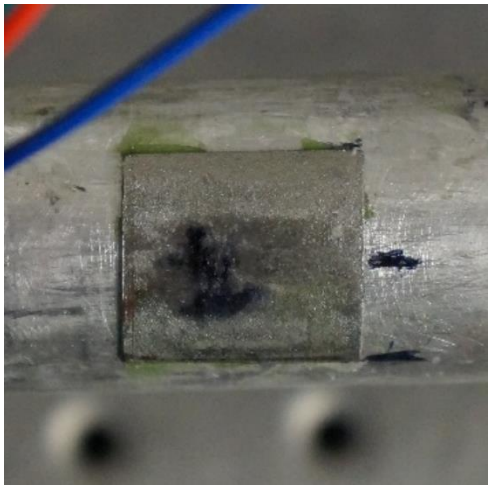

Figure 3.20: Etches were made adjacent to the magnetostrictive sensing element while adhered to the shaft in order to calculate angular displacement under applied bi-directional torsional loading.

Table 3.11: Torque and theoretical twist in aluminum shaft, nine inches from fixed end

Torque	Twist (degrees)
50	0.07
100	0.14
150	0.21
200	0.28

Image J, an image analysis program created by NIH, was used to identify the cartesian *y*-coordinates of individual pixels along the bottom and top edges of the shaft. Using these coordinates, a scale converting pixels to inches was calculated for each test case such that the distance between the top and bottom edges as measured in pixels was equal to 1 inch, the diameter of the shaft. The midpoint *y*-coordinate of the shaft in each image was determined by averaging the top edge and bottom edge *y*-values, as seen in Figure 3.21.

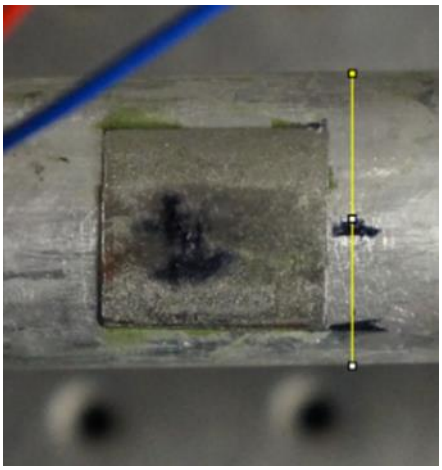

Figure 3.21: An ImageJ screenshot shows a yellow line which provided the coordinates of the top edge of shaft, the bottom edge of shaft, and a midpoint between the two.

Additionally, the coordinates along the bottom of the etches were noted and compared between two images. One image was captured while a load was applied, and another was captured after the load was removed. By comparing the two images as in Figure 3.22, the distance in inches between the midpoint and each etch (x_1 and x_2) was calcluated and converted to angles θ_1 and θ_2. Angular displacement of the shaft was calculated as the difference between the two angles.

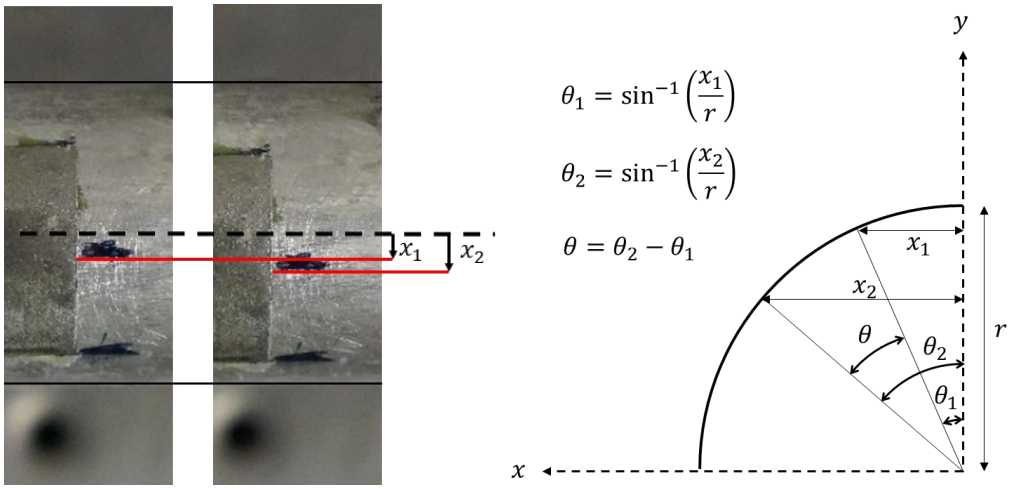

(a) (b)

Figure 3.22: Angular displacement was determined by (a) measuring x_1 and x_2 for each etch and (b) calculating the difference of angles θ_1 and θ_2 with respect to the midpoint. x_1 was measured when no load was applied, and x_2 was measured when a was applied.

Angular displacement of the shaft was observed to be roughly an order of magnitude larger than the previously calculated theoretical twist: theoretical twist was ~0.3˚, while angular displacement due to the inclusion of flexible couplings was ~7˚ under a 200 in-lb torque. This additional rotation was comparable bi-directionally, varying at

most by ~1˚ at ± 200 in-lb. Based on these results, it is reasonable to assume that in addition to torque-induced twist, the shaft experienced an additional angular displacement due to the "give" in the flexible couplings, and as such, determining quasi-static signal response without this variation would require a test setup without flexible couplings. When this was observed, it was unclear if this would impact the results of quasi-static or dynamic testing. Modelling results in Figures 2.16 – 2.17 suggested that magnetic flux leakage would be variable along the edge of the patch and maximized at its corners, so in the quasi-static mode, the Hall effect sensor was placed over the center of the edge of the patch in order to minimize any impact on WiMET signal from this effect.

3.6.2 Difference Between Measured and Modeled Strain

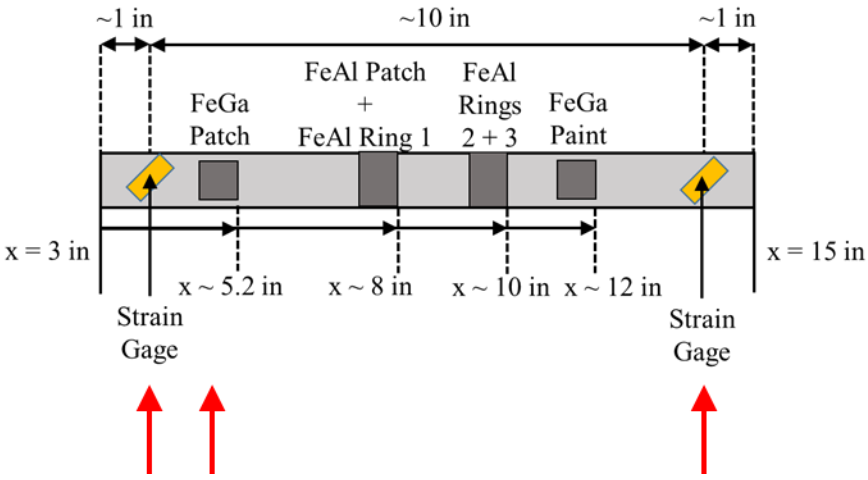

Figure 3.23: Strain gages were mounted 10 in apart, on either end of the test section, and atop the FeGa patch to determine if the position along the shaft of each magnetostrictive sample would impact sensor performance and to determine the decrease in principle strain between the surfaces of the aluminum shaft and FeGa patch.

In order to determine if the location where samples were mounted on the shaft would affect sensor performance, two strain gages were mounted on either end of the test section, 10 in apart, as shown in Figure 3.23. Likewise, a strain gage mounted atop the FeGa patch provided an estimate of strain lost between the surface of the shaft and the surface of the patch.

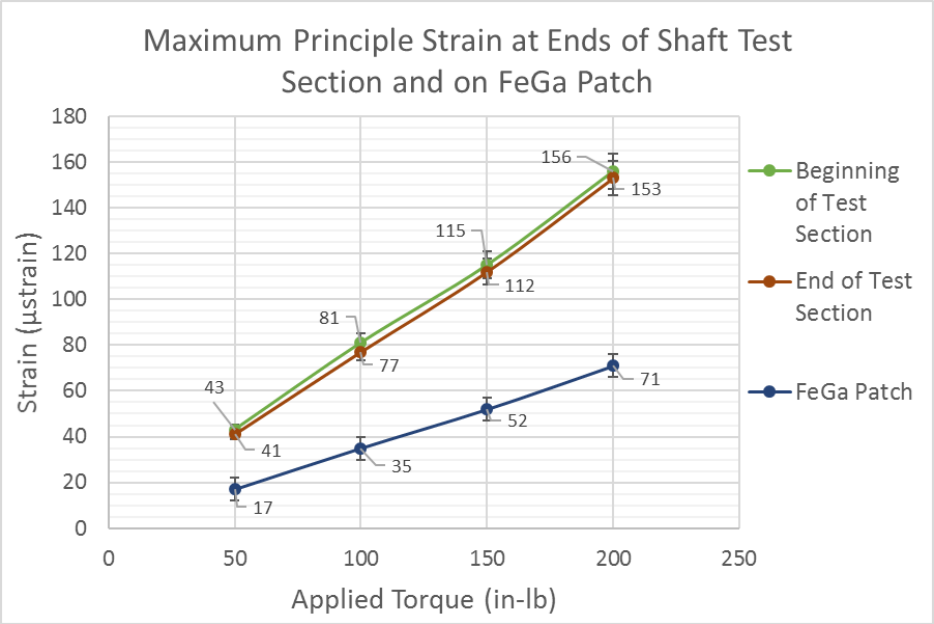

Figure 3.24: Maximum principle strain (µstrain) measured at +45˚ from the longitudinal shaft axis varied little between opposite ends of the test section (10 in apart) and decreases by ~54% between the shaft and the FeGa patch (mounted in the center of the test section).

Experimental results from strain gages mounted on the aluminum shaft in the direction of principle strain are summarized in Figure 3.24, and suggested that there was relatively little difference (error bars overlapped) between principle strain as measured at +45˚ from the *x*-axis at the two locations shown in Figure 3.23 while positive torsion was

applied. These gages measured only a 3 μstrain difference in response at +200 in-lb and subsequent tests showed at most a 10 μstrain or ~7% decrease between the two gages. Considering the location of magnetostrictive sensing elements seen in Figure 3.23, it is likely that at most a ~3.5% decrease in strain was experienced on the shaft between the locations of the FeGa and FeAl samples which were mounted at most ~5 in apart. As such, variation of strain along the length of the test section is expected to have minimal effect on the variation in performance between individual magnetostrictive sensing elements.

By contrast, modeling results in Chapter 2 suggested that there should have been a large variation in the principle strain present along the surface of the shaft between the beginning and end of the test section. Two points, located at the same locations evaluated in Figure 3.23 experienced a strain of 88 μstrain and 36 μstrain respectively in the COMSOL model (a 60% decrease), as seen in Figure 2.14. This difference in response between the modeled and experimental cases is not well explained by only the difference in how load application was modeled and how it was physically applied to the system. Namely, a distributed total force was applied to the shaft as calculated in Equation 2.20 for ease of modeling in COMSOL, while in physical testing the weight was not distributed; rather, a weight was applied at the end of a moment arm mounted opposite the fixed end of the shaft as demonstrated in Figure 3.6.

Modeling also suggested that a decrease in principle stress and strain on the order of ~10% (from ~67 μstrain on the shaft to ~60 μstrain on the center of the patch) should have been observed between the shaft and the patch at an applied torque of +200 in-lb, as seen in Figures 2.10 and 2.14 respectively. However, the COMSOL model assumed a perfect bond between the shaft and the FeGa patch which should not be expected in the

physical test setup due to the presence of an interstitial adhesive bond layer. Experimental strain measurements seen in Figure 3.24 show that a ~54% decrease in strain should be expected between the shaft and the center of the patch. Table 3.12 summarizes expected strain on each element while considering the location of each element along the test section. The strain transfer to FeGa flakes in the paint sample in unknown. Unlike the patches, the paint was applied directly to the shaft without the use of sandpaper to roughen the shaft surface.

Table 3.12: Relative position and expected strain at each sample edge during quasi-static and dynamic testing

Sample	Edge	Sample Dimensions (in)	Edge Position (in from fixed end of shaft)	Strain on Sample (μstrain)
				Based on Measurements **
FeGa Patch 1 Edge (a)*	Left	0.7 x 0.7	~4.5	71.5
	Right		~5.2	71.4
FeAl Patch	Left	0.75 x 0.75	~7.2	71.1
	Right		~7.9	71
FeAl Ring 1, 0.1mm	Left	0.75 x 3.14	~7.2	71.1
	Right		~8.0	71
FeAl Ring 3, 0.15mm	Left	0.75 x 3.14	~9.2	70.8
	Right		~10.0	70.7
FeGa Paint	Left	0.8 x 0.8	~11.2	70.6
	Right		~12.0	70.4

*Right edge is edge (a)

** Assumes reduction of ~54% between shaft and patch

3.7 Dynamic Test Setup

The goal of dynamic testing was to characterize the performance of magnetostrictive samples of varied shape and composition over a range of applied speeds between 0 – ±2000 RPM and over a range of applied torques between 0 – 200 in-lb. These dynamic test cases are summarized in Table 3.13.

Table 3.13: Dynamic test cases

Subject	Samples Tested
Dynamic Testing	FeGa Patch 1 FeAl Ring 1, t = 0.1mm FeAl Patch FeGa Paint
RPM Variation	
Rotation Direction Variation	
Extended Data Sets	
Repeatability	

Between quasi-static and dynamic testing, the benchtop test setup underwent a series of modifications. The moment arm used for torque loading was removed, and a driving motor was installed in its place in-line with the shaft to the right of the test section, as pictured in Figure 3.25. Likewise, the brake used for quasi-static testing was replaced with a magnetic particle brake to allow for torque loading in the dynamic mode. No changes were made to the height-gage-mounted WiMET sensor as previously described in Section 3.2.1, and a second identical sensor was added to the benchtop setup to allow for additional data to be gathered. These components are detailed in Table 3.14.

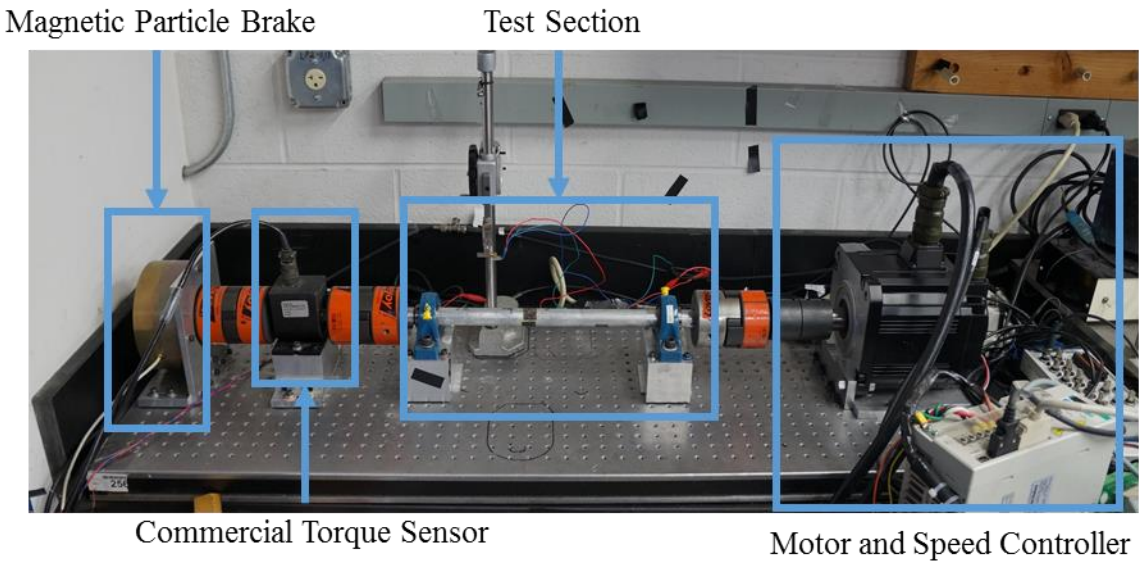

Figure 3.25: The dynamic test setup included a motor to drive the shaft, a speed controller to vary RPM, and a magnetic particle brake to apply torque to the test section.

Table 3.14: Dynamic system specifications

Part	Specifications	Manufacturer	Details
Driving Motor	Rated Speed: 2000 RPM Rated Torque: 126 in-lbs Rated Power Output: 4 HP	SureSERVO	Servo Motor
Brake	Max Speed: 1800 RPM Max Torque: 220 in-lbs Operating Voltage: 24 V	Placid Industries Inc.	Magnetic Particle Brake
Torque Sensor	Max Speed: 5000 RPM Max Torque: 200 in-lbs	Sensor Developments Inc.	Rotary Shaft-Slip Ring
Shaft	Diameter: 1 in Length of Test Section: 10 in Length of Shaft: 24 in	Mc-Master-Carr	Aluminum
Magnetic Flux Piece	Dimensions: 1.18 x 0.2 x 0.2 in	Mc-Master-Carr	Steel, High Permeability
Hall Effect Sensor	Sensitivity: 130 mV/mT @ 5V input voltage	Asahi Kasei Microdevices	Hybrid Linear Hall Effect Ics EQ-series
Bias Magnet	Residual flux density: 6800 G	McMaster-Carr	Nd-Fe-B disk

3.7.1 Operational Limits

The operating window of the system was limited primarily by the magnetic particle brake and the commercial torque sensor, which allowed for a maximum rotation rate of 1800 RPM and a maximum applied load of 200 in-lb respectively. Additional considerations were made for the brake, as the maximum RPM was set by the manufacturer to ensure that the device does not overheat. According to the manufacturer, the brake is rated to a maximum heat dissipation of 110W, as calculated by Equation 3.4, and the resulting recommended long-term operation window for the brake is plotted within the colored region of Figure 3.26.

$$Heat\ \langle Watts \rangle = RPM \times Torque \langle in \cdot lb \rangle \times 0.012 \tag{3.4}$$

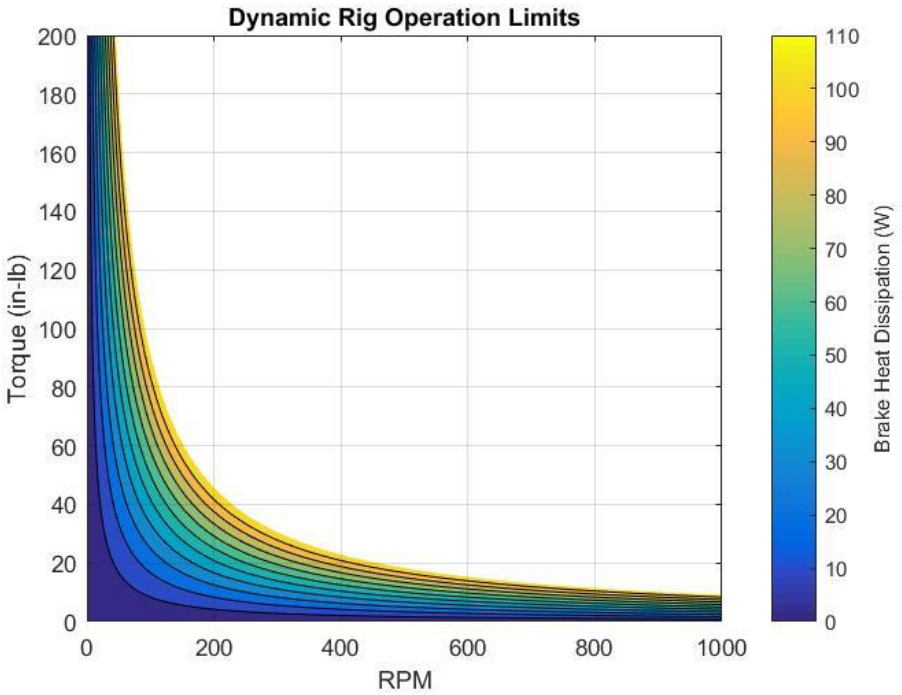

Figure 3.26: Brake heat output (W) less than 110 W is plotted as torque (in-lb) and RPM are varied.

This heat output was allowed to be exceeded for short periods of time, as long as maximum case temperature never exceeded 160˚F as measured constantly by a thermocouple and periodically by a handheld infrared thermometer gun [48]. Therefore, tests with speed in excess of 1800 RPM (up to 2000 RPM) were allowed, but operation time was limited to a 10 second window for all tests in order to avoid overheating of the brake.

Over the course of all test runs, the input voltage applied to the magnetic particle brake was independently varied, and the resulting torque, measured with the commercial in-line torque sensor, was averaged for each input voltage to produce the brake calibration curve in Figure 3.27, while Table 3.15 lists the speeds and torques applied to the shaft during dynamic testing.

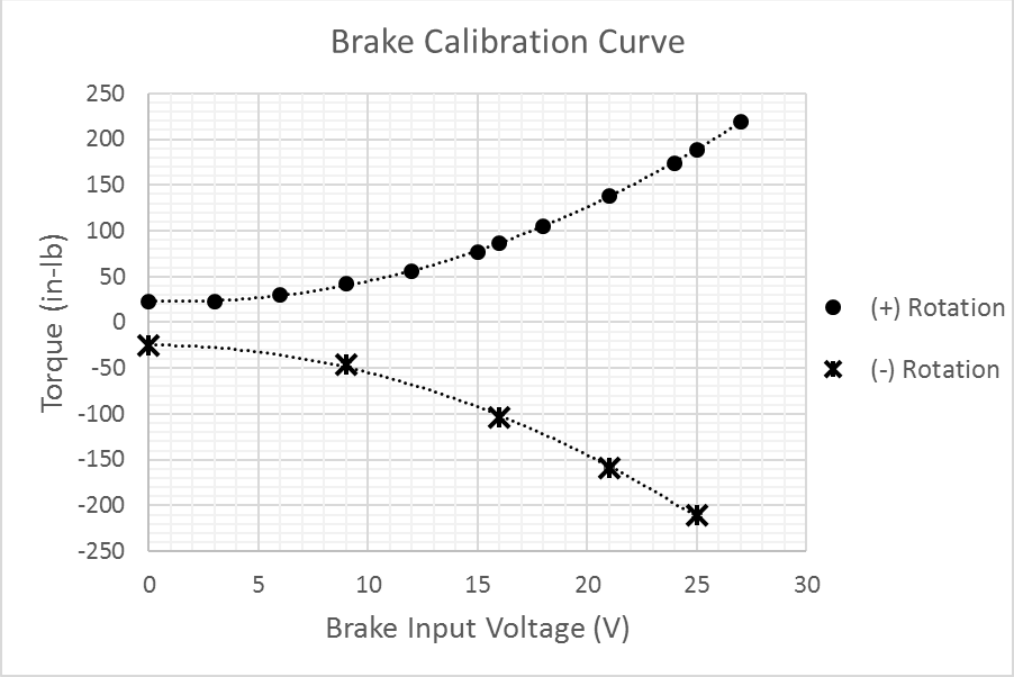

Figure 3.27: Torque (in-lb) increased bi-directionally as input voltage to the magnetic particle brake (V) was increased.

Table 3.15: Speeds and applied torques tested in the dynamic mode

RPM	Torque (in-lb)	
	(+) Rotation	(-) Rotation
±500	+23, 42, 86, 138, 188	-
±1000	+23, 30, 42, 56, 77, 86 105, 138, 174, 188, 220	-26, -46, -104, -159, -210
±1500	+23, 42, 86, 138, 188	-
±2000	+23, 42, 86, 138, 188	-

Chapter 4: Experimental Results and Analysis

This Chapter details the results of quasi-static and dynamic testing of FeGa and FeAl samples of varied shape and composition to characterize the response of each sample for torques between 0 – 200 in-lb and for bi-directional rotation at speeds from 0 – ±2000 RPM.

4.1 Quasi-Static Benchtop Testing

This section details the results of testing carried out to evaluate the bi-directional response of the WiMET sensor in quasi-static mode. After a discussion of testing procedure and data analysis, results for quasi-static testing are summarized. Assuming a linear response from the WiMET sensor, the relative sensitivity was then calculated for each material considering the increase in signal observed over a range of applied torques.

4.1.1 Testing Procedure

Each test was run for approximately two minutes. Loads were applied in 20 second intervals, with 10 second intervals with no load applied between intervals with a load. A detailed schedule can be seen in Table 4.1.

Table 4.1: Quasi-static testing schedule

Interval	1	2	3	4	5	6	7
Start Time (sec)	0	20	40	50	70	80	100
End Time (sec)	20	40	50	70	80	100	110
Load	Off	On	Off	On	Off	On	Off

Loads were applied by placing weights at the end of a lever arm, as described in Section 3.2.2. A single load case (i.e. ±50, 100, 150, or 200) was applied three times during each test. 50 in-lb would be applied three times in one test, 100 in-lb in another, and so on. Hall effect sensor and commercial torque sensor outputs were simultaneously recorded during each test via a Labview interface which continually recorded their respective signals at a sampling rate of 500 Hz.

4.1.2 Data Analysis

During Intervals 2, 4, and 6 (as defined in Table 4.1), the voltage measured by the Hall effect sensor increased sharply as the load was applied, as seen in Figure 4.1. Figure 4.1 (a) shows six separate tests superimposed in one image and Figure 4.1 (b) shows Interval 2, when the first of three 50 in-lb loads was applied.

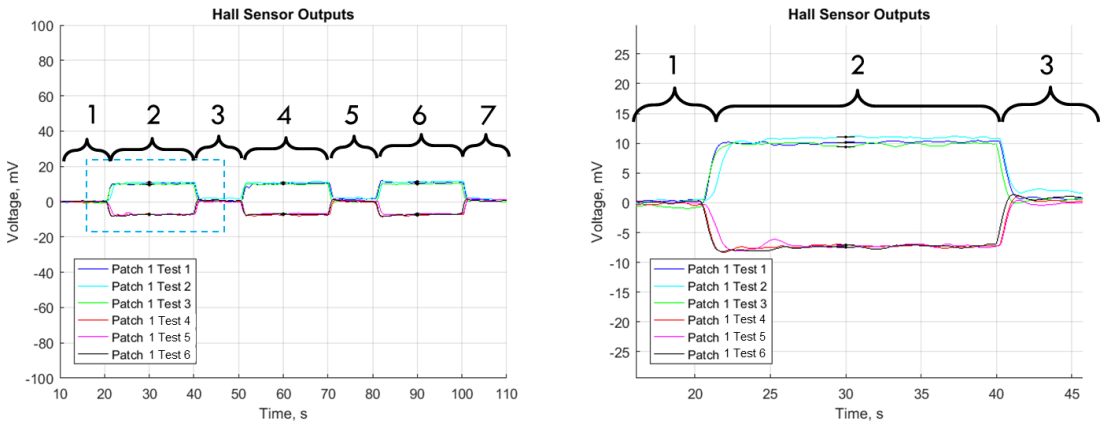

(a) (b)

Figure 4.1: The Hall effect sensor signal (mV) is shown for six tests in (a) blue, cyan, and green while three +50 in-lb torques are applied and in red, pink, and black as three -50 in-lb torques are applied, with (b) a zoomed image of the first load application.

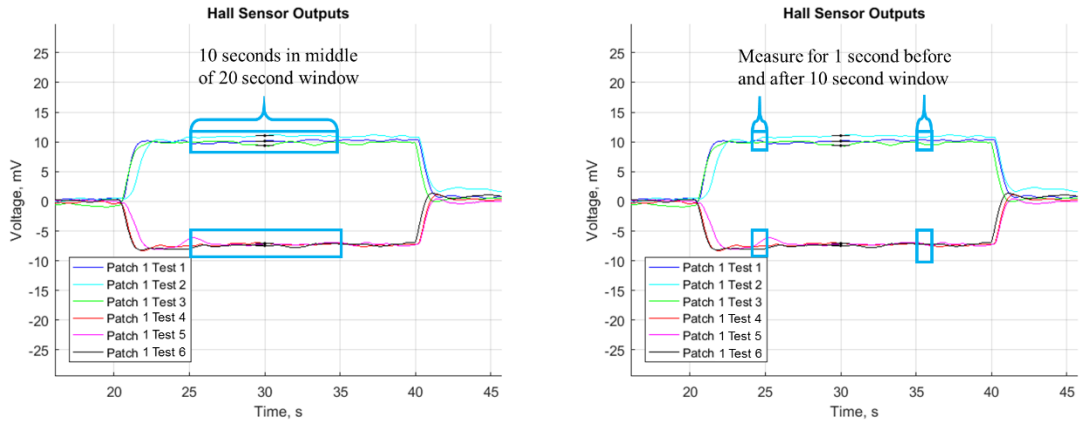

(a) (b)

Figure 4.2: The filtered Hall effect sensor signal was sampled to determine the (a) mean voltage output over 10 seconds and b) signal drift over 10 seconds.

Mean signal magnitude was computed using data from the middle 10 seconds of each 20 second load interval in order to ensure that the signal would remain unaffected by any data acquired as weights were physically applied to and removed from the moment arm. For instance, only data from between 0:25 and 0:35 were considered for Interval 2, as seen in Figure 4.2(a). Figures 4.1 – 4.2 show a 2 – 3 second period where the signal increased (slightly after 0:20) or decreased (slightly after 0:40) as weights were physically applied to or removed from the moment arm, respectively.

A mean zero was calculated by averaging the signal magnitude during Intervals 3, 5, and 7, after each load was removed. By subtracting the mean zero from the mean signal magnitude as loads were applied, a true signal mean was calculated. Error in the mean signal was calculated as standard error from the mean, $\sigma_{\bar{x}}$, such that:

$$\sigma_{\bar{x}} = \frac{\sigma}{\sqrt{n}} \tag{4.1}$$

Here, σ is the standard deviation and n is 3, the number of samples.

As seen in Figure 4.2(b), drift was calculated by taking the difference in mean signal over a one second interval before and after the 10 second data collection interval, such that drift as a percent of the mean signal was evaluated as in Equation 4.2:

$$Drift_{as\,\%\,of\,Mean} = \frac{Drift}{Signal\,Mean} \times 100\% \tag{4.2}$$

4.1.3 Results

The results of BDQS testing using the improved adhesive application protocol are summarized in Figures 4.3 – 4.4, which depict signal magnitude and signal drift as percent magnitude respectively. Specifically, results were gathered for FeGa patch 1 Edge (a), FeAl Rings 1 and 3, an FeAl patch, the FeGa paint sample, and the aluminum shaft. The responses of the 0.1 and 0.15 mm FeAl rings are compared, as are the responses of the FeAl and FeGa patches.

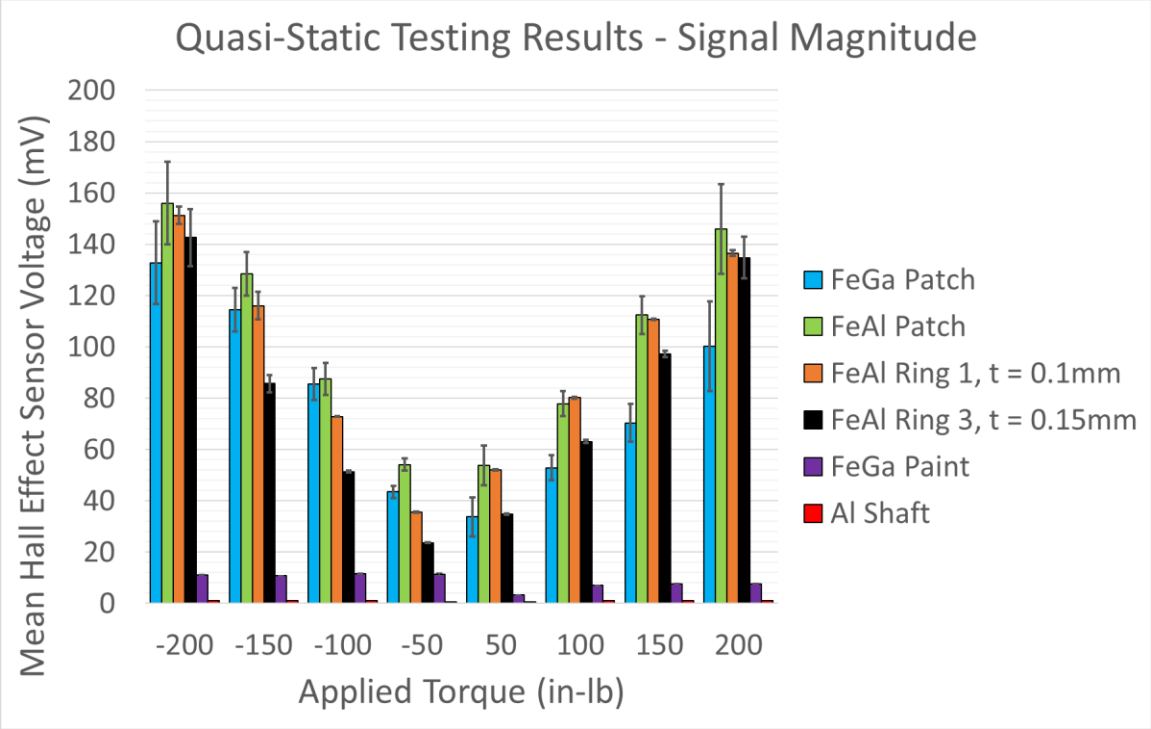

Figure 4.3: An increase in output magnitude was observed for all samples after changes were made to the adhesive application protocol.

As seen in Figure 4.3, readings taken over the aluminum shaft did not increase as larger torques were applied to the shaft. For all other cases, a bi-directional increase in signal was observed as applied torque was increased from ±50 in-lb to ±200 in-lb. Overall, a factor of 2 – 3 increase in signal magnitude for each adhesively applied sample was attributed to the improved bonding protocol established in Section 3.5. Across all cases, observed drift expressed as a percent of the mean signal was less than 2.5%, and it tended to decrease as higher loads were applied with the exception of a few outliers, as seen in Figure 4.4.

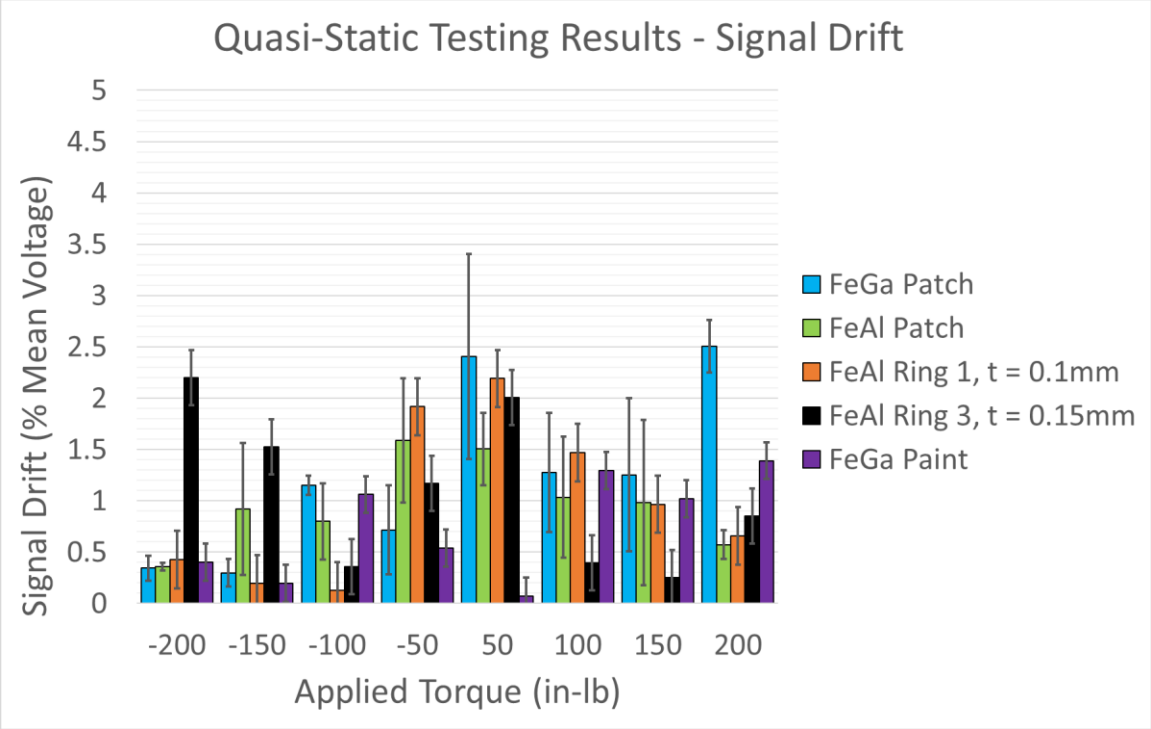

Figure 4.4: The tendency of drift to increase or decrease as larger torques were bi-directionally applied varied on a sample-by-sample basis.

The FeAl patch outperformed the FeGa sample of similar shape across all load cases, but the overall responses of the two samples were similar. FeAl signal varied by ~15 mV at most depending on load direction, while FeGa outputs varied by ~45 mV at most. Drift remained less than 2.5% of the signal mean in all cases, and tended to decrease as load increased bi-directionally, with the exception of the +200 in-lb case for the FeGa Patch.

The FeAl rings provided responses of similar magnitudes, especially in high torque cases, but Ring 1 (0.1mm thick) provided slightly greater output magnitude than Ring 3 (the 0.15mm ring) across all load cases. For the two ring samples, trends in drift were generally similar as applied loads increased bi-directionally: drift increased between -100

and -200 in-lb for both samples, but under positive loading Ring 3 experienced a slight increase, rather than decrease, in drift at +200 in-lb. Overall, maximum mean variance in signal was about 15 mV between the bi-directional cases, and signal drift in both cases remained less than 2.5% of mean signal.

A standard error of ~10mV occurred in the high load cases for Ring 3 due to a drift in Hall effect sensor output, as seen in Figure 4.5. As a reminder, "drift" as presented in these results considers the drift present in each load case; it does not consider the drift between measurements which is represented in standard error.

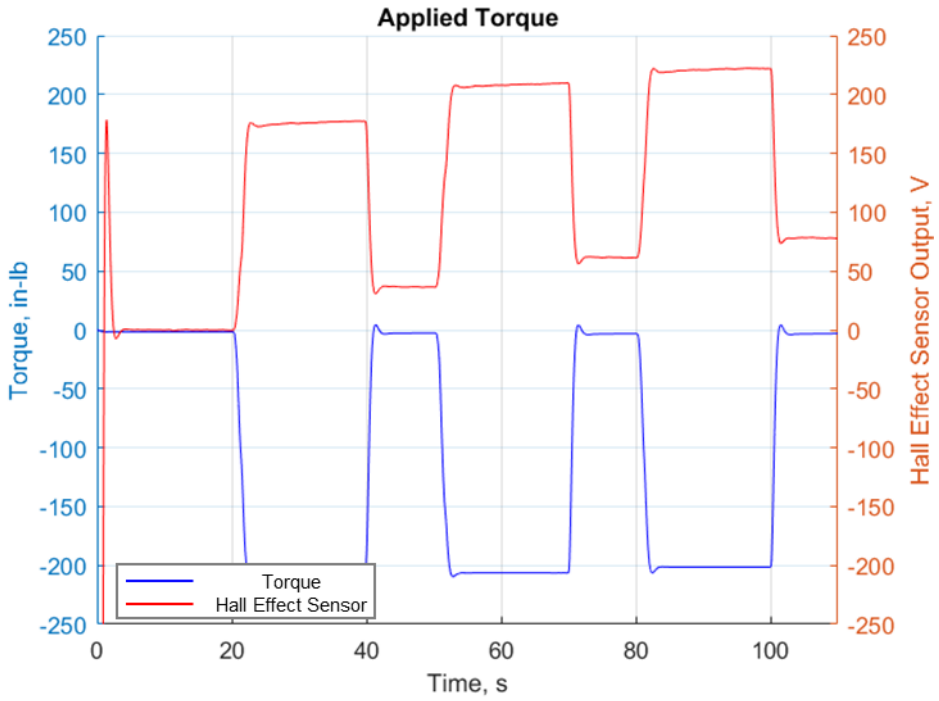

Figure 4.5: A 0.15 mm thick FeAl ring was tested with a load measured by the commercial torque sensor (blue) and with the Hall effect sensor (red) showing evidence of error in the no-load response between measurements. Loads are applied between 0:20 – 0:40, 0:50 – 1:10, and 1:20 – 1:40.

4.1.4 Repeatability

As the ability to repeatedly acquire the same signal output for given torque inputs is desirable, the magnitude and drift in response of FeGa Patch 1 Edge (a) and the FeAl Patch were evaluated over three test runs as shown in Figures 4.6 – 4.7. The typical static testing procedure of previous tests was repeated; loads between 50 and 200 in-lb were applied bi-directionally, and the Hall effect sensor output voltage was recorded. Before every test, the patches were removed from the shaft, cleaned, sanded, and reapplied using the refined protocol discussed in Section 3.5.

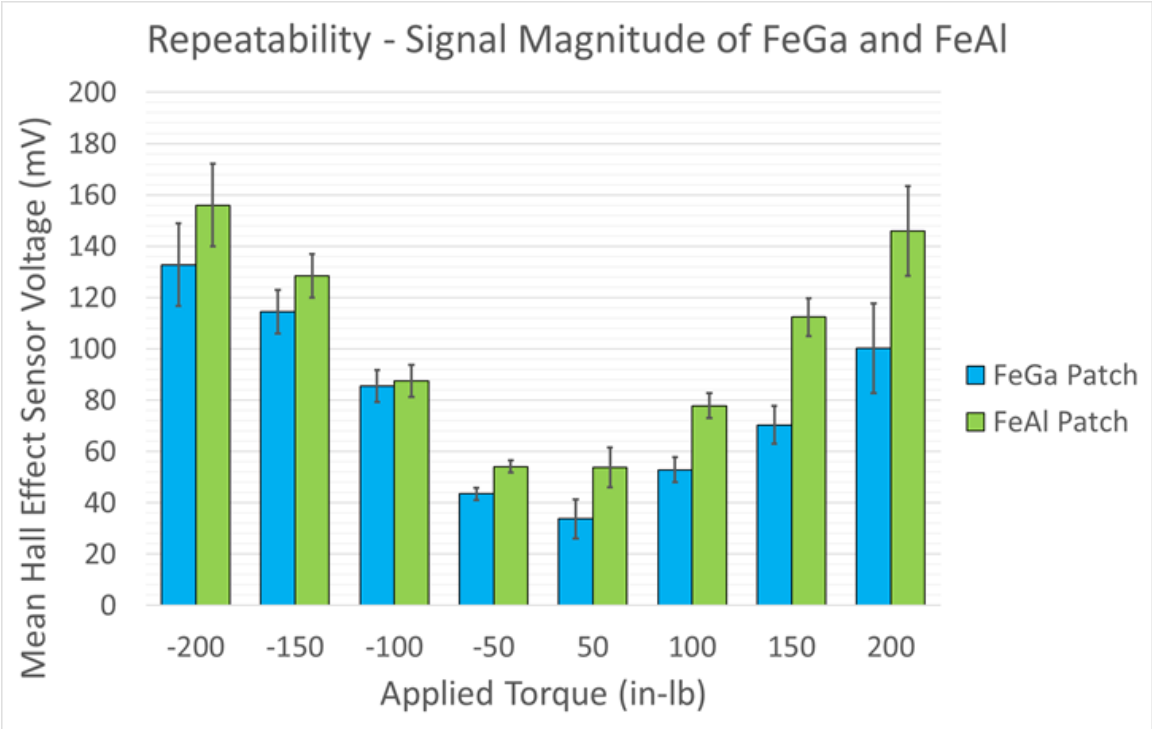

Figure 4.6: FeAl Patches provided a larger output signal than FeGa across most cases.

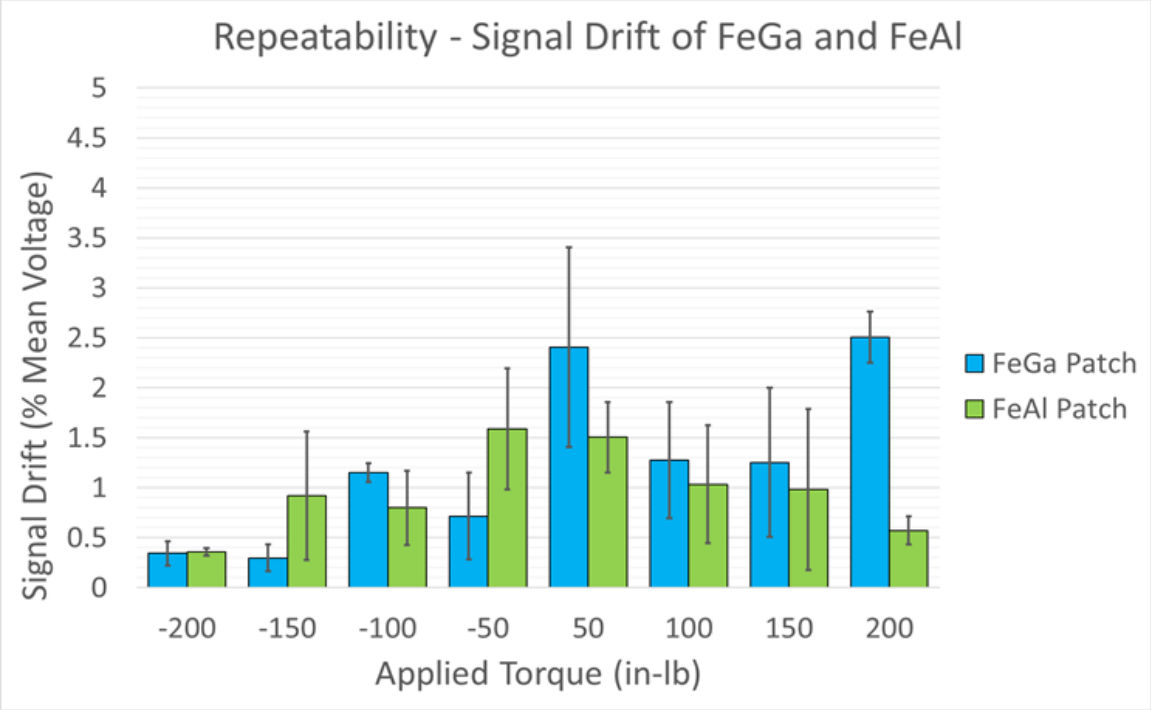

Figure 4.7: Over three individual test cases, FeGa and FeAl Patches experienced the highest drift (still < 2.5% mean) at ±50 in-lb and generally under positive loading.

In all three cases, output voltage increased as applied torque increased, and the mean response under positive loads was less than the response under negative loads, which is consistent with results acquired before the refined adhesion protocol was implemented. High variance between maximum and minimum signals was observed in the highest load cases: upon application of -200 in-lb, signals recorded in two tests varied by 50mV, and upon application of +200 in-lb, a 70 mV difference was observed. Mean voltage varied by 30 mV between these highest load cases and varied by 20 mV or less for cases between -100 and +100 in-lb. Signal drift remained below 3% of mean for most cases (with the exception of Test 2 for +50 in-lb and Test 1 for +200 in-lb) and remained below 5% of mean for all cases. This variation in response, especially under positive torque application,

may have be due to inconsistent sensor element placement between tests, potential saturation of the Hall effect sensor, the effects of shaft rotation, or a combination of the three.

The peak response of FeAl remained consistently greater than that of FeGa in these test cases. Mean peak response between positive and negative torques of the same magnitude remained comparable in all torque cases, and mean drift tended to decrease as loads increased in magnitude bi-directionally. The greatest variance observed between mean peak signals was about 15 mV in the ± 150 in-lb case, and drift remained below 3% mean for all torque cases.

4.1.5 Sensitivity

Considering operation between 0 and 200 in-lb and assuming a nearly linear signal response as load was increased, the sensitivity of each sample was evaluated as the change in peak signal over the 50 – 200 in-lb range of applied torques via Equation 4.3. These values are summarized in Table 4.2, and they are presented in Figure 4.8 overlaid with the results from Section 4.1.4.

$$Sensitivity = \frac{\Delta\ Hall\ Effect\ Sensor\ Signal}{Range\ of\ Applied\ Torque} \tag{4.3}$$

Table 4.2: Sensitivity of magnetostrictive sensing elements in the quasi-static mode

Sample	Sample Dimensions (in)	Sensitivity (mV/ft-lb)		Sensitivity (mV/in-lb)		Signal Drift (% Mean)	
		-	+	-	+	-	+
FeGa Patch 1 Edge (a)	0.7 x 0.7	7.1	5.2	0.59	0.43	0.6	1.9
FeAl Patch	0.75 x 0.75	8.3	7.4	0.69	0.62	0.8	0.9
FeAl Ring 1, 0.1mm	0.75 x 3.14	9.4	6.9	0.78	0.57	0.7	1.3
FeAl Ring 3, 0.15mm	0.75 x 3.14	9.4	8.0	0.78	0.67	1.3	0.9

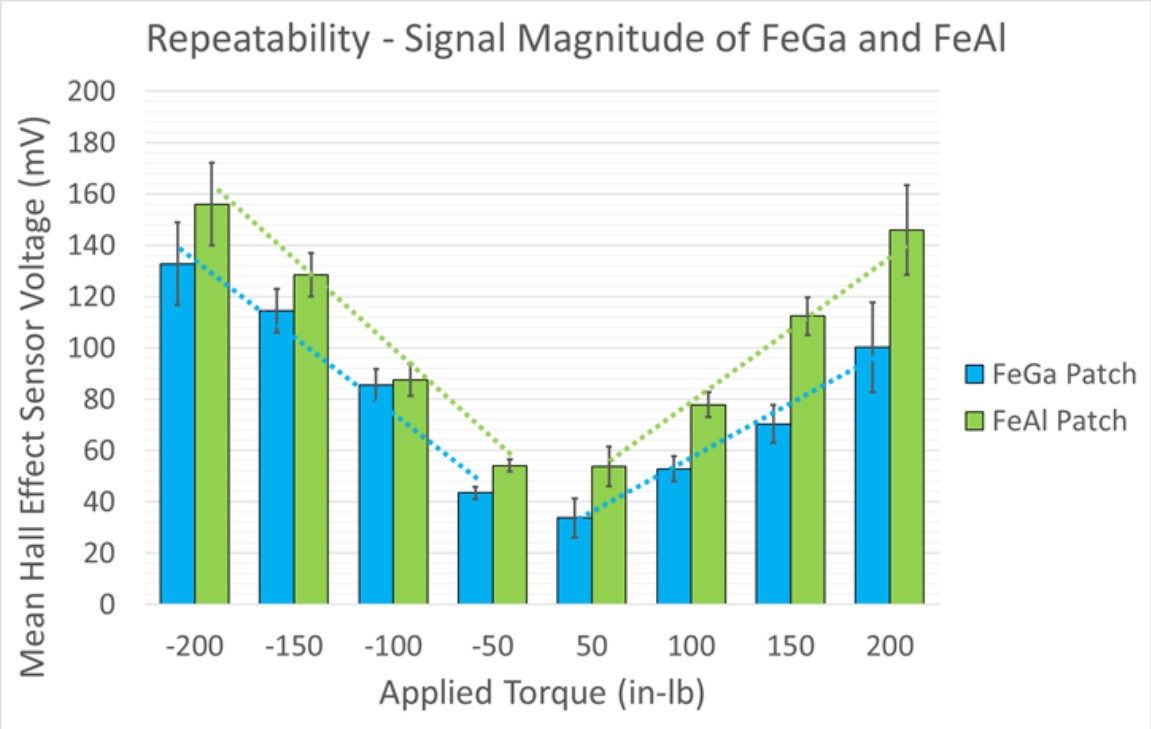

Figure 4.8: The sensitivity (mV/in-lb) is considered as a change in Hall effect sensor output (mV) over a range of applied torques (in-lb)

The FeGa sample provided more sensitive response under negative torsion than positive torsion, and exhibited greater signal drift under positive torsional loading. The FeAl patch provided slightly higher sensitivity than FeGa with low variance in response between directions, and it produced mean drift less than 1% of mean signal response. The 0.1mm thick FeAl ring provided slightly lower bi-directional sensitivity than the 0.15mm thick ring, which provided the highest overall sensitivity, and both rings exhibited comparable drift magnitudes.

4.2 Dynamic Benchtop Testing

This section details the efforts made to characterize sensor performance in the dynamic mode considering variations to RPM, rotation direction, and applied torque for four magnetostrictive samples. The section begins with a discussion of testing procedure and data smoothing methods, followed by an overview of dynamic testing results.

4.2.1 Testing Procedure

The same general testing procedure was followed for all test cases. FeGa Patch 1 Edge (a), an FeAl patch, a 0.1mm thick FeAl ring, and a "FeGa flake paint" sample (with random orientation of flakes) were adhered to the shaft for dynamic testing. For the patch and ring samples, only edges with a known circumferential crystal orientation of <100> were tested, due to the favorable properties of the easy magnetization axis described in Section 1.3.1. A Hall effect sensor was positioned above the edge of each magnetostrictive patch, and the height gages upon which they were mounted were secured to the underlying optical bench to prevent movement of the Hall effect sensor relative to the shaft during

high RPM testing. A voltage between 0 and 27 V was provided to the magnetic particle brake in order to apply torque between 0 and ~220 in-lb to the rotating shaft.

The RPM of the driving motor and the torque applied to the shaft were independently varied while output measurements of each Hall effect sensor were recorded. Each test was conducted for 30 seconds, during which the motor was run for a 10 second interval between about 0:10 and 0:20 seconds, and measurements of the dependent variables were made during this period. After the application of a moving average filter, the peak Hall effect sensor output was recorded once per rotation between 0:15 and 0:20 seconds, and these values were averaged to calculate a mean signal for a given RPM and input torque.

The execution order of individual test cases was determined by assigning a number to each test and randomizing the set of numbers, and an example is provided in Table 4.3.

Table 4.3: Randomization scheme and execution order of tests characterizing the response of an FeAl ring and FeGa Paint at 1000 RPM

File Name (Test_#)	Amp Factor	Random #s	Execution Order
234, 244, 248	0	1 2 3	20, 22, 18, 14, 24, 19, 23, 29, 27, 4, 8, 26, 1, 15, 11, 9, 28, 5, 12, 30, 21, 2, 17, 16, 3, 6, 13, 7, 25, 10
231, 240, 249	3	4 5 6	
232, 238, 252	6	7 8 9	
237, 241, 254	9	10 11 12	
225, 235 251	12	13 14 15	
224, 245, 246	15	16 17 18	
222, 227, 243	18	19 20 21	
223, 226, 228	21	22 23 24	
230, 233, 253	24	25 26 27	
229, 239, 242	27	28 29 30	

4.2.2 Data Analysis

To smooth data during dynamic operation, a moving average filter was implemented in Matlab to eliminate outlying data points. The moving average of every three data points was calculated, and the corresponding lowpass filter used coefficients equal to the reciprocal of the span. This is referred to as a span-three moving average filter.

4.2.2.1 Effect of Moving Average Filter on Response

Filters with larger spans (i.e. considering a moving average of every 5 or 7 elements) were first implemented, but at a sampling rate of 1000 Hz, peak Hall effect sensor output values for smoothed data sets tested at 2000 RPM decreased dramatically as seen in Figure 4.9.

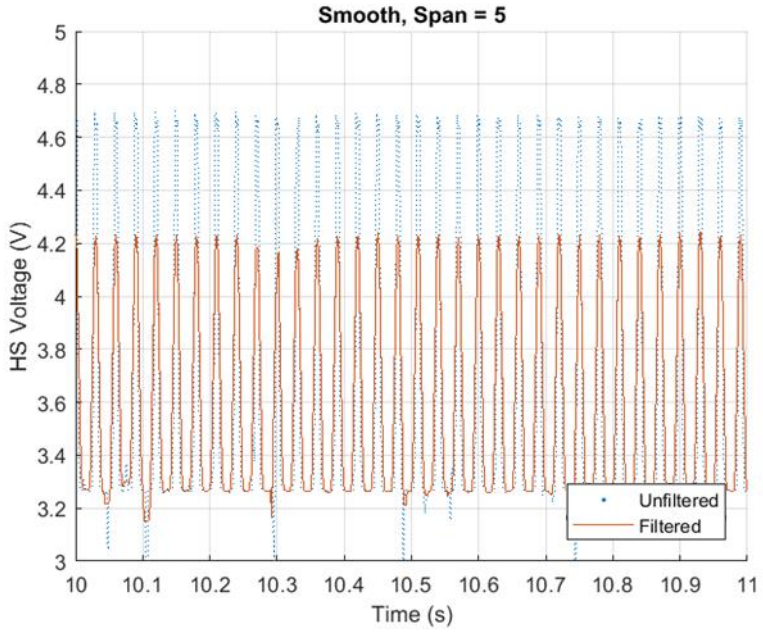

Figure 4.9: A span-five moving average filter reduced peak Hall effect sensor output values by ~450 mV @ 2000 RPM.

This decrease in signal was undesirable, as COMSOL modeling results from Section 2.4 suggested that maximum flux leakage occurred at the corners of the patch. Therefore, it was desirable to sample the peak signal value of each pass to accurately evaluate change in signal as applied load was varied. A decrease in signal due to the implementation of a span-three moving average filter at a 1000 Hz sampling rate was still observable as RPM increased, but to a much lesser extent, as seen in Figures 4.10 – 4.12. Figure 4.10 demonstrates the implementation of the selected span-three filter for the output signal of a Hall effect sensor mounted above an FeAl patch spinning at 500 RPM with ~75 in-lb applied to the shaft, while Figures 4.11 and 4.12 depict the same filter at speeds of 1000 RPM and 2000 RPM respectively.

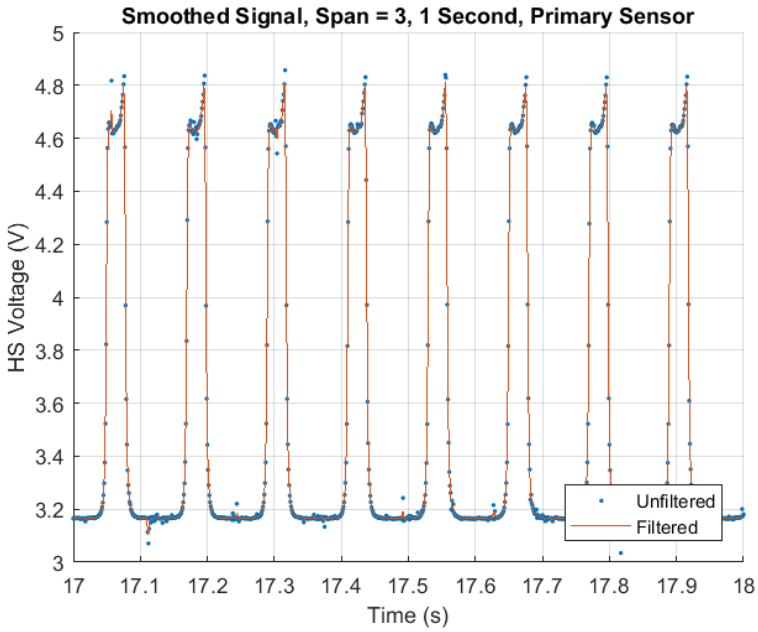

Figure 4.10: FeAl at 500RPM produced filtered peaks ~30mV less than the maximum raw recorded values.

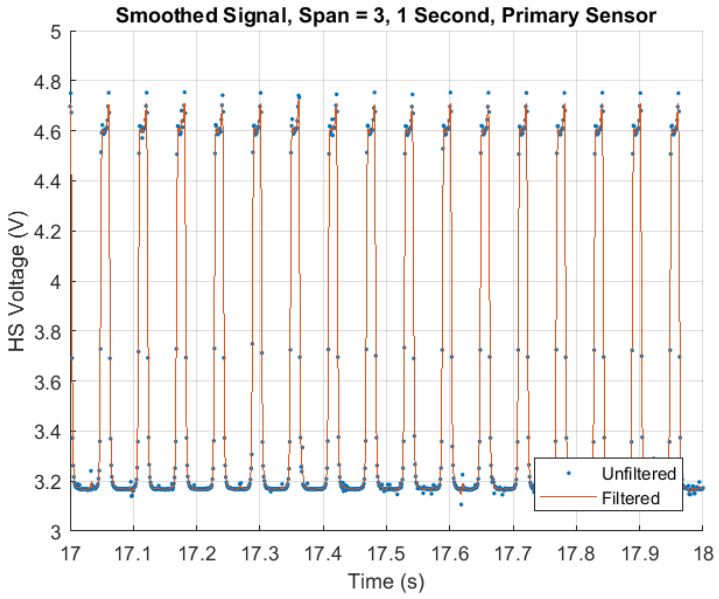

Figure 4.11: A span-three moving average filter was applied to the raw Hall effect sensor data to eliminate outliers and provide an estimate for a mean peak value for each rotation, here tested at 1000 RPM.

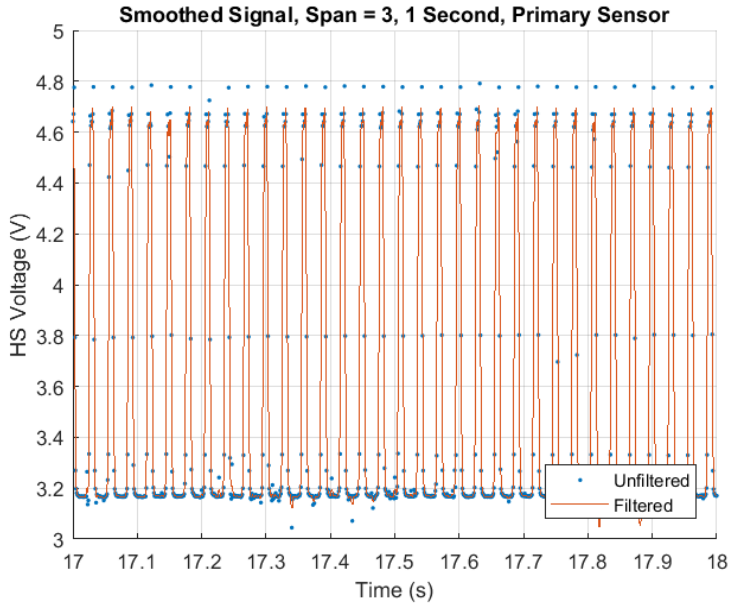

Figure 4.12: FeAl at 2000 RPM produced filtered peaks ~80mV less than the maximum raw recorded values.

In Figure 4.11, at 1000 RPM, the moving average does a good job of capturing peak response. In Figure 4.12, at 2000 RPM, the moving average decreases the evaluated peak response by ~80 mV (the difference between the peak blue dots and the peak red trace values). As each patch coved a smaller percentage of the circumference of the shaft than a ring, few data points existed per pass of a patch under the Hall effect sensor than per pass of a ring under the sensor. This can be seen in Figure 4.10 for an FeAl Patch and in Figure 4.13 for an FeAl ring.

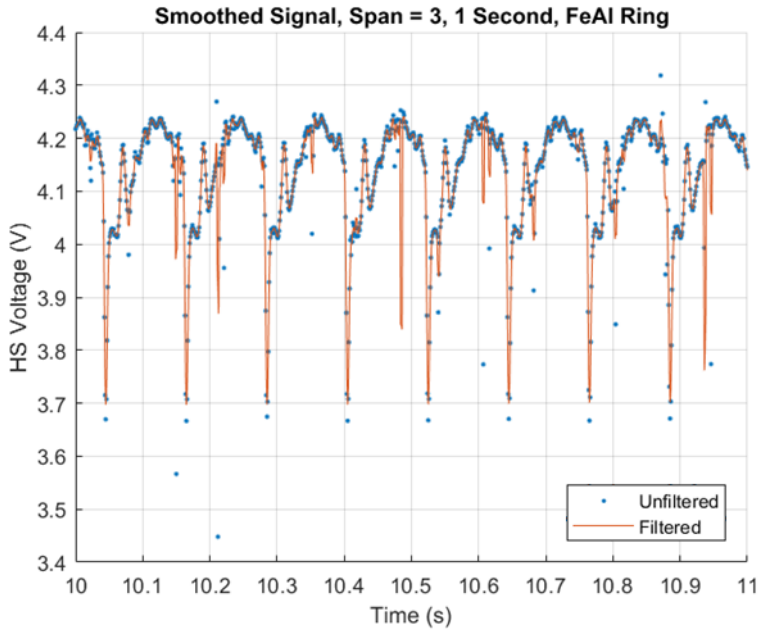

Figure 4.13: Each FeAl ring covers the majority of the circumference of the shaft, such that the troughs represent a sliver of aluminum passing under the Hall effect sensor, shown here at 500 RPM with a 1000 Hz sampling rate.

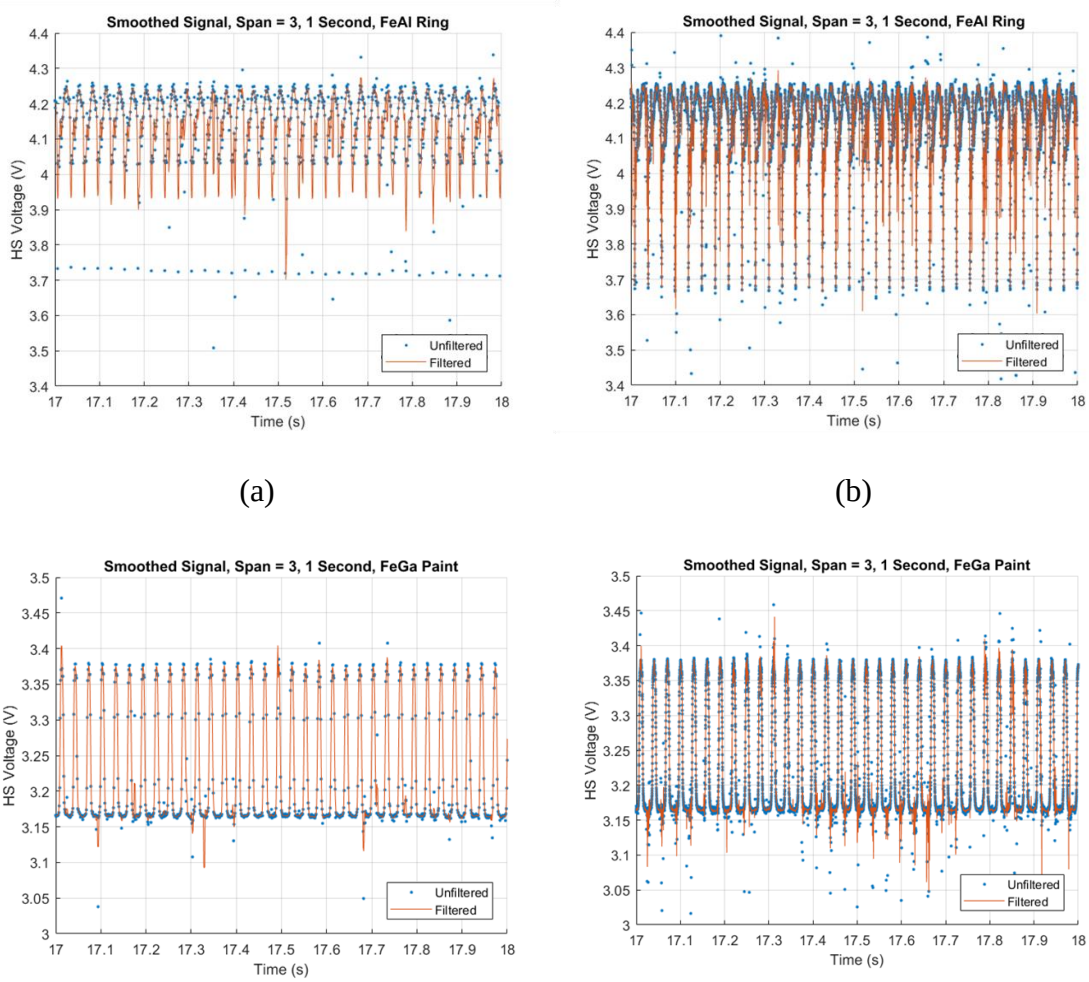

Figure 4.14: Peak FeAl Ring output experiences minimal reduction in response due to the implementation of a span-three moving average filter at a speed of 2000 RPM and a sampling rate of (a) 1000 Hz and (b) no reduction at 10000 Hz. Peak signal for a FeGa paint sample experiences minimal reduction due to implementation of a moving average filter at a sampling rate of (c) 1000 Hz and (d) no reduction at 10000 Hz.

It is worth noting that the reduction in signal due to the implementation of the moving average filter was observed in the FeGa and FeAl Patch samples, but not to the same degree for the FeAl Ring samples. As seen in Figure 4.14 (a), minimal reduction in

peak signal is noted for the ring, even at 2000 RPM. Compare this to Figure 4.12, which depicts a signal reduction of ~80 mV for an FeAl patch sample at the same speed and sampling rate for the FeAl patch.

4.2.2.2 Effect of Sampling Rate on Response

It is suggested that future testing be conducted using a higher sampling rate in order to eliminate the moving average filter as a potential source of variation in sensor response. As seen in Figure 4.14 (b) and (d), sampling at a rate of 10000 Hz provides a much denser distribution of samples with no measurable loss in peak response. However, it is likely that the span of the moving average filter would need to be increased to eliminate additional outliers present in this data set. As such, it is recommended that filtering methods be more rigorously studied in future tests.

4.2.2.3 Data Collection

Each collection of maxima data points in Figures 4.10 – 4.14 corresponded to a single pass of a magnetostrictive patch under the Hall effect sensor per rotation, while every trough corresponded to a period when the aluminum shaft passed beneath the Hall effect sensor. As seen in Figure 4.13, the Hall effect sensor peak signal typically took between 1 and 5 seconds to settle after the beginning of dynamic operation, so only data points from the second half of the ten-second test period (between 0:15 and 0:20 seconds) were used in determining the average peak signal.

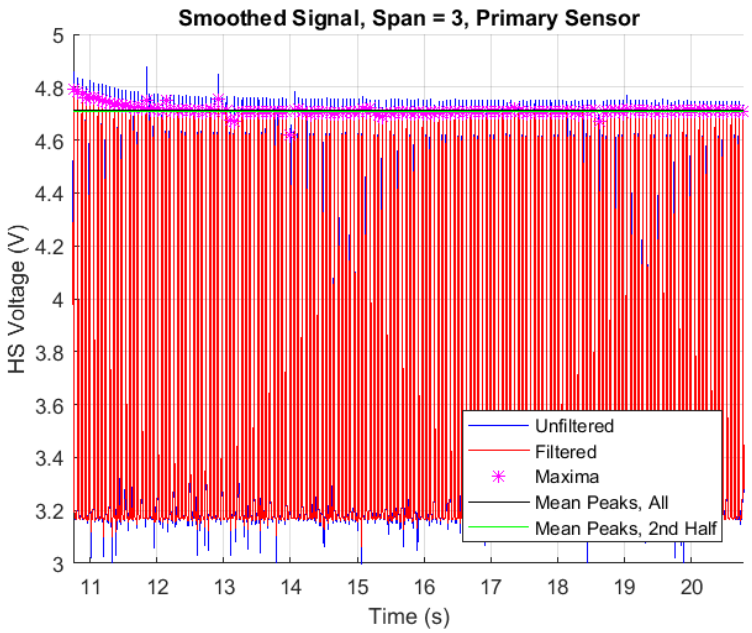

Figure 4.15: A maximum Hall effect sensor value was calculated for each rotation, and the results from the last 5 seconds were averaged to generate a "Mean Peak Signal."

4.2.3 Results and Discussion

4.2.3.1 Shaft Measurements

Two Hall effect sensors were mounted directly above the aluminum shaft in order to establish a baseline measurement for comparison with readings taken over magnetostrictive sensing elements as seen in Figure 4.16. An increase of ~10mV was noted between minimum and maximum torque application at 1000 RPM for both sensors, and signal increased non-linearly until application of ~100 in-lb, after which minimal change in signal occurred.

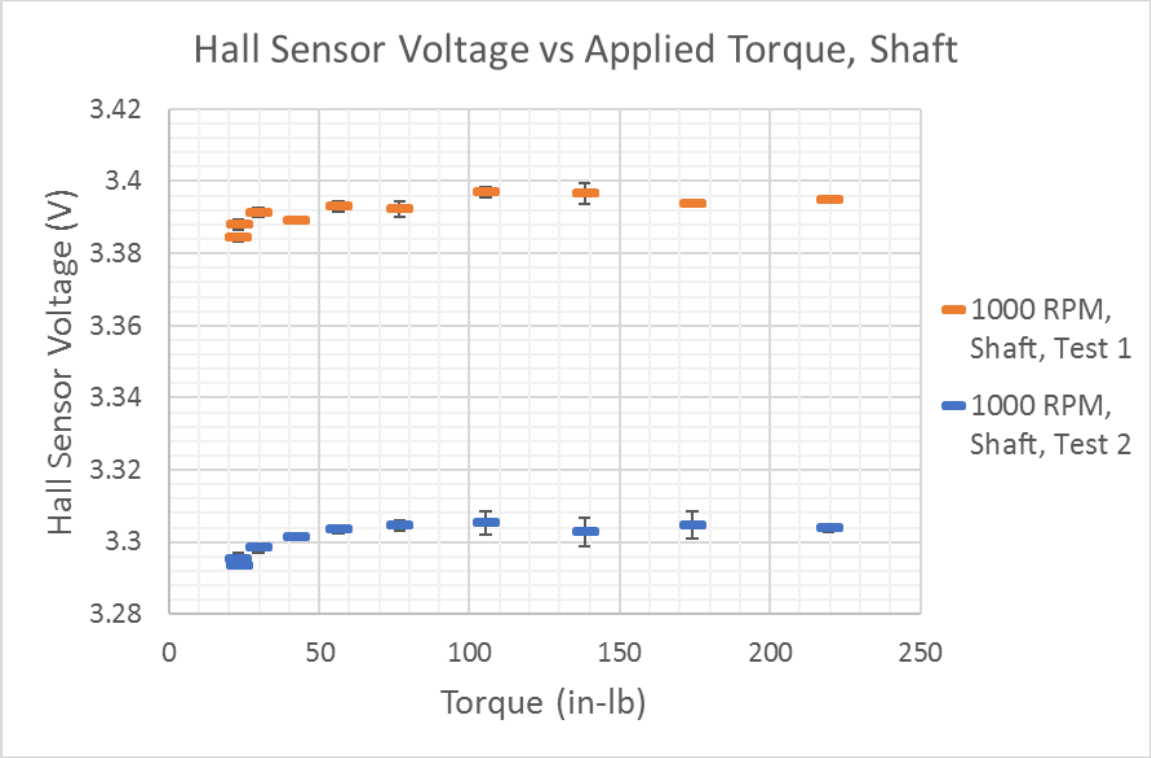

Figure 4.16: Hall sensors mounted directly over the aluminum shaft measured an increase of ~10mV between minimum and maximum torque application.

4.2.3.2 Repeatability

Each sample was tested at 1000 RPM over a range of applied torques between ~22 in-lb – 220 in-lb to provide definition to the Hall effect sensor output voltage curve of each material and to evaluate the repeatability of signal acquisition using different two WiMET sensors as seen in Figures 4.17 - 4.20.

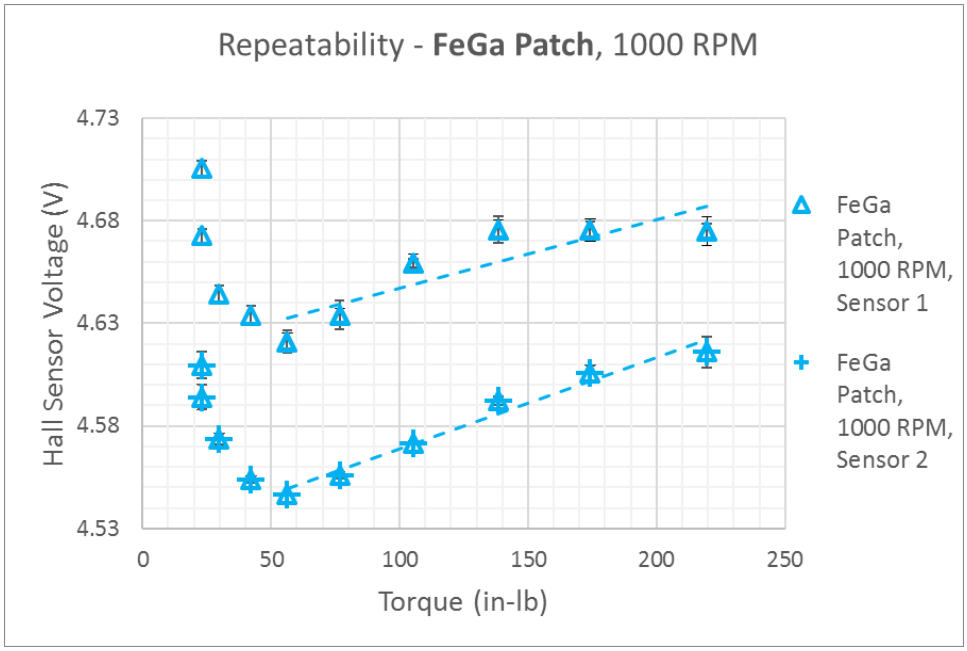

Figure 4.17: Similar responses were observed in the FeGa Patch sample for loads > ~55 in-lb as measured by two separate WiMET sensors.

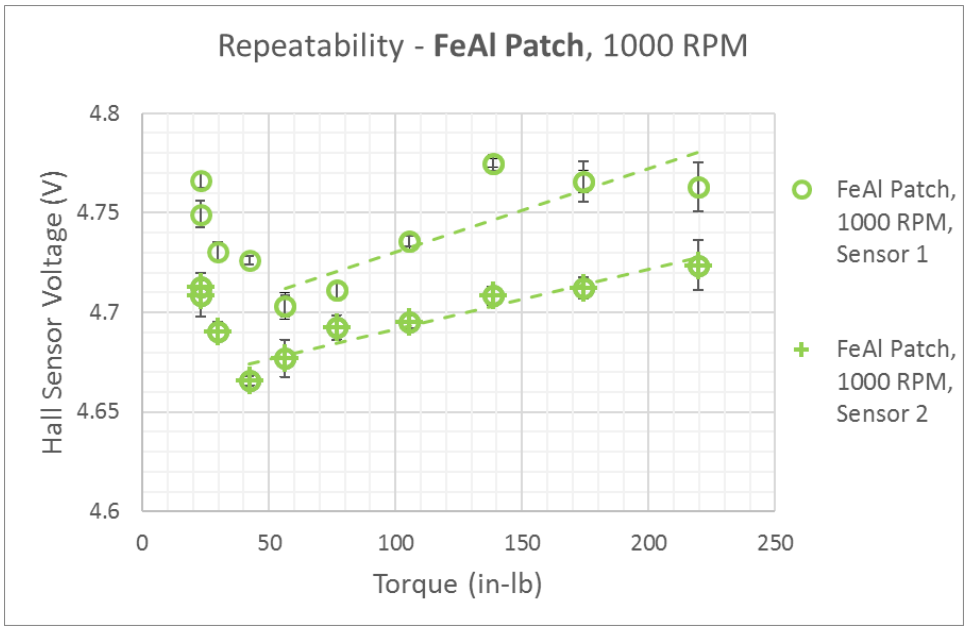

Figure 4.18: Similar responses were observed in the FeAl Patch sample for loads > ~50 in-lb as measured by two separate WiMET sensors.

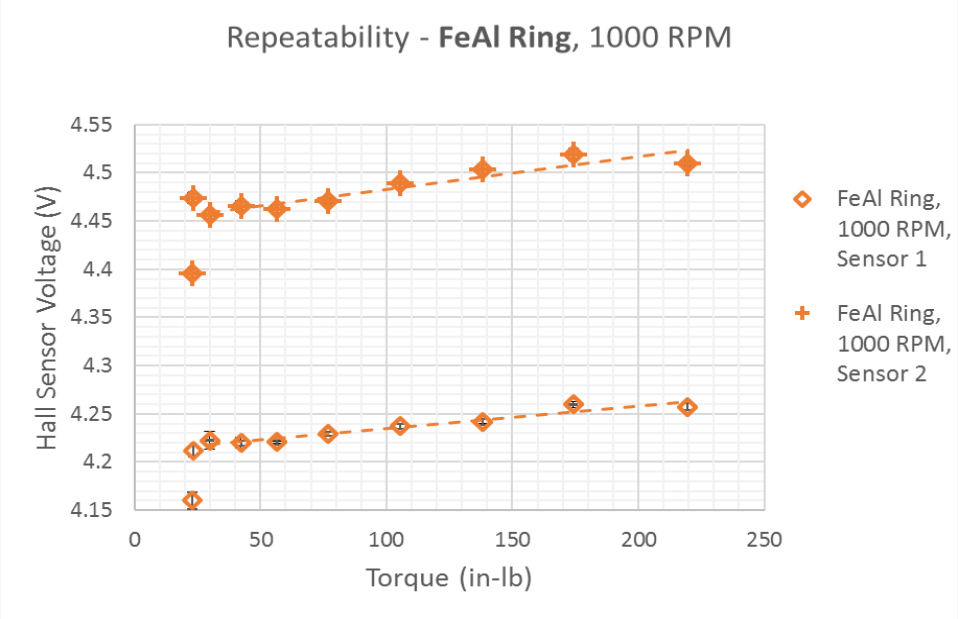

Figure 4.19: Similar responses were observed in FeAl Ring 1 for loads > ~40 in-lb as measured by two separate WiMET sensors.

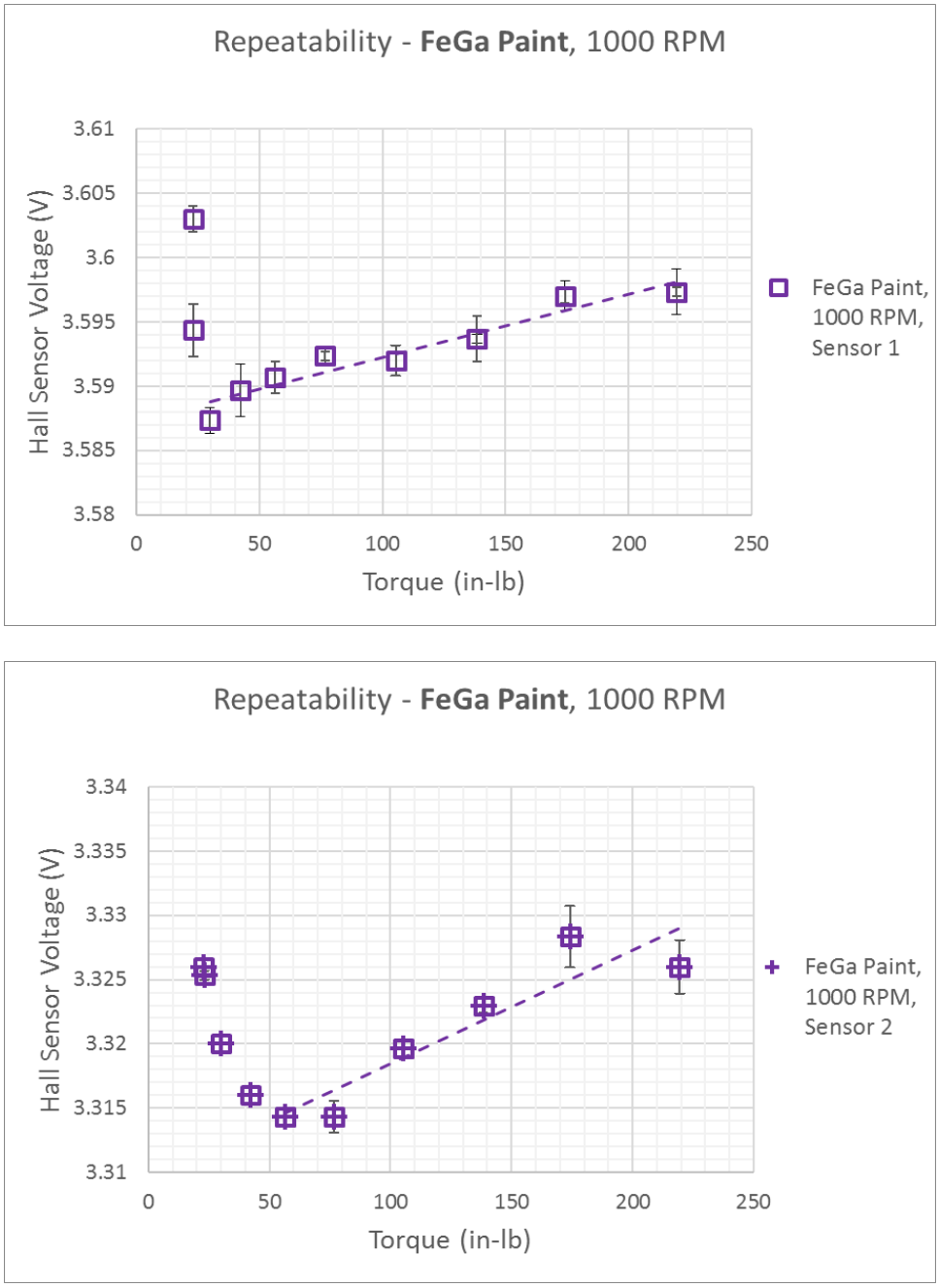

Figure 4.20: Slightly different responses were observed in the FeGa Paint sample for loads > ~50 in-lb as measured by two separate WiMET sensors.

Across all four cases, the outputs of both sensors exhibited similar overall trends in response across the entire range of applied torques for each material. The differences in magnitude between the two responses of Sensors 1 and 2 as seen in Figures 4.17 – 4.20 were due to slight variations in DC bias and position between the two sensors. A slight discrepancy in response of the FeAl patch was noted at ~140 in-lb, but otherwise an increase in signal was observed across applied loads between ~50-220 in-lb. The FeGa patch output signal for Sensor 1 exhibited a slight leveling-off of response for torsional loads in excess of ~140 in-lb, but Sensor 2 provided an increase in signal between ~50 and 220 in-lb. FeGa paint data in Figure 4.20, depicted a noticeable decrease in signal below ~50 in-lb, which is comparable to the response of the similarly-shaped FeGa and FeGa patches, but the slope of the trendlin in the bottom plot is noticeably higher than that of the top plot. Unlike patch-shaped samples, in Figure 4.19 output from the sensors measuring the FeAl rings exhibited a sharp initial increase in signal, followed by a region of linearly increasing response. The dynamic response of each sample is summarized in Table 4.4 considering the change in signal produced by each element before and after the point where response changes from increasing with torque to decreasing with torque, or vice versa.

Table 4.4: Dynamic Response at 1000 RPM

Sample	Hall Effect Sensor	Shape	Initial Decrease?	Inflection Point (in-lb)	Signal Δ Before Inflection (mV)	Signal Δ After Inflection (mV)
FeAl Patch	1	Square	Yes	56	-63	60
	2			42	-47	58
FeGa Patch	1	Square	Yes	56	-84	53
	2			56	-64	70
FeGa Paint	1	Square	Yes	30	-16	10
	2			56	-12	12
FeAl Ring	1	Ring	No	56	65	50
	2			56	60	60
Shaft	1	Ring	No	75	10	0
	2			75	10	0

4.2.3.3 Effect of Rotation Direction

The effect of bi-directional torsional loading on sensor response was evaluated for each sample, as seen in Figures 4.21 – 4.24. In all four cases, a variation in response was noted depending on the direction of rotation.

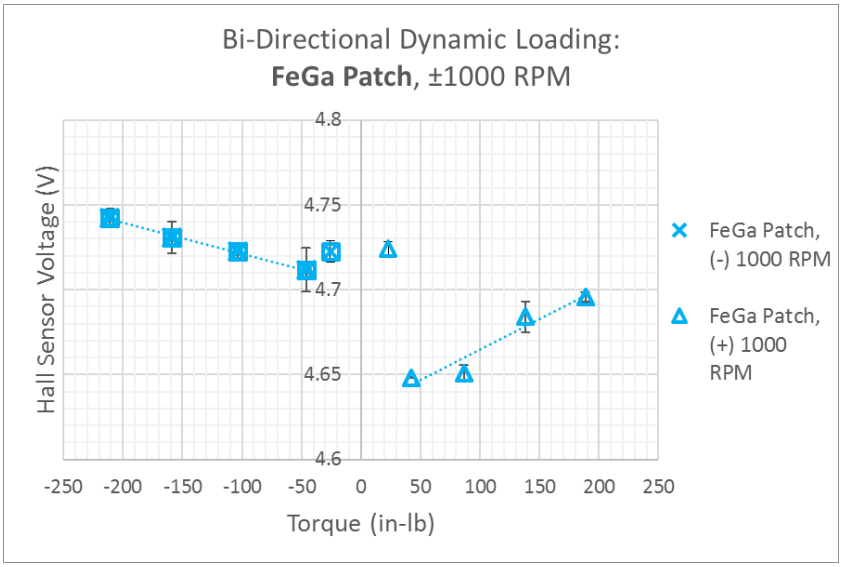

Figure 4.21: A higher sloped trendline was observed under positive rotation than under negative rotation for the FeGa Patch.

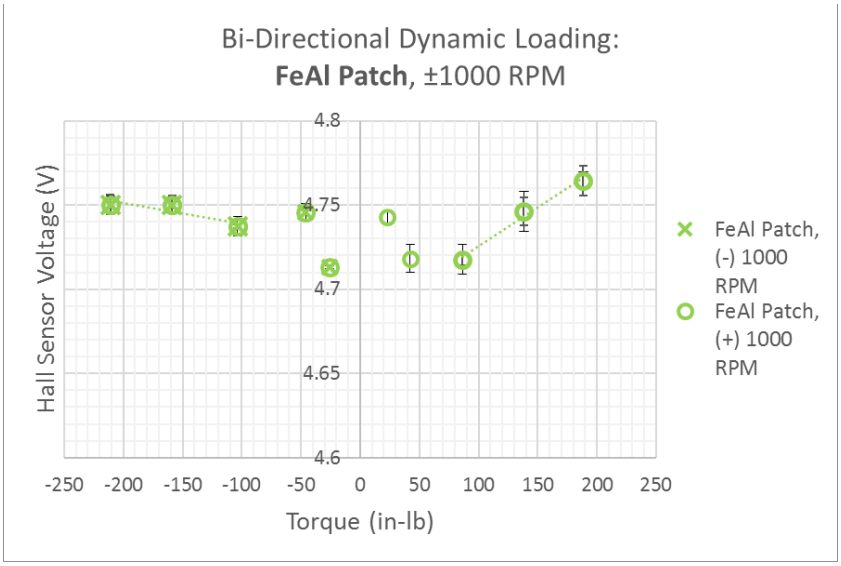

Figure 4.22: A higher sloped trendline was observed under positive rotation than under negative rotation for the FeAl Patch.

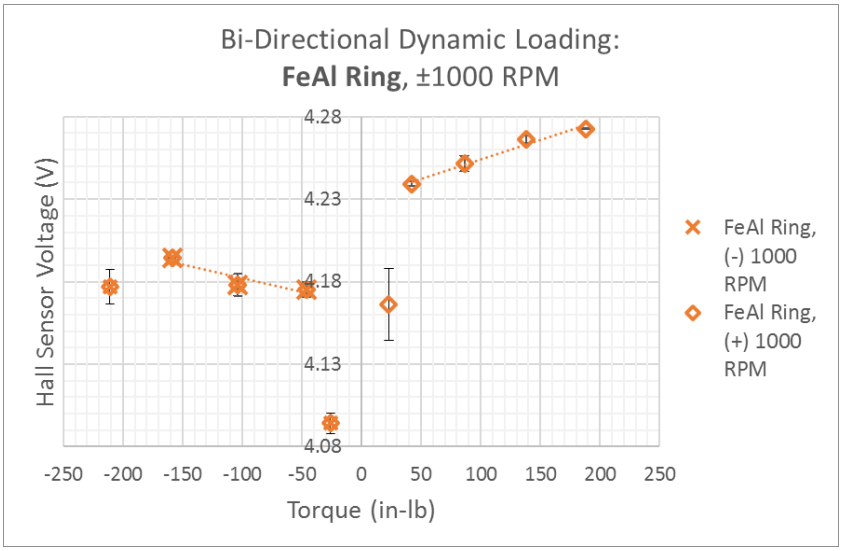

Figure 4.23: A higher sloped trendline was observed under positive rotation than under negative rotation for the FeAl Ring.

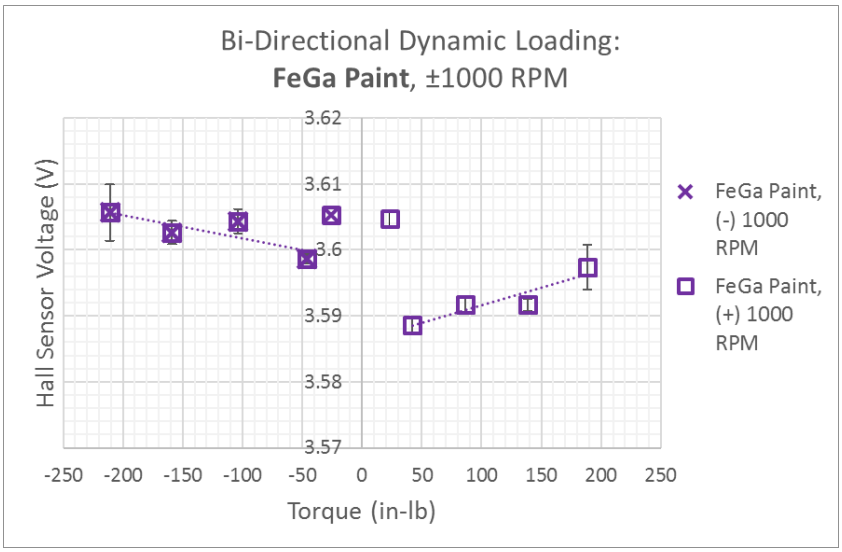

Figure 4.24: A higher sloped trendline was observed under positive rotation than under negative rotation for the FeGa Paint.

Unexpectedly, the FeAl patch offered a different bi-directional response for applied torque < ~±50 in-lb. Upon application of positive torsional loading between 0 and 50 in-lb, the FeAl patch output signal decreased, as previously observed in Figure 4.22, but upon application of the same loads during negative rotation, the output signal of the FeAl patch increased. Additionally, the magnitude of the response of the FeAl patch differed depending on the direction of torque application, as the Hall effect sensor output signal increased by ~50 mV between application of ~40 – 190 in-lb during positive rotation, while the sensor only exhibited an increase of ~10 mV during negative rotation between ~50 – 210 in-lb.

The FeGa patch responded with a distinct decrease in torque between 0 and ±50 in-lb before signal began to increase as applied torque increased in either direction. The FeGa patch provided a slightly different response depending on rotation direction with a ~50mV increase between 40 – 190 in-lb for positive rotation and a ~30mV increase between 50 – 210 in-lb during negative rotation. The FeAl ring offered the most consistent bi-directional response, providing a sharp increase in signal between ~ 0 – 50 in-lb and an approximately linear increase in signal of ~20mV over the remainder of applied torques for both directions of rotation. The FeGa paint exhibited a limited but consistent bi-directional response, providing a ~10 mV increase in signal between applied loads of ~±50 and ±200 in-lb.

4.2.3.4 Effects of RPM Variation

Each sample was tested at 0, 500, 1000, 1500, and 2000 RPM as seen in Figures 4.25 – 4.29. The “0 RPM” cases are static testing results taken from Section 4.1, and are included here to demonstrate a similar increase in signal as applied torque is increased.

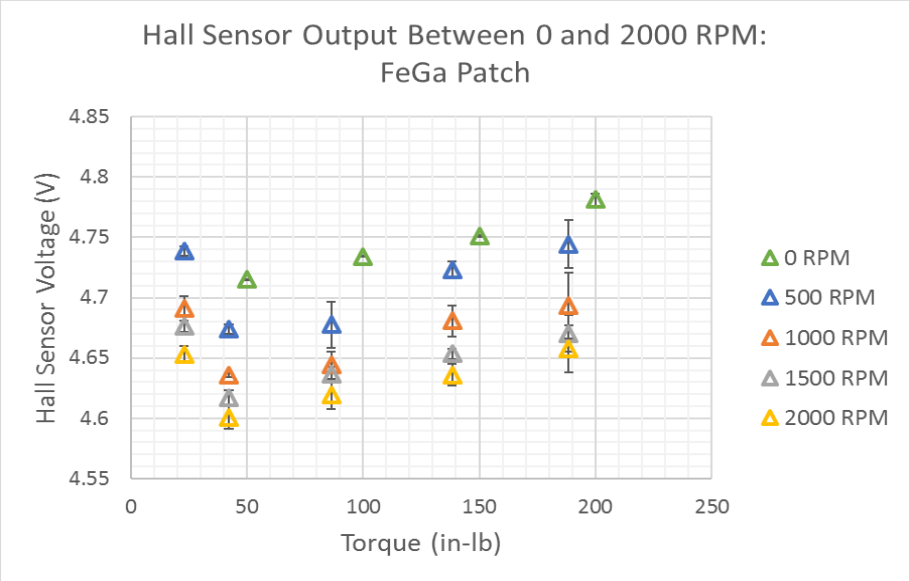

Figure 4.25: Hall effect sensor output (V) decreased at low torque application, but increased in a linear fashion for torques in excess of 50 in-lb for FeGa samples.

Here in Figure 4.25 for the FeGa Patch, an initial decrease in signal is noted across all RPMs between ~22 and 42 in-lb, before signal begins to increase until a maximum torque of ~188 in-lb is reached. By applying a linear trendline (see Figure 4.26) to each RPM curve between the point where the slope in the output signal changes sign (positive slope to negative slope or vice versa), an approximation for sensitivity can be made for the dynamic mode as expressed previously in Equation 4.3. This approximation of linear sensitivity can be seen for all samples in Figures 4.26 – 4.29.

$$Sensitivity = \frac{\Delta\ Hall\ Effect\ Sensor\ Signal}{Range\ of\ Applied\ Torque} \tag{4.3}$$

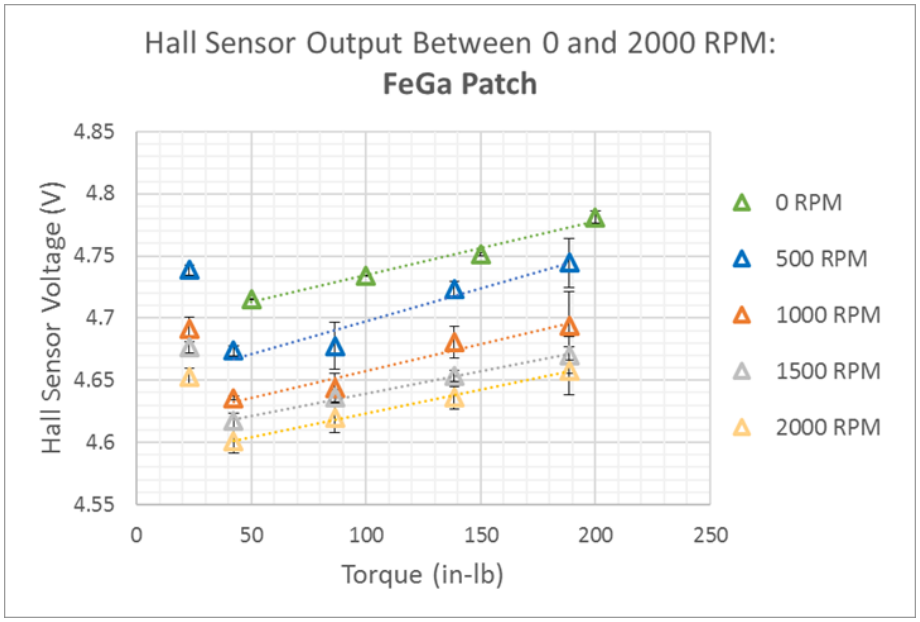

Figure 4.26: Similar sensitivities were observed between 0 – 2000 RPM for the FeGa patch sample

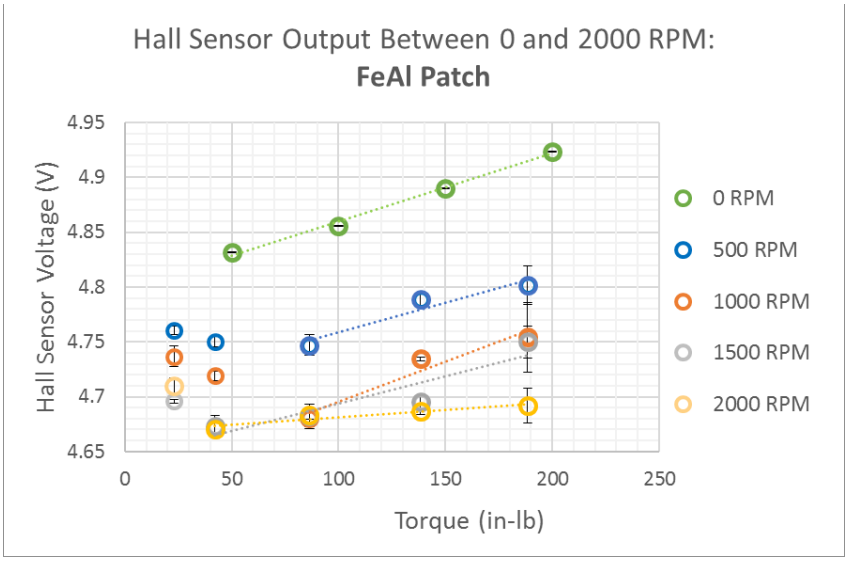

Figure 4.27: Hall effect sensor output (V) decreased at low torque application, but increased in a linear fashion for torques in excess of 50 in-lb with a lower sensitivity response at 2000 RPM than at 0 – 1500 RPM for FeAl samples.

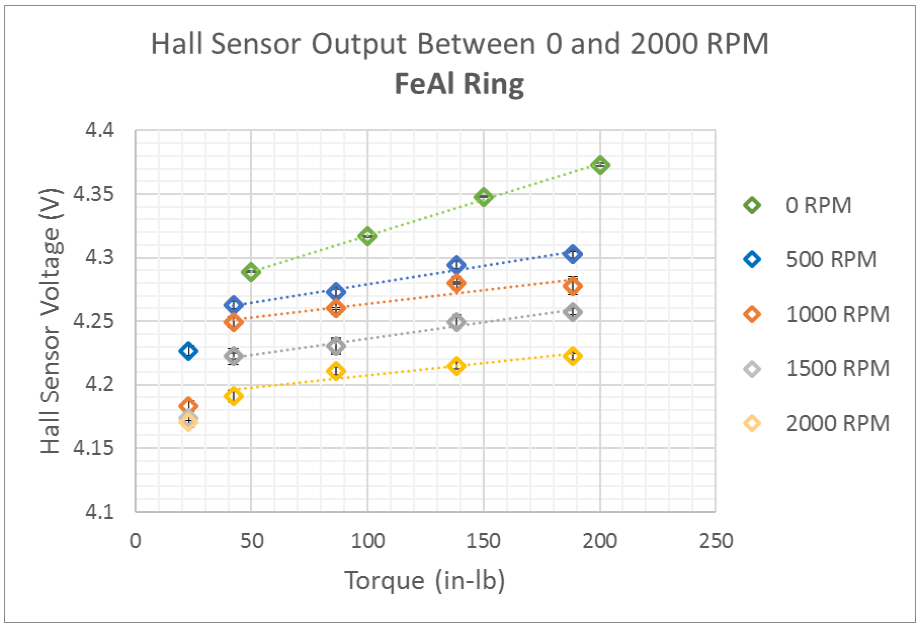

Figure 4.28: Hall effect sensor output voltage (V) increased non-linearly for torques < ~50 in-lb for the FeAl Ring sample and increased linearly for torques > ~50 in-lb with similarly sloped linear trendlines between 500 – 2000 RPM.

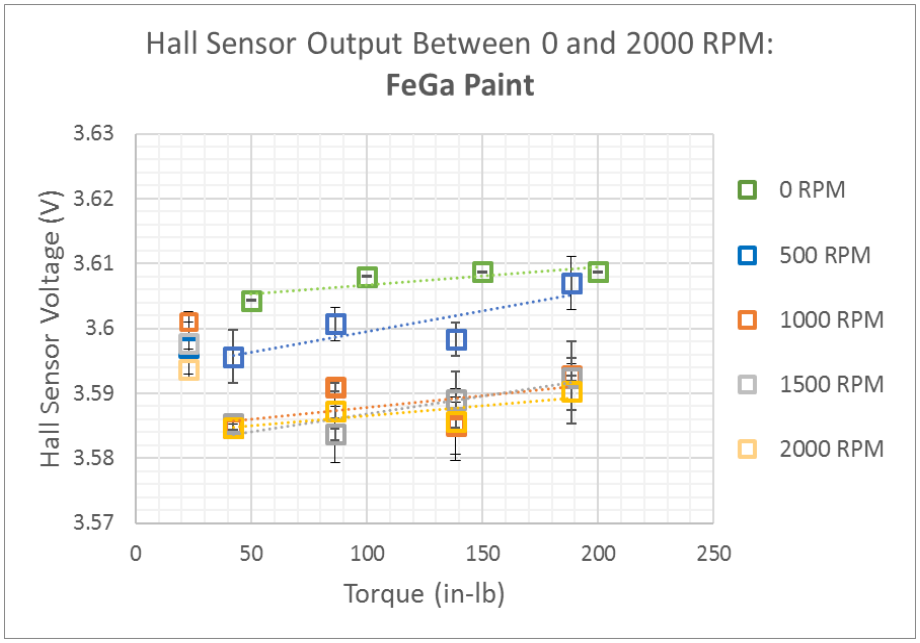

Figure 4.29: Hall effect sensor output voltage (V) increased by a maximum of ~10mV for the FeGa Paint sample as applied torque increased (NOTE: Scale of vertical axis is triple compared with graphs of other samples in this section).

Across all samples, Hall effect sensor signal magnitude decreased as RPM increased. This was due in part to the sampling method described in Section 4.2.2. As RPM increased, fewer data points existed per pass of the patch under the Hall effect sensor, resulting in a lower average signal in high RPM cases, as seen in Figures 4.10 – 4.14. Despite this decrease in signal magnitude as RPM increased, the same general trends were still observable for each sample over the entire range of applied RPMs, suggesting that the magnitude of applied torque and position of the Hall effect sensor primarily affect the magnitude of the response, and RPM shifts the curve depending on how the signal is filtered.

Samples with a square geometry, namely the FeGa and FeAl patches, provided a visible decrease in signal between ~ 0 – 50 in-lb, and demonstrated a fairly linear increase

in output across cases with torque application >50 in-lb, as seen in Figures 4.26 – 4.27. This linear portion of the response suggests that the magnetostrictive patches operated within a linear region of the *B*-σ curves in Figure 1.5 Currently, the reason for a different sign in the slopes below and above ~50 in-lb is not well-understood, although the non-uniformity in response at applied torques < 50 in-lb may potentially be attributed to the unanticipated realignment of magnetic domains within the magnetostrictive material, possibly due to the effects of centripetal loading and/or the initial shear stress causing all moments to align circumferentially with the easy axis of each material. The thought here is the magnetic bias would cause domains to align along the shaft length. The initial shear stress (loads < 50 in-lb) is like the pre-stress used in Figure 1.4 and causes domains to align along the circumferential <100> easy axis, thus producing a reduction in the flux leaking along the axis of the shaft to the Hall effect sensor. As further increases in torque rotate domains toward the 45˚ principle stress axis of the patch, one would expect to see an increase in the component flux leakage along the shaft length being measured by the Hall effect sensor.

An increase of ~50mV was observed for FeAl and FeGa samples within this linear range, while FeGa paint samples provided a maximum increase in signal of ~10mV. While the responses measured over the bare aluminum shaft and over the paint are of the same order of magnitude, it worth noting that the FeGa paint does exhibit a unique response by comparison. The output signal of the FeGa paint decreases for torque <~50in-lb as seen in Figure 4.29 while the background signal observed over the bare aluminum shaft increased over the same range of torques as seen in Figure 4.16.

Unlike the square patches, the FeAl ring sample experienced no initial decrease in signal. Rather, an increase of ~40mV was observed over the entire range of applied torque for the FeAl ring sample, and the signal appeared to increase linearly for torque application >~50 in-lb. Comparing the outputs of the FeAl patch in Figure 4.28 and the FeAl ring in Figure 4.29, it is possible that this difference in performance can be attributed to shape anisotropy effects.

4.2.3.5 Dynamic Sensitivity

As described previously, the sensitivity of each sample was calculated considering the mean increase in Hall effect sensor output between the point in the signal where response shifted from a rapid increase or decrease to a shallow-sloping linear trend and maximum applied torque for each case, as seen in Equation 4.3. These results are summarized in Table 4.5 for test cases evaluated at 500, ±1000, 1500, and 2000 RPM.

Table 4.5: Dynamic Sensitivity of FeGa and FeAl Samples

Sample	Sensitivity (mV/in-lb) RPM Variation					Sensitivity (mV/in-lb) +/- Rotation	
	500	1000	1500	2000	Average	(-1000)	(+1000)
FeGa Patch	0.53	0.43	0.36	0.38	**0.43**	0.18	0.36
FeAl Patch	0.53	0.73	0.5	0.13	**0.47**	0.12	0.46
FeAl Ring 1, 0.1mm	0.29	0.22	0.25	0.20	**0.24**	0.17	0.23
FeGa Paint	0.06	0.04	0.05	0.03	**0.05**	0.04	0.05

The FeAl patch provided the highest average sensitivity for applied loads between ~42 – 188 in-lb and for speeds between 500 – 2000 RPM. The FeGa patch, which has a similar shape, provided similar performance within 91% of FeAl. The FeAl ring provided consistent response across RPMs and directional loading, but provided lower output than the FeAl patch. This difference in response by two samples of similar composition and different shape suggests the effect of shape anisotropy on sensor performance. The FeGa paint exhibited the lowest overall response, but still provided an increasing signal as loads were applied.

4.3 Comparison of Experimental Results and Simulations

Over the course of quasi-static and dynamic testing, sensitivity (considered as an increase in Hall effect sensor voltage as applied load increased) for FeGa was measured between 0.43 – 0.59 mV/in-lb. It must be considered whether assumptions made when modeling sensor performance are consistent with these results.

Assuming no torque greater than 200 in-lb is applied to the shaft, the WiMET sensor should operate along one of the curves to the right of the dotted line in Figure 2.18. The specific curve associated with WiMET operation should depend on magnet strength, magnet position, and Hall effect sensor position in the physical test setup.

Considering the FeGa B-σ curve generated by Atulasimha et al. in Figure 2.18, a sensitivity can be estimated for the WiMET sensor for each applied magnetic field curve presented. By evaluating the magnetic induction at 0 MPa and 10 MPa for each applied field curve, a change in induction over a 10 MPa range can be calculated for each curve. Based on the reduction in flux across the air gap (0.01 in thick) predicted from Figure 2.16,

it can be assumed that the magnetic flux density as measured by the Hall effect sensor will be ~50% of that output by the FeGa.

The Hall effect sensor converts this measured flux to a voltage based on an approximate linear sensitivity of 130 mV/mT, as listed by the manufacturer. Based on modeling results which suggest that a volume maximum compressive stress of ~10 MPa within the FeGa patch corresponds to an applied torque of ~200 in-lb on the shaft, a sensitivity can be estimated in terms of change in Hall effect sensor voltage [mV] over the 200 in-lb range of applied torques, as seen in Table 4.6.

Table 4.6: WiMET sensor sensitivity estimation

Applied Field (Oe)	Induction @ 0 MPa (T)	Approximate Induction @ 10MPa (T)	Δ Induction (mT)	Δ Induction @ Hall Effect Sensor (mT)	Δ Hall Effect Sensor Output (V)	Estimated Sensitivity of Sensor Response (mV/in-lb)
0	0	0	0	0	0	0
22.3	1.5	1	~500	250	32.5	162.5
44.6	1.61	1.54	~70	35	4.55	22.75
66.9	1.63	1.61	~20	10	1.3	6.5
89.1	1.64	1.63	~10	5	0.65	3.25
111	1.65	1.64	~10	5	0.65	3.25
167	1.665	1.66	~5	2.5	0.325	1.625
223	1.685	1.681	~4	2	0.26	**1.3**
446	1.75	1.749	~1	.5	0.065	**0.325**
891	1.85	1.85	0	0	0	0

Considering experimental results (0.43 – 0.59 mV/in-lb) and the estimates summarized in Table 4.6, it is likely that the configuration of the WiMET sensor discussed here operated between the 223 Oe and 446 Oe curves indicated in Figure 4.30, as Table 4.6

provides sensitivity estimates of 0.325 mV/in-lb at 446 Oe and 1.3 mV/in-lb at 223 Oe, which are highlighted on the table.

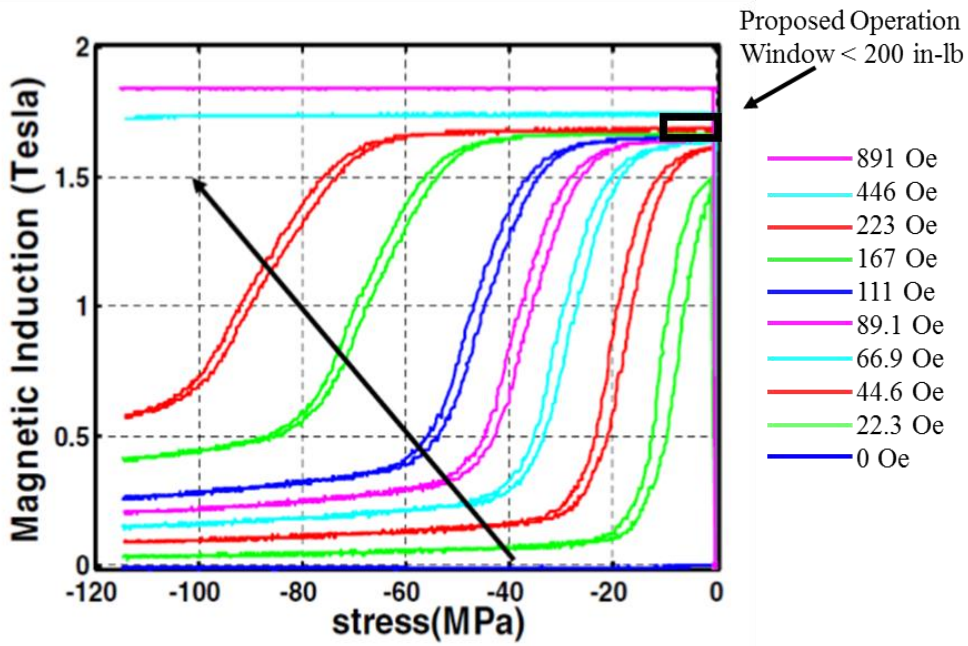

Figure 4.30: This updated WiMET operating window is based on estimates from FeGa sensor curves generated by Atulasimha et al., modeling results from Chapter 2, and testing results from Chapters 3 and 4.

This estimated operating window is consistent with experimental results when considering the particular configuration of sensor elements described in Section 3.3.3, where it is noted that a magnet with a 135 mT surface field is used as a DC bias. In air, 135 mT is ~ 1350 Oe, which upon reaching the surface of the FeGa patch has reduced in strength by 72% based on COMSOL modeling results. This reduction in applied field corresponds to an applied field of ~380 Oe, which is within the predicted range of 223 Oe – 446 Oe in Table 4.6.

As such, Table 4.7 summarizes the quasi-static testing sensitivity and dynamic sensitivity for FeGa determined in Chapter 4, which are equal under positive torsion and within the estimated operating range provided by Table 4.6.

Table 4.7: Sensitivity summary

Sample	Linear Sensitivity Estimate (mV/ft-lb)	BDQS Linear Sensitivity (mV/in-lb)		Average Dynamic Linear Sensitivity (mV/in-lb)
		(-) Rotation	(+) Rotation	
FeGa Patch	0.325 – 1.3	0.59	0.43	0.43

In addition to comparing the current experimental results with simulated performance, in Figure 4.31, the current results are compared to the prototype FeGa WiMET data presented in Figure 1.11. Here, the blue boxes in Figure 4.31 represent the regions of similar operating torques and RPM for the two WiMET sensors.

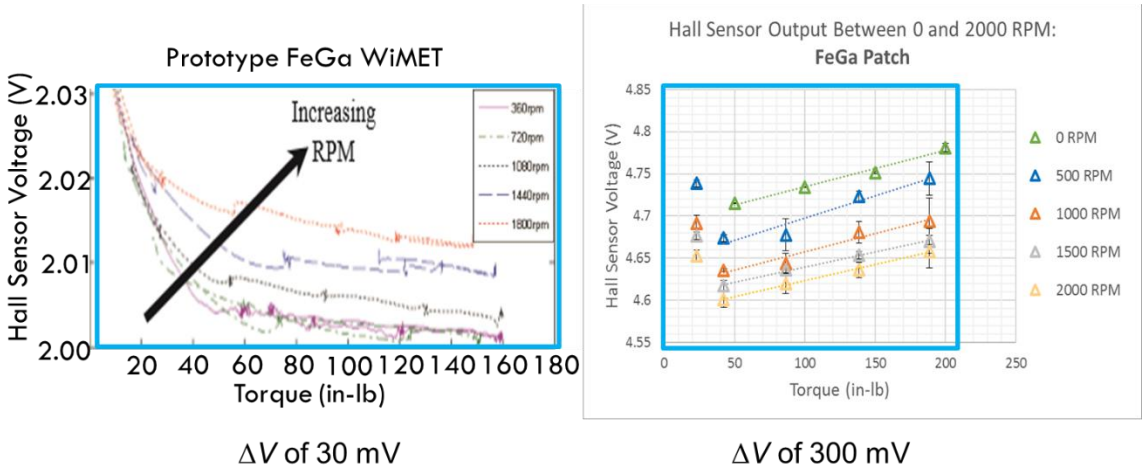

Figure 4.31: The updated WiMET configuration provided an output magnitude and sensitivity ~10 times greater than the prototype between ~ 44 and 188 in-lb.

The prototype sensor (left) and the updated WiMET configuration (right) both exhibited a negative sloping response for applied torque < ~44 in-lb, and both exhibited a linearly varying response as applied torque further increased, though the prototype sensor provided a linearly decreasing response while the updated configuration provided a linearly increasing response. The updated WiMET configuration discussed in this thesis provided an order of magnitude larger sensitivity i.e. output response per unit applied torque, with an observable change in Hall effect sensor voltage ten times that of its predecessor over the same range of applied torque for torques greater than ~50 in-lb. The difference in the order of magnitude or responses, but not the difference in trends between these responses, can be attributed only in part to the difference in standoff distances between the Hall effect sensor and patch in each case (0.01 in for the current work, and 0.1 in for the prior work). The protocol used for bonding of the patch to the shaft, the type of adhesive, and the bias magnet position are the primary differences between these two results that are believed to improve strain transfer from the shaft to the patch, and to improve the bias state of the patch so it is more responsive to the applied torque. The patches used were similar and the bias magnets used were the same. There were also differences in the standoff distance between the Hall effect sensor and the patch and of the position of the bias magnet. These are summarized in Table 4.8.

Table 4.8: Differences in sensor configuration between prototype WiMET and current WiMET configurations

	Magnet Surface Strength (mT)	Magnet Vertical Standoff (in)	Magnet Position above Patch	Hall Effect Sensor Standoff (in)	Adhesive Used
Prototype WiMET	135	0.1	Over Edge	0.1	Crystalbond
Current WiMET	135	0.05	Over Center	0.01	Loctite 648

Chapter 5: Conclusions and Future Work

5.1 Summary of Results

A review of the state of the art in torque sensing technology within the automobile and rotorcraft industries revealed the need for a robust compact system capable of real-time, accurate, and reliable torque measurement from a non-rotating frame of reference for the purposes of system health monitoring, condition-based monitoring, and usage-based monitoring. Recent improvements in the development of rolled sheet magnetostrictive materials have provided the opportunity to develop such a non-contact torque sensor by using a thin magnetostrictive structural element of either Galfenol or Alfenol adhesively-bonded to a drive shaft to measure the changes in the stress-induced magnetic state of said magnetostrictive material.

By considering the results of a mechanics-level analysis of such a system under pure torsion while keeping the piezo-magnetic constitutive equations, it was determined that the principle shear stress and three-dimensional magnetic field applied to the magnetostrictive patch would be primarily responsible for any expected change in magnetic flux density as measured by a nearby Hall effect sensor. The results of a COMSOL multiphysics model confirmed this evaluation by providing insight into the expected leakage of magnetic flux from the WiMET sensor along with estimates for the expected magnitude of the applied stress and magnetic field during bi-directional loading. Though neither expected nor obvious, modeling results predicted a variation in magnetic flux leakage dependent on the direction of load application, which was likely an incorrect estimate, as the modules governing structural mechanics and applied magnetic fields were not coupled, and as such a bi-directional difference in response should not have occurred.

Considering these modeling results, an operating window was proposed for the WiMET sensor such that when the FeGa sample experienced a maximum stress of ~10 MPa during a 200 in-lb applied torque, it was expected to provide a response along one of the B-σ curves experimentally generated by Atulasimha et al. depending on the magnitude of the magnetic field applied to the material by the DC bias magnet mounted nearby.

Preliminary BDQS testing demonstrated a consistent increase in sensor output as applied torque was increased for all tested materials. FeGa Patch 1 Edge (a) and Patch 2 Edge (a) exhibited similar bi-directional response, as the measured edge of each sample had a circumferentially-oriented <100> crystallographic axis, and a distinct difference in response was observed between the FeGa Patches and the FeAl ring samples, suggesting that shape anisotropy played a role in sensor output. The refined adhesive bonding method highlighted the importance of careful shaping of material during production, consistent sample preparation between tests to ensure repeatable results, and uniform compression during curing to ensure formation of uniform bond layers. BDQS testing conducted with samples applied using the refined bonding protocol provided signal output that was increased by a factor of two to three when compared to preliminary results.

Overall, the FeAl Patch proved to be a promising magnetostrictive sensing element, as it provided higher sensitivity than the FeGa Patch and observed the lowest overall drift between bi-directionally applied torques of up to 200 in-lb. FeGa provided a comparable, but slightly lower, sensitivity and maximum signal, and it exhibited lower sensitivity to positive torsional loading than negative loading. The 0.15 mm thick FeAl ring provided output magnitudes comparable to those of the FeAl patch, and it exhibited more consistent bi-directional response than the 0.1 mm thick FeAl ring. Overall, signal drift as a percent

of signal mean varied on a case to case basis, but with a few exceptions it remained below 2.5% when considered over short periods of time.

Repeatability of signal acquisition was demonstrated in the dynamic mode using two separate WiMET sensors to evaluate the response of four magnetostrictive samples between 0 – 220 in-lb at 1000 RPM. Over a series of bi-directional tests at 1000 RPM, variation in sensor performance was noted depending on the direction of rotation for every sample. Dynamic testing between 500 and 2000 RPM demonstrated a decrease in sensor output as RPM increased, however this decrease may have been an artifact of the digital sampling rate used in the study and the span-three moving average filter that was used to smooth data. This decrease in sensitivity as RPM increased was not observed during dynamic operation for FeGa by Raghunath et al. [35]. The Hall effect sensors which measured the square FeAl and FeGa patches provided the greatest overall sensitivity to applied loads between ~50 – 200 in-lb and between 0 – 2000 RPM. The FeAl ring exhibited the most consistent overall bi-directional response, but it offered lower sensitivity than the patches. The FeGa paint provided the lowest overall sensitivity, with an increase in signal of similar magnitude to measurements taken directly over the bare aluminum shaft, but unlike the bare shaft, the paint exhibited the same distinct decreasing and then increasing trend in response to increasing applied torque as was observed in the FeAl and FeGa square patches.

Table 5.1: Comparing modeling, quasi-static, and dynamic results

Sample	COMSOL Linear Sensitivity Estimate (mV/in-lb)	BDQS Linear Sensitivity (mV/in-lb)		Dynamic Linear Sensitivity (mV/ft-lb)
		(-) Rotation	(+) Rotation	
FeGa Patch	0.325 – 1.3	0.59	0.43	0.43
FeAl Patch	-	0.69	0.62	0.47
FeAl Ring 1	-	0.78	0.57	0.24
FeAl Ring 3	-	0.78	0.67	-
FeGa Paint	-	-	-	0.05
Shaft	0	0	0	0

5.2 Recommendations

Considering these results in the context of future testing, the biggest change in sensitivity should arise from reducing the magnetic bias applied to the magnetostrictive sensing element. As seen in Figure 4.30, the WiMET sensor operated over a narrow range of applied magnetic fields and applied compressive stresses such that magnetic induction of the magnetostrictive material varied on the order of a few mT. By applying a lower magnetic field to the magnetostrictive sensing element, the material could produce a linear change in induction on the order of 1 T over certain ranges of applied compressive stress. However, a change in induction of more than ~19 mT will saturate the Hall effect sensor used in this study at an offset distance of 0.01 in between the sensor and the magnetostrictive element.

For future testing, increasing the distance between the flux piece (with the attached magnet and Hall effect sensor) and magnetostrictive patch should decrease the magnetic

field applied to the patch, and should also decrease the change in magnetic flux detected by the Hall effect sensor. Assuming a sensitivity of 130 mV/mT for the Hall effect sensor, a 5 V saturation voltage, and a 2.5 V output at a 0 mT reading, the sensor currently has a 2.5 V or ±19 mT operating range. By increasing the distance between the sensor and the patch, the magnitude of detectable flux from the edge of the magnetostrictive patch would decrease exponentially, resulting in decreased WiMET sensitivity. However, this would allow for a wider range of torque to be tested before the Hall effect sensor would reach saturation.

As such, it is recommended that future modeling and testing efforts detail how variations to the strength, size, and position of the magnet (and other elements) in the WiMET sensor affect the magnitude of the magnetic field applied to the magnetostrictive sensing element and the magnetic flux density measured by the Hall effect sensor, which in turn govern sensor response over a wide range of bi-directionally applied torques and RPMs. Alternatively, an induction coil wrapped around the flux piece could be implemented to measure stress-induced changes in induction in the magnetostrictive sample rather than the Hall effect sensor. This would effectively eliminate dynamic range limitations imposed on the WiMET sensor by the sensitivity and 5V operating range of the Hall effect sensor, though this option would require even further research and testing.

5.3 Future Work

This section will discuss recommendations for future studies that utilize magnetostrictive materials for similar sensing applications, and it will outline a brief test plan to expand upon and further validate the results presented in this thesis in a more

realistic operating environment at an Army Research Lab facility on-base at Aberdeen Proving Grounds.

5.3.1 Testing in Realistic Operating Conditions

The studies conducted in support of this thesis were undertaken in an effort to characterize the performance of FeGa and FeAl for torque sensing applications in a room temperature environment relatively free of stray magnetic fields. As such, future research in this subject area should look to address the use of this technology in more realistic operating environments.

Final sensor placement, originally depicted in Figure 3.10 (a), featured the Hall effect sensor at a 0.01 in standoff from the right edge of the magnetostrictive sensing element, with the magnet positioned in the center of a flux piece and over the left half of the patch. This provided the most practical way to compare relative signal magnitudes between material samples during quasi-static testing, as a small standoff distance increased the amount measurable magnetic flux from the magnetostrictive sample and provided the highest signal-to-noise ratio. As such, this standoff distance was also used in the dynamic case, where low axial and lateral shaft motion ensured the Hall effect sensor did not come in contact with the shaft or patch. However, a Hall effect sensor used on a drive shaft between gearboxes, such as a shaft between the main transmission and an intermediate or tail gearbox, will require a standoff distance greater than 0.500 in between the shaft and Hall effect sensor due to aircraft flexure and any whirling of the shaft. With the increased standoff distance, signal-to-noise will increase, and the signal will be too low for the Hall effect sensor to accurately measure**.** At this increased distance, it may be necessary to

utilize a stronger magnet to apply the proper magnetic bias to the magnetostrictive sensing element, which runs the risk of saturating the Hall effect sensor [49], [50].

Likewise, additional axial shaft movement from thrust and thermal loads is expected in full-scale systems. Some applications can see axial shaft movement greater than 0.1 in, which may result in an inability of the Hall effect sensor to accurately detect changes in magnetic field brought on by torque application. Utilizing a scheme of multiple Hall effect sensors with proximity pickup for shaft position is one possible solution, and this could be studied as a possible solution to overcome the axial shaft movement issue [50]. Several sets of Hall effect sensors could be positioned along the length of the shaft and around the shaft in 90˚ increments in order to cancel out shaft bending effects and vibrational loading.

Testing thus far has utilized an adhesive to attach the FeGa and FeAl sensing elements to the shaft. However, adhesives can fail over a large number of test cycles resulting in damage to the mechanical system being tested, such as internal Foreign Object Damage within a gearbox or engine depending on the application. Despite the ability to easily apply and remove patches of FeGa and FeAl when using an adhesive, it is recommended that a ring design be utilized with an interface fit in order to protect other components within the system being tested [50].

The effect of temperature variation on sensor performance has been observed below 670˚C, the Curie temperature of FeGa. The stability of the bottom plot in Figure 1.6, which represents change in magnetization, is promising for sensing applications because little change in response is seen over the tested range of temperatures [26]. However, this study

must be expanded to better characterize performance in higher temperature environments that will be present in full-scale drive train systems.

As shaft temperature varies during operation, the hoop stresses within the magnetostrictive sensing elements will vary. The changes in hoop stresses will affect the magnetic properties of the materials, and the resultant strength of magnetic field as measured by the Hall effect sensor. Therefore, modeling efforts and practical experimentation are needed to quantify the effects of changing hoop stresses within the magnetostrictive materials under different temperatures and input stresses [50].

Finally, future testing should include considerations for environmental effects other than temperature, namely electromagnetic interference and the presence of oil or otherwise caustic materials. Some form of shielding will likely be required over the sensor to ensure that stray magnetic fields from nearby components do not interfere with measurements. Meanwhile, it has already been shown that potentially corrosive compounds, such as oil or seawater are detrimental to the mechanical properties of FeGa [28]. In particular, it is recommended that the effect of prolonged exposure to an oily environment on sensor performance be studied in order to evaluate the projected lifetime and potential degradation of sensing capabilities for FeGa and FeAl sensing elements [50].

5.3.2 Proposed Testing with Army Research Lab

The primary goal of performing on-site testing with the support of Army Research Lab at Aberdeen Proving Grounds would be to reproduce and expand testing carried out on the University of Maryland campus over a greater range of RPM and applied torque in order to validate results and gather new data in a more realistic testing environment. Much

like testing carried out at the University of Maryland, testing with ARL would be divided between quasi-static and dynamic testing.

Quasi-static testing at APG would look to validate previously obtained data on an Army drive train. After the precise assembly of a test setup on an Army drive train system, the study would look to test and validate the wireless torque measurement system using a known, square, patch geometry. The same set of previously-conducted bi-directional quasi-static bending tests, as described in Chapters 3 and 4, would be repeated using a modified Blackhawk tail rotor mounted in a stationary configuration as torque is applied to the shaft. These tests would be carried out using FeGa and FeAl sensing elements of different geometry, such as square patches, rectangular patches, and rings.

The sensor package used for these tests would be the same setup described in Section 3.1, and would include a magnetostrictive sensing element, a flux piece, Hall effect sensor, and bias magnet attached to a height gage. An in-line torque sensor provided by ARL would allow measurements in excess of 200 in-lb, and strain gages would be mounted on the shaft and sensing element at ±45˚ with respect to the longitudinal shaft axis in order to validate theoretical predictions for maximum bi-directional surface strain. Using a different biasing magnet, an increased standoff distance between magnet and patch, or a combination of the two, the magnetic field applied to the magnetostrictive sensing element will be lower than that used in tests summarized in Chapters 4 and 5 in order to increase the sensitivity of the WiMET sensor.

As before, Hall effect sensor and commercial torque sensor measurements would be recorded as torque is varied bi-directionally in increments of 50 in-lb up to the rated system torque. Multiple readings would be acquired at each torque level to determine

scatter, drift, and any hysteretic effects. This cycle would be repeated at least 5 times to ensure adequate sample size, and could be repeated additional times depending on signal variability and error magnitude. Results would be further validated by repeating this sequence of tests with a randomized set of torque inputs and by comparing signal magnitude and drift from these tests with tests carried out at the University of Maryland. Magnetostrictive samples would be removed and replaced using the refined adhesive bonding method detailed in Section 3.5.

It is expected that precise torque application would be confirmed by comparing measurements made using the commercial torque sensor and the strain gages mounted on the shaft and magnetostrictve sensing elements for inputs of up to 200 in-lb. To determine and compare adhesive bond strengths, the strain as measured by gages on the shaft and patch could be compared and reduced to determine a relational "strain transfer" for each material case. Hall effect sensor readings and strain gage measurements would be recorded and compared to previous results as parameters such as patch geometry and thickness are varied, such that any hysteretic effects or drift in response could be identified before dynamic testing. By the end of testing, it is expected that sensor operating range, signal to noise ratio, and sensitivity and calibration factors would be determined for each magnetostrictive sample.

Dynamic testing would proceed in a manner similar to the method explained in Chapters 3 and 4. After a precise assembly of the test setup on one of the drive trains available at APG, the sensor system would be tested using multiple magnetostrictive sensing elements at speeds up to 3500RPM with and without a series of mechanical faults,

such as broken bearings or missing teeth on a gear, introduced to the system in an effort to determine the potential of the sensor for fault detection.

Appendix A: EBSD Images of Magnetostrictive Samples

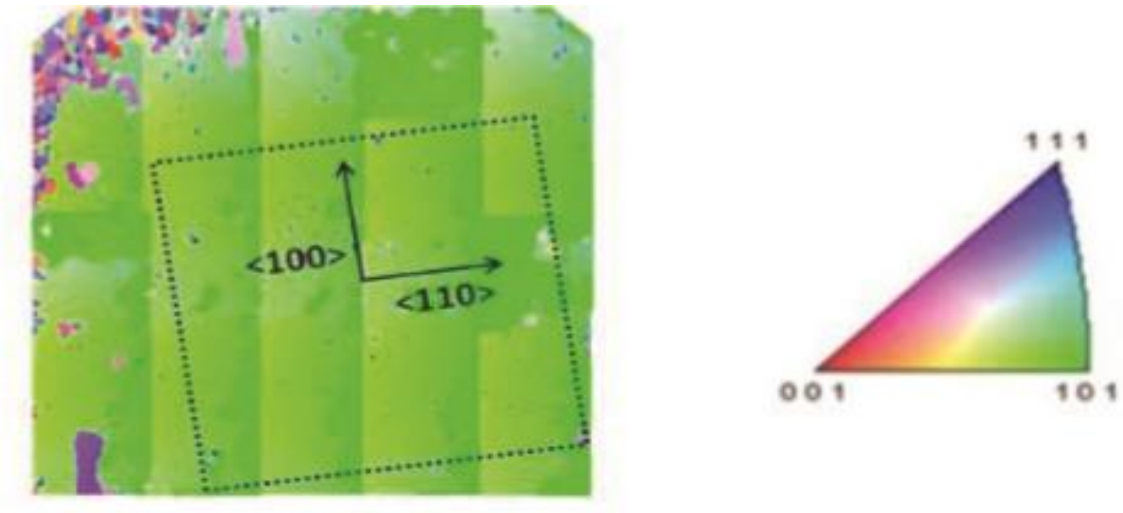

Figure A.1: EBSD-scanned image of a patch of Goss-textured FeGa rolled sheet that was used for the prototype WiMET sensor by Raghunath et al. with a <100> orientation along the length of the shaft [35].

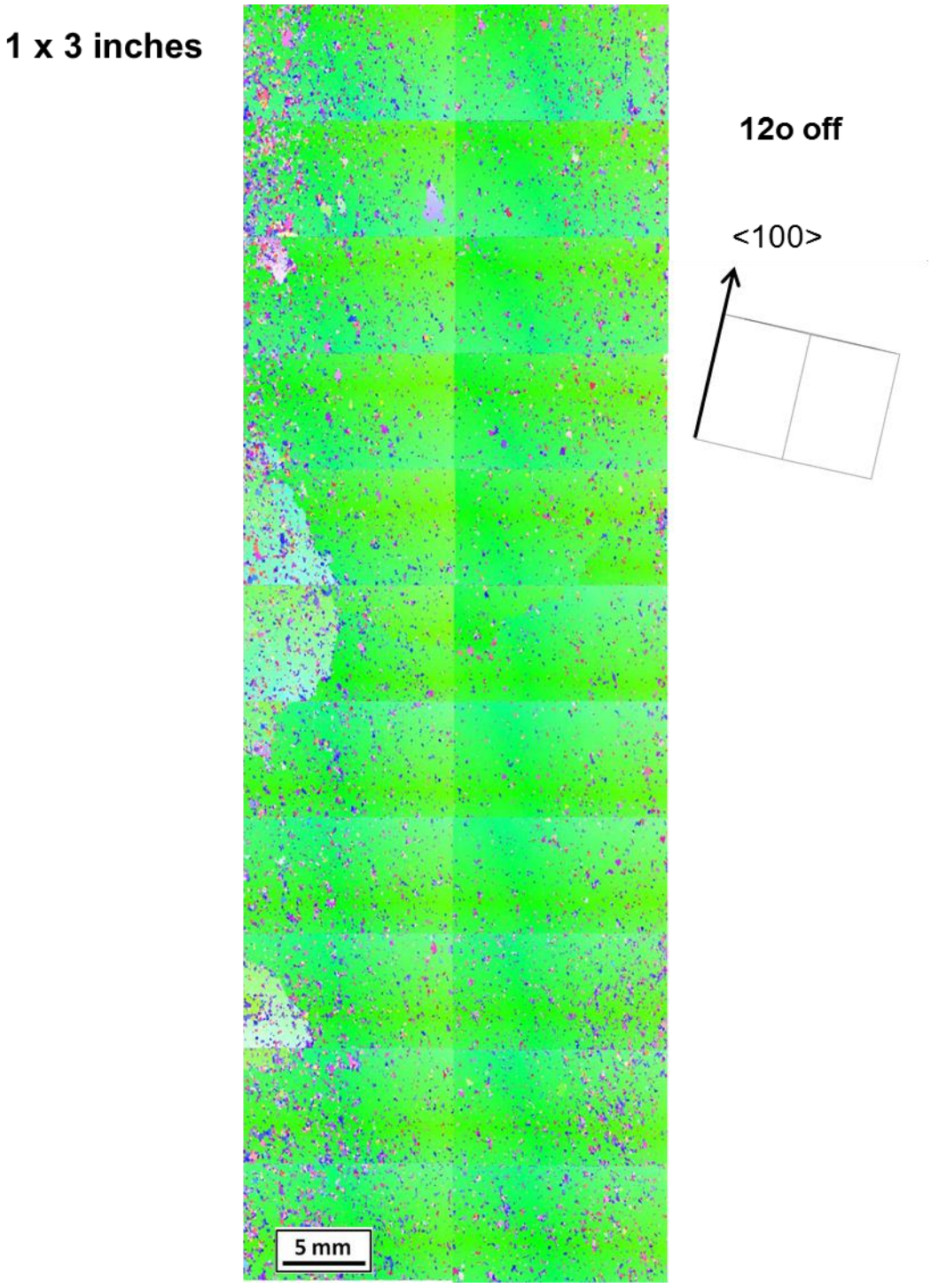

Figure A.2: EBSD-scanned image of FeAl rolled sheet that was used to create "FeAl Patch" sample for WiMET testing with a <100> orientation along the circumference of the shaft.

Appendix B: Modelling Magnetostriction

Equation 2.19, the magnetostrictive sensor equation, can be used to approximate the change in magnetic induction in a magnetostrictive sample considering applied stresses and applied fields. The equation expands as follows:

$$\begin{Bmatrix} B_1 \\ B_2 \\ B_3 \end{Bmatrix} = \begin{bmatrix} d_{11}^* & d_{12}^* & d_{13}^* & d_{14}^* & d_{15}^* & d_{16}^* \\ d_{21}^* & d_{22}^* & d_{23}^* & d_{24}^* & d_{25}^* & d_{26}^* \\ d_{31}^* & d_{32}^* & d_{33}^* & d_{34}^* & d_{35}^* & d_{36}^* \end{bmatrix} \begin{Bmatrix} \sigma_1 \\ \sigma_2 \\ \sigma_3 \\ \tau_{23} \\ \tau_{31} \\ \tau_{12} \end{Bmatrix} + \begin{bmatrix} \mu_{11}^\sigma & \mu_{12}^\sigma & \mu_{13}^\sigma \\ \mu_{21}^\sigma & \mu_{22}^\sigma & \mu_{23}^\sigma \\ \mu_{31}^\sigma & \mu_{32}^\sigma & \mu_{33}^\sigma \end{bmatrix} \begin{Bmatrix} H_1 \\ H_2 \\ H_3 \end{Bmatrix} \quad \text{(B.1)}$$

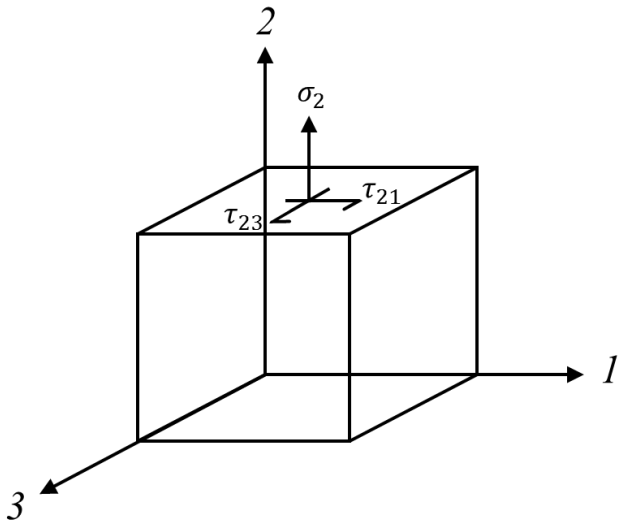

Figure B.1: Axial stress subscripts correspond to the stress orthogonal to a plane, while shear stress subscripts correspond to the stress on a plane in the direction of another axis.

By the convention of the piezomagnetic relations, the *3*-axis is assumed to be the direction of initial magnetization, while axes *1* and *2* are defined in a plane orthogonal to the *3*-axis as part of a conventional right-handed system [2]. Stresses σ and τ [N/m^2] are

representative of axial and shear stresses, and they are denoted by subscripts as shown in Figure B.1.

The proposed WiMET sensor configuration featured a thin curved patch of Goss-textured rolled sheet magnetostrictive material (FeGa or FeAl) mounted to a shaft with its <100> axis oriented along the circumference of the shaft. For the Goss texture, there is only one in-plane <100> axis. Along the length of the shaft, a magnet and a Hall effect sensor were mounted above the magnetostrictive patch in order to form a magnetic circuit, such that magnetic flux lines emanating from the magnet could flow across an air gap, through the magnetostrictive material, across another air gap through a Hall effect sensor, and could return to the magnet via a high permeability magnetic flux piece as seen in Figure B.2. The Hall effect sensor was affixed above an edge of the magnetostrictive patch, and the position of the magnet along the high permeability flux piece was variable.

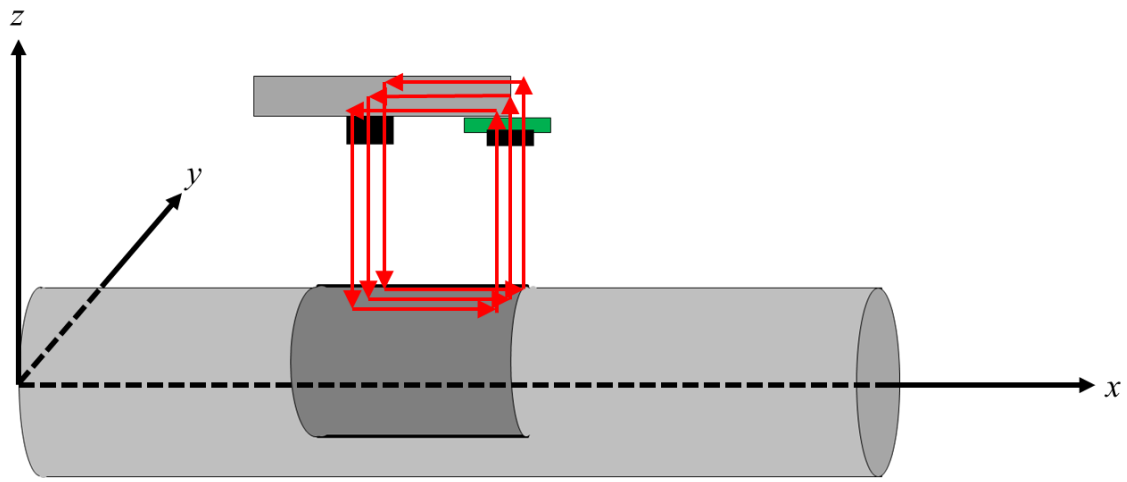

Figure B.2: Magnetic flux lines are expected to travel though the magnetostrictive patch along the axis of the shaft and "leak" through the edge of the material to be detected by a Hall effect sensor mounted above.

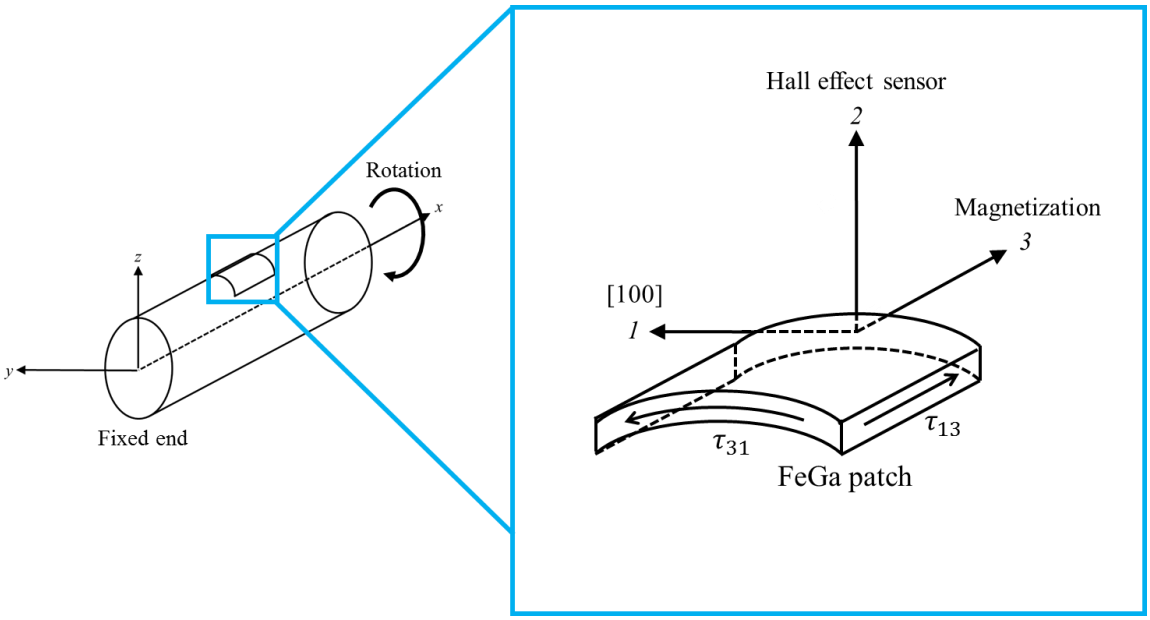

Figure B.3: The FeGa patch experiences shear stress τ across the *1*-face and *3*-face as torsion is applied, and the material is magnetized along the *3*-axis as flux lines travel down the length of the shaft.

When the magnetostrictive patch was positioned atop the shaft, the edge of the sample furthest along the *x*-axis, as shown in Figure B.3, had a <100> crystal orientation along the curvature of the shaft, and the material was magnetized along its *3*-axis as flux lines travel through the length of the patch. Considering the proposed orientation of sensor elements in Figure 2.16, it was assumed that applied field from the biasing magnet and flux density measured by the Hall effect sensor would both be maximal in the *2*-direction and could represented as H_2 and B_2 respectively. The *1*, *2*, and *3*-components of applied field H, H_1, H_2, and H_3 respectively, were all likely to influence measured magnetic flux B in the *1*, *2*, and *3*-directions, B_1, B_2, and B_3 respectively. Given the Mohr's Circle analysis from Section 2.2.1, it was assumed that under ideal conditions of purely torsional loading, no axial stresses would be applied to the rotating shaft, and by extension, the FeGa patch.

Likewise, shear stress was expected to occur only on the *13*-plane and the *31*-plane, eliminating all other shear stress terms. Given these assumptions, the magnetostrictive sensor equation could be simplified to Equation B.2 for instances of quasi-static loading:

$$\begin{Bmatrix} B_1 \\ B_2 \\ B_3 \end{Bmatrix} = \begin{bmatrix} \tau_{31} d_{15}^* + \mu_{11}^\sigma H_1 + \mu_{12}^\sigma H_2 + \mu_{13}^\sigma H_3 \\ \tau_{31} d_{25}^* + \mu_{21}^\sigma H_1 + \mu_{22}^\sigma H_2 + \mu_{23}^\sigma H_3 \\ \tau_{31} d_{35}^* + \mu_{31}^\sigma H_1 + \mu_{32}^\sigma H_2 + \mu_{33}^\sigma H_3 \end{bmatrix} \tag{B.2}$$

As the resultant magnetic flux in the simplified piezo-magnetic sensor equation is determined primarily by the effects of the principal shear stress in a torsionally loaded rod and the components of a three-dimensional applied magnetic field, a full magneto-elastically coupled 3D COMSOL model could be implemented to determine the direction and magnitude of principal stress in the shaft and magnetostrictive sample and to evaluate the *x*, *y*, and *z* magnitudes of the applied magnetic field across the patch as quasi-static torques were applied to the shaft. In order to evaluate the same quantities in the dynamic mode, additional stress terms in Equation B.1 would become relevant, as centripetal loading during high speed rotation would cause a tensile load through the thicknesses of the adhesive layer and of the FeGa patch.

Appendix C: Preliminary BDQS Testing Results

Procedures for BDQS testing, data acquisition, and data analysis are consistent with methods described in Section 3.1.

C.1 Preliminary BDQS Testing

The results of preliminary BDQS testing are summarized in the following histograms, Figures C.1 – C.2, which respectively depict averaged signal magnitude and drift for all samples, and error bars atop each colored bar represent the standard error of the mean $\sigma_{\bar{x}}$ as calculated in Equation 4.1 for each measurement.

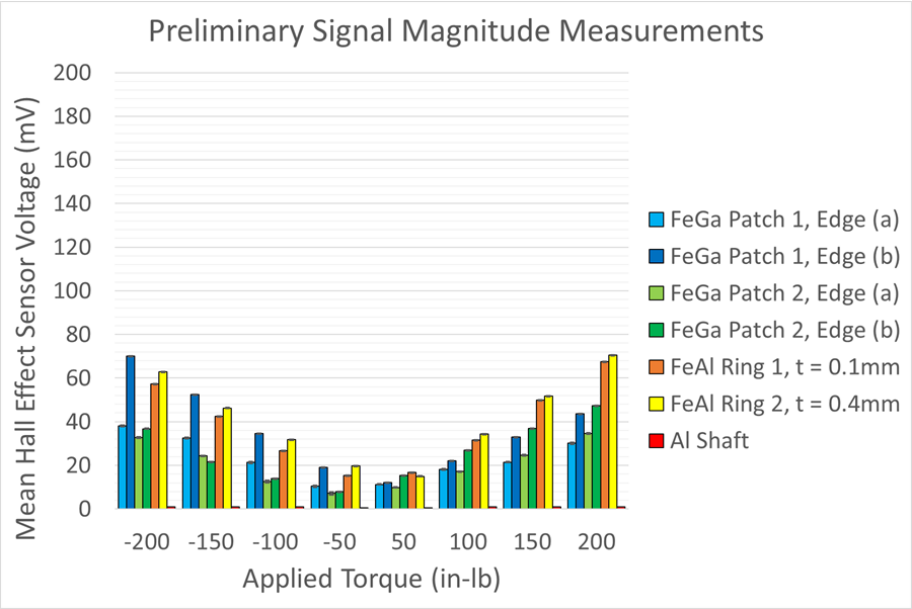

Figure C.1: Hall effect sensor mean voltage output (mV) increased as applied torque (in-lb) increased for each material sample in preliminary BDQS testing. Error bars indicate standard error of the mean.

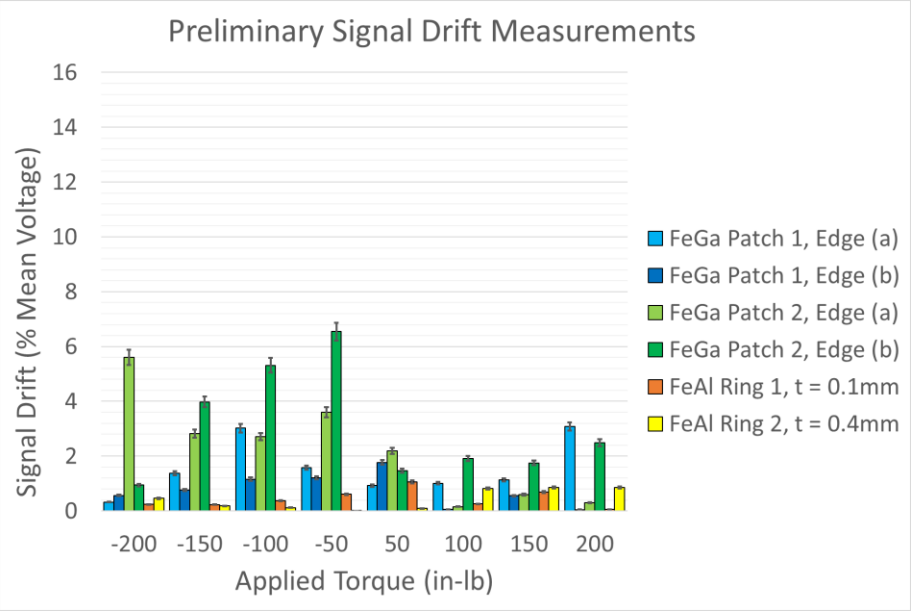

Figure C.2: FeAl samples experienced signal drift < 1% of mean signal over all test cases, while FeGa Patch 2 exhibited drift > 6% under negative torsional loading.

In each case, signal magnitude increased as increasing loads were applied in either direction, as predicted by the piezo-magnetic sensor equation as discussed in Section 2.3.

$$B = d^{*}\sigma + \mu^{\sigma}H \tag{2.19}$$

Assuming the applied field is held constant, the expected response of a magnetostrictive sensor should scale primarily with an increase in applied stress. In this particular case of a rod in torsion, the principal shear stress experienced by the magnetostrictive patch increased as additional torque was applied.

Flux leakage from edge (a) of FeGa patches 1 and 2 offered comparable bi-directional signal magnitude, which was expected considering their similar crystal

orientations. Flux leakage from edge (b) of samples 1 and 2 both experienced a linear increase in output signal as larger positive torques were applied. However, FeGa flux density leakage from edge (b) for sample 1 exhibited vastly greater response than from edge (b) of sample 2 under negative torsion.

The FeAl ring samples provided the consistently highest peak signal output under application of positive torque with a ~70mV signal at 200 in-lb for the 0.4 mm thick ring. As discussed in Section 1.3.4, FeGa and FeAl should offer comparable performance in the sensing mode, so the apparent difference in signal output between FeAl and FeGa samples in this case should be attributed primarily to a difference in sample geometry and the resulting effects of shape anisotropy. Edge (b) of FeGa Patch 1 exhibited greater signal output than the FeAl rings in cases of negative torque application, but did not maintain this performance as positive torques were applied.

In addition to high signal output in both rotation directions, FeAl ring samples experienced drift less than 1% of percent of signal magnitude across all load cases. FeGa Patch 1 exhibited maximum drift of ~3% considering all cases, while FeGa Patch 2 experienced drift in excess of 6% of signal mean across multiple cases. The increased drift in the case of FeGa Patch 2 was most likely due to a combination of low output signal, and a non-uniform adhesive bond layer between the aluminum shaft and FeGa patch. Overall, the FeAl rings exhibited the largest increases in signal and lowest signal drift out of all tested magnetostrictive samples.

C.2 BDQS Testing With Randomized Inputs

In order to validate the results in Section C.1 under more realistic operating conditions, the previous bi-directional quasi-static tests were repeated using a series of randomized inputs. In this section, modifications made to the testing procedure are discussed, along with updated signal magnitude and drift results.

C.2.1 Testing Procedure

These randomized tests evaluated the same six cases as before; one set of tests on each curved edge of two FeGa patches and one set of tests on each of two FeAl ring. Loads were applied in a different manner than before. Rather than applying the same load multiple times in succession, loads were applied in ten second intervals in a random order.

Six strings of nine random numbers were generated using randomizer.org, which offered a suitable degree of randomness for the purpose of this study. The six generated sets included three strings of numbers that were not repeated and three strings of numbers that did not prohibit repetition, as seen in Table C.1.

Table C.1: Randomized number strings used for testing

Interval	**1**	**2**	**3**	**4**	**5**	**6**	**7**	**8**	**9**
Unique	-100	0	-150	50	-200	100	150`	200	-50
	100	200	-50	50	-150	0	150	-100	-200
	150	50	0	-200	-50	-150	-100	200	100
Repeated	150	50	-150	100	100	-50	200	-150	0
	-50	100	100	150	150	-50	-200	100	200
	50	-50	-200	-100	150	-50	50	-200	-50

C.2.2 Results

The results of randomized BDQS testing are summarized in Figures C.3 – C.4 which depict signal magnitude and drift respectively for all six samples. As in Section C.1, Hall sensor output tended to increase as additional torque was applied bi-directionally for all cases. FeGa Patch 1 Edge (a) and Patch 2 Edge (a) exhibited comparable signal magnitude under positive loading, but not under negative loading. Peak bi-directional signal was once more observed in the FeAl ring samples, with the exception of the lowest torque cases.

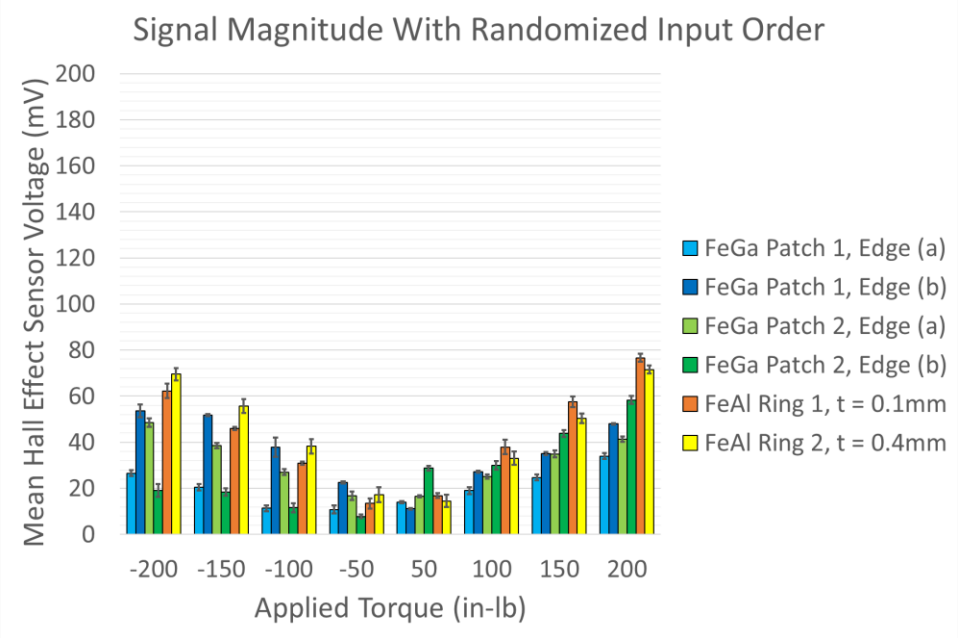

Figure C.3: Hall effect sensor mean voltage output (mV) is plotted against applied torque (in-lb) for randomized-input BDQS testing. Error bars show standard mean error.

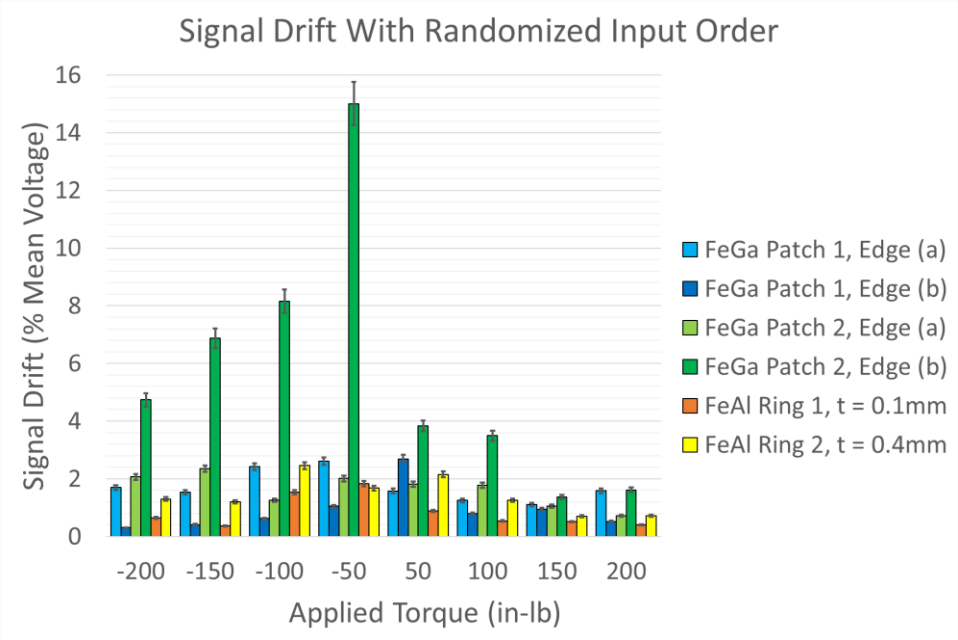

Figure C.4: Hall effect sensor drift (% mean voltage) is plotted against applied torque (in-lb) for randomized BDQS testing.

As shown in Figure C.4, drift as percent of mean signal remained below 5% in all cases except that of FeGa Patch 2 Edge (b), which exhibited a maximum drift of 15% of mean and the lowest signal magnitude observed in this round of testing, ~8 in-lb, when applied a -50 in-lb load. It should be noted that low torque cases (±50 in-lb) tended to exhibit greater drift than cases of greater torque. Because drift was calculated as a percent of the mean signal, a low mean signal such as 8 mV in the +50 in-lb case in Figure C.3 coupled with a magnitudinal drift of 1.2 in-lb resulted in a high mean drift as percent of signal magnitude.

Again, the FeAl rings offered the highest magnitude response and the lowest signal drift across the majority of test cases. The 0.4mm thick ring provided peak signal of about 70 mV bi-directionally, while the 0.1 mm thick ring provided between 60 mV under

negative load and 80 mV under positive load. The signal drift exhibited by the FeAl rings remained less than 3% of mean signal for all cases.

Table C.2 presents the sensitivity of response of the magnetostrictive sensing elements to applied torsional loads before experiments were conducted to refine the adhesive application method, and it assumes operation between 0 and 200 in-lb with linearly increasing signal response.

Table C.2: Sensitivity of magnetostrictive sensing elements before updated bonding protocol.

Sample	**Sample Dimensions (in)**	**Sensitivity (mV/ft-lb)**		**Signal Drift (% Mean)**	
		-	+	-	+
FeGa Patch 1 Edge (a)	0.7 x 0.7	2.5	2.1	1.6	1.5
FeGa Patch 1 Edge (b)	0.7 x 0.7	4.3	2.7	0.9	0.6
FeGa Patch 2 Edge (a)	0.7 x 0.7	1.8	2.1	3.7	0.8
FeGa Patch 2 Edge (b)	0.7 x 0.7	1.9	3.2	4.2	1.9
FeAl Ring, t = 0.1mm	0.75 x 3.14	3.4	4.0	.4	.5
FeAl Ring, t = 0.4mm	0.75 x 3.14	4.0	4.0	.4	1.5

Appendix D: Quasi-Static Drift Over One Minute

In an effort to better understand signal drift over a longer term than 10 seconds, signal drift was evaluated over a one minute interval for FeGa Patch 1 Edge (a), as seen in Figure D.1.

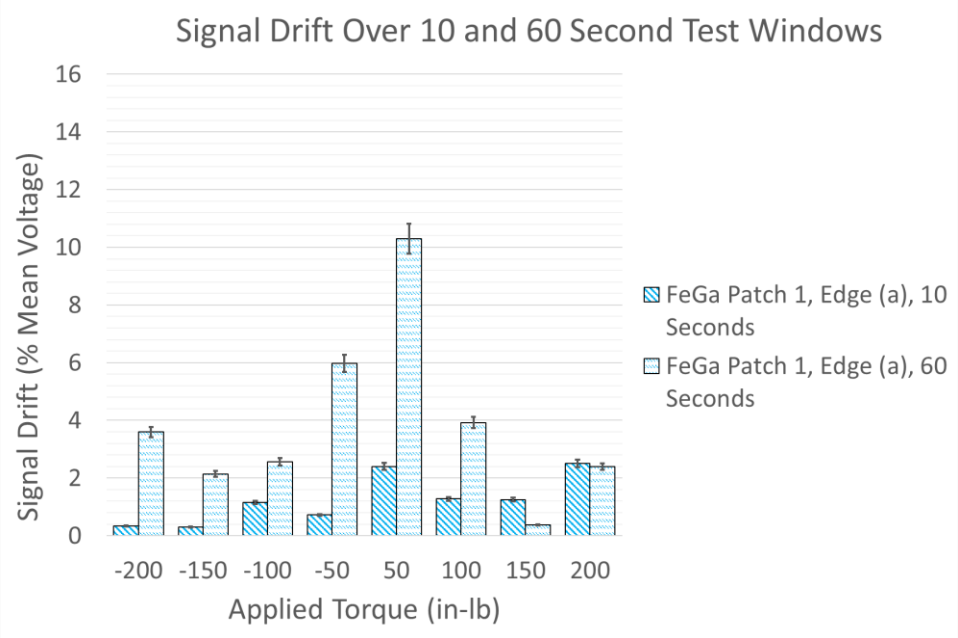

Figure D.1: Magnitude of sensor drift (% mean voltage) generally tended to be greater when observed over longer periods of time.

For each torque application, with the exception of +150 and +200 in-lb, the drift over one minute is greatest. Low torque cases exhibited high drift as percent of mean output voltage. Hall effect sensor output voltage was 13mV in the -50 in-lb case and 11mV in the +50 in-lb case. This means the corresponding drifts for each case were only about 0.8 mV and 1.1 mV respectively. This makes sense because as with other cases, drift as percent mean generally tended to decrease as applied load increased.

Works Cited

[1] S. R. Day, "The design, construction and testing of a scour monitoring system using magnetostrictive materials," 2014.

[2] I. Chopra and J. Sirohi, "Smart Structures Theory," in *Smart Structures Theory*, New York, NY: Cambridge University Press, 2014, pp. 581–678.

[3] S. M. Na, M. Rice, G. Raghunath, V. Klimchenko, and A. B. Flatau, "Magnetostrictive Alfenol Whisker Sensor Performance and Sensitivity to Whisker Thickness," *IEEE Trans. Magn.*, vol. 50, no. 11, pp. 1–4, Nov. 2014.

[4] J. Atulasimha, "Characterization and modeling of the magnetomechanical behavior of iron-gallium alloys," 2006.

[5] J. Atulasimha and A. B. Flatau, "A review of magnetostrictive iron–gallium alloys," *Smart Mater. Struct.*, vol. 20, no. 4, p. 43001, Apr. 2011.

[6] E. N. Economou, *The Physics of Solids*. Berlin, Heidelberg: Springer Berlin Heidelberg, 2010.

[7] L. Sandlund, M. Fahlander, T. Cedell, A. E. Clark, J. B. Restorff, and M. Wun-Fogle, "Magnetostriction, elastic moduli, and coupling factors of composite Terfenol-D," *J. Appl. Phys.*, vol. 75, no. 10, p. 5656, May 1994.

[8] A. E. Clark, J. B. Restorff, M. Wun-Fogle, and E. Summers, "Effect of stress annealing on Galfenol and Alfenol magnetostrictive alloys," 2006, vol. 6170, p. 61700I–61700I–2.

[9] W. J. Fleming, "New Automotive Sensors #x2014;A Review," *IEEE Sens. J.*, vol. 8, no. 11, pp. 1900–1921, Nov. 2008.

[10] W. J. Fleming, "Overview of automotive sensors," *IEEE Sens. J.*, vol. 1, no. 4, pp. 296–308, Dec. 2001.

[11] H. Ng, L. T. Rupert, and M. J. Devsam, "Torque and position sensor," US5837908 A, 17-Nov-1998.

[12] S. J. Horton, A. L. Trace, and D. Rees, "Optical displacement sensor and torque sensor employing relatively movable slit patterns," US5841132 A, 24-Nov-1998.

[13] M. Taniguchi, H. Nagano, T. Daido, I. Kuramoto, M. Nohara, and H. Kyotani, "Torque sensor," US4907460 A, 13-Mar-1990.

[14] K. Chikaraishi and K. Satoh, "Torque sensor," US5796014 A, 18-Aug-1998.

[15] "Development of a Contactless Hall Effect Torque Sensor for Electric Power Steering." [Online]. Available: http://papers.sae.org/2006-01-0939/. [Accessed: 04-Jan-2017].

[16] P. Gandel, D. Frachon, D. Angleviel, C. Oudet, and D. Prudham, "Position sensor, designed in particular for detecting a steering column torsion," US7028545 B2, 18-Apr-2006.

[17] V. A. Kalinin and M. Lee, "Temperatures stable saw sensor with third-order elastic constants," US7202589 B2, 10-Apr-2007.

[18] I. J. Garshelis, "Collarless circularly magnetized torque transducer and method for measuring torque using same," US6145387 A, 14-Nov-2000.

[19] I. J. Garshelis, D. Hooper, and R. J. Kari, "Bands of circumferential remanent magnetization obtained by sequential application of axial fields and torsion," *IEEE Trans. Magn.*, vol. 40, no. 4, pp. 2658–2660, Jul. 2004.

[20] I. J. Garshelis and S. P. L. Tollens, "Influence of geometric factors on the polarity of a remanent magnetization," *IEEE Trans. Magn.*, vol. 41, no. 10, pp. 2796–2798, Oct. 2005.

[21] I. J. Garshelis, R. J. Kari, and S. P. L. Tollens, "A Rate of Change of Torque Sensor," *IEEE Trans. Magn.*, vol. 43, no. 6, pp. 2388–2390, Jun. 2007.

[22] "Core Torque Sensor," *MagCanica Inc :: Home*, 2011. [Online]. Available: http://www.magcanica.com/torque.html. [Accessed: 05-Jan-2017].

[23] M. B. Moffett, A. E. Clark, M. Wun-Fogle, J. Linberg, J. P. Teter, and E. A. McLaughlin, "Characterization of Terfenol-D for magnetostrictive transducers," *J. Acoust. Soc. Am.*, vol. 89, no. 3, pp. 1448–1455, Mar. 1991.
[24] Y.-W. Park and M.-C. Yim, "Design and characterization of a magnetostrictive microactuator," *Phys. Status Solidi A*, vol. 201, no. 8, pp. 1983–1987, Jun. 2004.
[25] J. R. Cullen, A. E. Clark, M. Wun-Fogle, J. B. Restorff, and T. A. Lograsso, "Magnetoelasticity of fe–ga and fe–al alloys," *J. Magn. Magn. Mater.*, vol. 226, pp. 948–949, 2001.
[26] R. A. Kellogg, "Development and modeling of iron-gallium alloys," Iowa State University, 2003.
[27] S. M. Na and A. B. Flatau, "Global Goss grain growth and grain boundary characteristics in magnetostrictive Galfenol sheets," *Smart Mater. Struct.*, vol. 22, no. 12, p. 125026, Dec. 2013.
[28] T. V. Jayaraman, N. Srisukhumbowornchai, S. Guruswamy, and M. L. Free, "Corrosion studies of single crystals of iron–gallium alloys in aqueous environments," *Corros. Sci.*, vol. 49, no. 10, pp. 4015–4027, Oct. 2007.
[29] M. Michael, "Development of a Bio-Inspired Magnetostrictive Flow and Tactile Sensor," Master's Thesis, University of Maryland, 2012.
[30] G. Raghunath, "Wireless Magneto-Elastic Torque Sensor System," University of Maryland College Park, Scolarly Paper, 2012.
[31] J.-H. Yoo and A. B. Flatau, "A bending-mode galfenol electric power harvester," *J. Intell. Mater. Syst. Struct.*, vol. 23, no. 6, pp. 647–654, Apr. 2012.
[32] M. Germer, "Optimization Studies of a Magnetostrictive Energy Harvester," University of Dresden, 2016.
[33] A. E. Clark, J. B. Restorff, M. Wun-Fogle, T. A. Lograsso, and D. L. Schlagel, "Magnetostrictive properties of body-centered cubic Fe-Ga and Fe-Ga-Al alloys," *IEEE Trans. Magn.*, vol. 36, no. 5, pp. 3238–3240, Sep. 2000.
[34] A. S. Purekar, J.-H. Yoo, and A. B. Flatau, "Apparatus and method for non contact sensing of forces and motion on rotating shaft," US20130291657 A1, 07-Nov-2013.
[35] G. Raghunath, A. B. Flatau, A. Purekar, and J.-H. Yoo, "Non-Contact Torque Measurement Using Magnetostrictive Galfenol," in *Proceedings of the ASME 2013 Conference on Smart Materials, Adaptive Structures, and Intelligent Systems*, Snowbird, Utah, USA, 2013, p. 12.
[36] C. Felippa, "Introduction to Aerospace Structures (ASEN): Chapter 7, Torsion of Circular Shafts." University of Colorado at Boulder, 12-Sep-2016.
[37] "Mohr's circle - Wikiversity." [Online]. Available: https://en.wikiversity.org/wiki/Mohr%27s_circle. [Accessed: 13-Apr-2017].
[38] A. Sutor, S. Bi, and R. Lerch, "Identification and verification of a Preisach-based vector model for ferromagnetic materials," *Appl. Phys. A*, vol. 118, no. 3, pp. 939–944, Mar. 2015.
[39] W. D. Armstrong, "An incremental theory of magneto-elastic hysteresis in pseudo-cubic ferro-magnetostrictive alloys," *J. Magn. Magn. Mater.*, vol. 263, no. 1–2, pp. 208–218, Jul. 2003.
[40] J. Atulasimha, A. B. Flatau, and E. Summers, "Characterization and energy-based model of the magnetomechanical behavior of polycrystalline iron–gallium alloys," *Smart Mater. Struct.*, vol. 16, no. 4, pp. 1265–1276, Aug. 2007.
[41] Liang Shu, M. J. Dapino, P. G. Evans, Dingfang Chen, and Quanguo Lu, "Optimization and Dynamic Modeling of Galfenol Unimorphs," *J. Intell. Mater. Syst. Struct.*, vol. 22, no. 8, pp. 781–793, May 2011.
[42] P. G. Evans and M. J. Dapino, "State-Space Constitutive Model for Magnetization and Magnetostriction of Galfenol Alloys," *IEEE Trans. Magn.*, vol. 44, no. 7, pp. 1711–1720, Jul. 2008.

[43] E. Summers, “Galfenol - A New Class of Magnetostrictive Materials,” presented at the Galfenol Public Release V.7, Ames, IA, 2012.
[44] “ASM Material Data Sheet: Aluminum 2024-T4; 2024-T351.” [Online]. Available: http://asm.matweb.com/search/SpecificMaterial.asp?bassnum=ma2024t4. [Accessed: 04-Apr-2017].
[45] F. Metz, “PS-2016-102 Acknowledgment Letter,” 19-Jul-2016.
[46] “Loctite 648 Technical Data Sheet,” *Loctite: Henkel Adhesives North America*, Oct-2005. [Online]. Available: http://www.loctite.sg/sea/content_data/93769_Loctite_648_Retaining_Compound.pdf. [Accessed: 03-Jan-2017].
[47] J. S. Tomblin, W. P. Seneviratne, H. Kim, and J. Lee, “Box Beam Lap Shear Torsion Testing for Evaluating Structural Performance of Adhesive Bonded Joints,” in *Joining and Repair of Composite Structures*, ASTM International, 2004.
[48] “Magnetic Particle Brake B220 Data Sheet.” Placid Industries, Inc.
[49] T. Baker, “Torque Sensor Requirement,” 13-Dec-2016.
[50] M. Bhagwat, “UMD 2011-16 VLRCOE Final Review Feedback Task A-1.15,” 13-Jan-2017.